USING QUASAR COMPOSITE SPECTRA TO CONSTRAIN MODELS OF QUASAR SPECTRAL DIVERSITY

by

David Harris

A dissertation submitted to the faculty of
The University of Utah
in partial fulfillment of the requirements for the degree of

Doctor of Philosophy

in

Physics

Department of Physics and Astronomy

The University of Utah

August 2016

The University of Utah Graduate School

STATEMENT OF DISSERTATION APPROVAL

The dissertation of **David Harris**

has been approved by the following supervisory committee members:

Kyle Dawson	, Chair	**20 July 2015** Date Approved
Inese I. Ivans	, Member	**20 July 2015** Date Approved
Paolo Gondolo	, Member	Date Approved
Christoph Boehme	, Member	**20 July 2015** Date Approved
Julio Cesar Facelli	, Member	**20 July 2015** Date Approved

and by **Carelton DeTar** , Chair/Dean of

the Department/College/School of **Physics and Astronomy**

and by David B. Kieda, Dean of The Graduate School.

ABSTRACT

The Baryon Oscillation Spectroscopic Survey (BOSS) collected more than 150,000 quasar spectra. I first create a composite spectrum of 102,150 quasar spectra from 800 Å to 3300 Å at a signal-to-noise ratio close to 1000 per pixel (Δv of 69 km s^{-1}) as a tool to study the demographics of this large sample. Essential to an accurate construction of this composite spectrum is a correction to account for flux calibration residuals in the BOSS spectrophotometry. I confirm that the resulting flux-calibrated spectrum is consistent with SDSS photometry, thus validating that broad-band and emission features are preserved to better than 5% in the coaddition process. I then use this unprecedented sample to investigate quasar spectral diversity through multiple composite spectra binned by quasar property. I determine the relative influence of quasar luminosity, black hole mass, accretion efficiency, and quasar spectral index on quasar emission line diversity. A comparison of models that predict the dependence of high-ionization emission features on the intrinsic quasar luminosity demonstrates that one particular model is favored.

CONTENTS

ABSTRACT iii

LIST OF TABLES vi

Chapters

1. INTRODUCTION 1

1.1 Quasars 2
1.2 Quasar Structure 4
1.3 Quasar Composite Spectra 5
1.4 Equivalent Width 6
1.5 Baldwin Effect 6
1.6 Structure of the Dissertation 7

2. QUASAR PHYSICS 11

2.1 Spectral Index 11
2.1.1 α_λ vs α_ν 11
2.2 Eddington Limit 12
2.3 Understanding Baldwin Effect Models 14
2.4 Models of the Baldwin Effect 14
2.4.1 Wandel 99a Model 15
2.4.2 Wandel 99b Model 16
2.4.3 Korista Model 17
2.4.4 Modified Baldwin Effect 17

3. DATA 18

3.1 Source of the Data 18
3.1.1 The SDSS Program 18
3.1.2 The BOSS Program 19
3.1.3 Sample Selection 21
3.1.4 Properties of the Final Sample 21
3.2 Flux Calibration 22
3.2.1 Spectrophotometric Errors 22
3.2.2 Correcting the Spectrophotometric Errors 24
3.3 BOSS/SDSS Ratio 27

4. QUASAR COMPOSITE SPECTRUM 41

4.1 Previous Quasar Composite Spectra 41
4.1.1 Constructing the Composite 43
4.2 Spectral Index 45
4.2.1 Composite and Sample Spectral Index. 46
4.2.2 Quasar Sample Median Spectral Index Binned by Redshift 46
4.2.3 Comparing Spectral Index to Quasar Color 48
4.3 Spectral Features 49
4.3.1 Line Fitting 49
4.4 Discussion of the Composite 50

5. DATA CATALOGS AND COMPOSITE SPECTRA ANALYSIS 62

5.1 Data 62
5.2 Calculated Quantities 63
5.2.1 Black Hole Mass 63
5.2.2 Full Width Half Maximum 63
5.2.3 Bolometric Luminosity 64
5.2.4 Eddington Luminosity and Eddington Ratio 64
5.3 Comparing the Data Catalogs 64
5.3.1 Redshift 65
5.3.2 Bolometric Luminosity 65
5.3.3 Full Width Half Maximum 66
5.3.4 Black Hole Mass 68
5.3.5 Eddington Ratio 68
5.4 Comparing Quantities 69
5.5 Composite Spectra Analysis 69
5.5.1 Composite Spectra and Errors 69
5.5.2 Measuring Equivalent Width 71
5.6 Preservation of Spectral Properties in Composite Spectra 72

6. THE REDSHIFT DEPENDENCE OF QUASAR SPECTRAL PROPERTIES . . 90

6.1 Baldwin Effect in i-Band Magnitude and Redshift 92

7. LINEWIDTH RELATIONSHIPS TO QUASAR OBSERVABLES 104

7.1 Analysis 105
7.1.1 Tests to Baldwin Effect Models at all Luminosities 105
7.2 Bolometric Luminosity, Linear Fit 106
7.3 Comparing Modified Baldwin Effect Parameterizations 106

8. DISCUSSION AND CONCLUSION 130

REFERENCES 132

LIST OF TABLES

1.1 Common emission lines, their wavelengths, and the ionization energy required to create each species of ion. 10

3.1 Conversion from SDSS to AB magnitudes, in the form $\delta m = m_{AB} - m_{SDSS}$. . . 29

3.2 This table shows the number of quasars remaining in the sample after each sample selection criterion is applied. 29

3.3 Data showing the fitted slope, intercept, and color bias at the average airmass of 1.095 for (SDSS PSF magnitudes - BOSS synthetic magnitudes) in the g, r, and i filters. The second column is the characteristic error in magnitude for each filter. The first set of columns is for the uncorrected raw data, the second set of columns shows the values after performing the first round of corrections, and the third set of columns shows the values after the final round of corrections. 34

3.4 Plates used in making the spectrophotometric correction to the data using the blue reduction. 35

4.1 The respective ranges of redshifts and K-corrected i-band absolute magnitudes in recent composites, including this work. Also included is the equivalent width of the C IV emission line in each composite. 52

4.2 Emission lines detected in the composite spectrum generated in this work compared to known wavelengths and the measurements from V01. Entries that required multiple fits to describe the emission feature are listed with an additional suffix (e.g. Lyα-1 and Lyα-2). Blends are presented with each discrete component in the lab frame and by the multiple components in the observed data (e.g. Si IV / O IV). 61

6.1 This table shows the lines of interest examined for this study. The "blue continuum" region and "red continuum region" are used for fitting the continuum, while the "line region" indicates the wavelength range over which the equivalent width of the line will be found. The ranges for Mg II and C IV are taken directly from the Shen catalog. 96

6.2 The quasar composite spectra used in the initial tests to determine the redshift dependence on the Baldwin Effect. 99

7.1 The quality of the fits using the Korista model are shown. Comparisons to the predictions when using high-luminosity quasars are also indicated, as is the quality of the fit. 109

7.2 The quality of the fits using the Wandel99a (W99a) model are shown. Comparisons to the predictions when using high-luminosity quasars are also indicated, as is the quality of the fit. 109

7.3 The quality of the fits using the Wandel99b (W99b) model are shown. Comparisons to the predictions when using high-luminosity quasars are also indicated, as is the quality of the fit. 110

7.4 Slope of Baldwin Effect divided by 68% confidence interval for that parameter, in each line used. 110

CHAPTER 1

INTRODUCTION

Since their initial discovery (Sandage 1961; Greenstein 1963; Hazard et al. 1963; Oke 1963; Schmidt 1963; Burbidge 1967), quasars have played a critical part in probing and understanding the universe at high redshifts. A quasar is an extremely luminous extragalactic object. The luminous energy of a quasar is released by the accretion of hot gas on to a supermassive black hole at the core of a galaxy. A quasar is generally more luminous than all the stars in the galaxy in which the quasar resides. More recent observations have confirmed the existence of supermassive black holes (SMBHs) at the center of galaxies (Kormendy & Richstone 1995; Ghez et al. 1998; Ferrarese & Merritt 2000; Gebhardt et al. 2000), including our own; studies of the connection between quasar activity and the formation of galaxies continue today.

Quasars are characterized through their high luminosity, their broad spectral features, their power law continuum, their relative compactness, and their variability. Quasars can be observed in a wide range of redshifts, from close to zero to five or more. A redshift of five equates to a light travel time of 12.5 billion years, implying the light was emitted approximately 1 billion years after the Big Bang under the assumption of a flat Universe with matter responsible for 30% of the total energy density (Wright 2006). The nearest known quasar, IC 2497 (Schawinski et al. 2010b), technically a "dead" or nonemitting quasar, is at a redshift of 0.052, or a distance of 730 million light years, or 220 megaparsecs. A dead quasar is one in which the central black hole has no detectable accretion. These systems are still detectable and identifiable due to their lingering effects upon nearby gas (photoionization), which is possible due to light speed delay. This particular quasar is the progenitor of Hannys Voorwerp (Schawinski et al. 2010a).

In this work, I show that quasar composite spectra can be used to constrain models of quasar spectral diversity. This application of quasar composite spectroscopy to constraining models for quasar diversity offers a new way of examining the well-known Baldwin Effect, which describes the observed correlation between luminosity and emission line strength (Baldwin 1977). In addition, the sample is extremely large (the largest sample of quasars

made for a set of composite spectra). Data are taken from the Baryon Oscillation Spectroscopic Survey (BOSS; Dawson et al. 2013), part of the Sloan Digital Sky Survey (SDSS; Eisenstein et al. 2011).

1.1 Quasars

A quasar is a rapidly accreting supermassive black hole at the center of a galaxy. Quasars are among the most luminous single objects in the known universe. Quasars exist across a range of luminosities; quasars observed in large scale surveys commonly fall between $10^{46-47.5}$ erg s^{-1}. As gas falls onto the central black hole, it forms an accretion disk surrounding the central black hole due to the effects of angular momentum conservation. Viscosity and differential rotation in the disk cause the material to heat up and radiate, losing energy. The disk itself can reach temperatures in the order of 100,000 K. While quasar spectra show important similarities, fundamental differences remain. Shen & Ho (2014) recently found that one important difference between quasar spectra, the FWHM of the $H\beta$ emission line, can be explained by the orientation of the quasar relative to the observer's line of sight.

The material associated with quasar emission lines is ionized by the ultraviolet (UV) continuum, generally in the tens of eV, emitted by an accretion disk surrounding a black hole. Although this region of UV emission is rarely observable, the relative flux between different emission lines can provide insights into the far-UV continuum and offer constraints on the temperature profile of the hottest regions of the accretion disk. Wills et al. (1985) and Francis et al. (1991) both found the ratio between Lyman-α flux and FeII flux to be much greater than expected given standard photoionization models. Wilhite et al. (2005) and Ruan et al. (2014) reported an average quasar spectral index (α_λ) of -1.35 and -1.38, respectively, in the optical to Far UV (1300 Å to 5800 Å and 1400 Å to 7000 Å, respectively), which may be an important parameter in quasar photoionization models if the quasar spectral index at shorter wavelengths is related to the spectral index at these wavelengths. Pereyra et al. (2006) and Sakata et al. (2011) argue that the quasar accretion disk can be modeled by a simple thin disk because the spectral index varies between repeat spectral observations of quasars. Nagao et al. (2006) also constrained quasar models through observations of the broadline region in quasar spectra, constraining the gas metallicity and metallicity evolution of the broadline region.

The active, light-emitting region of a quasar is always resolved as a point source in telescopes. This indicates the maximum size of a quasar is less than a kiloparsec (Tremaine

2014). For example, at redshift of 0.5 one kiloparsec subtends 0.161 arcseconds of sky (Wright 2006), roughly the resolution of the Hubble Space Telescope. Lower limits to quasar size can be made through an examination of the light travel time across the light-emitting region. Quasars are highly variable objects, varying in brightness as matter is consumed by the black hole and the emitted light travels across the quasar itself. The timescale of variability is related to the light travel time across the quasar. This variability can range from days to decades. Using the most highly variable quasars and the argument that the various parts of the quasar must be causally connected, we can infer the smallest quasars can be no smaller than a few light-days across, which is less than one percent of a parsec or a few hundred times the earth-sun distance (1 Astronomical Unit or AU). Due to this small (astrophysical) size, the innermost regions of a quasar cannot be resolved by even large modern telescopes. As such, a great deal of uncertainty remains in our understanding of quasar astrophysics. Instead of resolving the details of a quasar, many studies have focused on using quasar spectra to improve our understanding of quasars.

The mass of the black hole of a quasar is strongly correlated to the mass of the parent galaxy. Often, the mass of the central black hole is approximately 0.2% of the mass of the parent galaxy. That equates to black hole masses in the range 10^{8-10} times the mass of the sun ($M_\odot$ or M_{sun} depending on nomenclature). Quasar luminosity is generally measured as a bolometric luminosity or as a K-corrected i-band absolute magnitude. The bolometric luminosity is a measure of all the energy released by the quasar as photons, and is measured in watts, ergs per second, or solar luminosities. The i-band absolute magnitude is a measure of the flux in the SDSS i-band filter, from approximately 7000 Å to 8500 Å in the observer frame. However, a different part of the rest spectrum is measured as part of the i-band for quasars at different redshifts. Thus, in this work, all i-band absolute magnitudes are quoted as K-corrected i-band absolute magnitudes. This K-correction measures the i-band absolute magnitude of the quasar as if the quasar was actually at a redshift of 2. Thus, the i-band absolute magnitudes used in this work always measure the magnitude of the same part of the quasar spectrum, and take into account cosmological effects to the apparent brightness.

Photons escaping the central regions of a quasar can eventually enter intergalactic space. Intergalactic space is generally considered to have a low optical depth. In other words, an optical or UV photon can be expected to travel unabsorbed for billions of years, so that we have a relatively unobscured view of the quasar. Two typical quasar spectra, taken from BOSS, are shown in Figure 1.1. The first spectrum is of a quasar at a redshift of

2.3 and the second is at 3.3. Despite the cosmological distance between them, remarkable similarities remain. Both display a power law continuum, with flux increasing at decreasing wavelength. Both have the same emission lines, with similar emission line strength.

There are exceptions to this general rule. In particular, there are regions of a quasar spectrum wherein this is less likely to be true. Here, we discuss the Lyman Alpha Forest. For the sake of example, assume a 1000 Å photon is emitted from a quasar at a redshift of 2. This photon may travel through clouds of intergalactic hydrogen very efficiently. However, as it travels, the expansion of the universe increases the wavelength of the photon (redshift). At some point, the wavelength of this photon will be extended to 1216 Å, the wavelength of the Lyman-α transition. If this photon intersects a cloud of intergalactic neutral hydrogen while it has this wavelength, it is likely to be absorbed by said cloud. In a quasar spectrum, this creates a trough at that wavelength. That trough is preserved and can be detected in quasar spectra. This allows a method to probe clouds of intergalactic hydrogen. This is called the Lyman Alpha Forest. The second quasar shows more absorption features blueward of Lyman-α than the first due to the effects of the Lyman-α Forest.

1.2 Quasar Structure

A quasar is a hot disk of gas surrounding a supermassive black hole at the center of a galaxy. The disk emits photons from the infrared to the soft X-ray, while a corona of superheated gas emits up to hard X-ray photons. There also exist clouds of ionized gas which are partly responsible for emission lines. See Figure 1 from Urry & Padovani (1995) for a visual representation of this.

The temperature of the accretion disk is not constant with distance from the central black hole. As such, the spectrum of the disk is really a superposition of many black body spectra at temperatures decreasing with increasing distance from the central engine. By observing the summation over each black body spectrum, the observer witnesses a broad spectrum best described by a power law.

Broad emission lines originate from relatively dense (10^9 particles per cubic centimeter) regions close to the central black hole and close to the central ionizing regions. The FWHM of these lines can be as high as tens of thousands of kilometers per second. Table 1.1 shows a number of emission lines, their wavelenghts, and the ionization energy required to create each species of ion.

Black holes cannot consume mass at an infinite rate, and are limited in a way similar to the limitation on stellar size. The "Eddington Limit" is the accretion rate (and hence the

luminosity) of a quasar in which the forces on gas outside the event horizon are balanced, with the force of the black hole's gravity pulling inward and the radiative pressure of the photons pushing outward. The greater the mass of a black hole, the more luminous it can be before the accretion exceeds the Eddington limit. Not all quasars must accrete at the maximum rate. The Eddington Ratio is the ratio between the actual accretion rate (determined through the luminosity of the quasar) and the maximum accretion rate for a black hole of that mass. The Eddington luminosity, Eddington limit, and Eddington ratio are discussed in detail in Section 2.2.

A technique known as Reverberation Mapping can tell us about the mass of the central black hole using time delay and the variability scale time. The masses of a number of black holes have been determined through reverberation mapping, and from those studies, scaling relationships between more easily observable quasar properties (such as quasar continuum luminosity and FWHM of various lines) and black hole masses have been identified. Thus, estimates of black hole mass can be made without time consuming reverberation mapping studies. A single spectrum is all that is necessary to estimate quasar black hole mass (Shen et al. 2011), though the uncertainty on such a measurement is large.

1.3 Quasar Composite Spectra

Weaker emission lines, including iron lines, are detectable in high signal-to-noise ratio composite quasar spectra (Francis et al. 1991). Composite spectra can provide redshift estimators for individual quasar spectra when used as a cross-correlation template (Vanden Berk et al. 2000). They allow for better quasar selection from photometric data by predicting color as a function of redshift (Richards et al. 2002). They can facilitate better continuum normalization for quasar absorption line studies, for example in studies of the Lyman-α forest and Broad Absorption Line (BAL) quasars (Grier et al. 2015).

Quasar composite spectra also provide insight into quasar astrophysics. Francis et al. (1991) showed that quasar spectra are governed by a power law continuum by generating a composite of 718 quasars from the Large Bright Quasar Survey (Foltz et al. 1989), covering a wavelength range of approximately 800 Å to 5800 Å in the restframe. Vanden Berk et al. (2001) (hereafter V01) used 2204 spectra to generate a composite spectrum, taking data from the commissioning phase of the Sloan Digital Sky Survey 1 (SDSS) (York et al. 2000). Their composite covered a wavelength range of 800 Å to 8555 Å in the restframe and included quasars in the redshift range $0.044 \leq z \leq 4.789$. V01 showed systematic velocity shifts from tens to a few hundred km s^{-1} between quasar emission lines. The optical depth

blueward of Lyman-α increases with redshift, thus requiring a low-redshift survey from a space-based telescope to create a quasar spectrum blueward of Lyman-α. Shull et al. (2012) created a composite spectrum from 22 AGN using HST-COS data, with a wavelength range of 550 Å to 1750 Å in the restframe over $0.026 \leq z \leq 1.44$. This high signal-to-noise ratio composite spectrum shows that the power law continuum continues below the Lyman Limit wavelength (912 Å) without a significant break. Stevans et al. (2014) (hereafter S14) included 159 quasars and expanded the work of Shull et al. (2012) by covering a slightly greater redshift range.

1.4 Equivalent Width

Equivalent width is calculated by normalizing the integrated flux under the emission line by the average flux of the continuum below the line. Equivalent width is therefore represented in units of wavelength, typically angstroms. Thus, a line will have a smaller equivalent width if the integrated line flux is held constant but the continuum flux is increased. Quasars can be characterized by having emission lines superimposed on a power law continuum. Thus, to find the equivalent width of a quasar emission line, one must fit and subtract the power law continuum, find the integrated line flux, and divide by the mean continuum luminosity at the line position.

1.5 Baldwin Effect

There exists an inverse relationship between the luminosity of a quasar and the equivalent width of major emission lines in that quasar. This relationship was first noted by Baldwin (Baldwin 1977) and is known as the Baldwin Effect. The effect was discovered just 15 years after the original discovery of quasars. The discovery was made using spectroscopic data on just 20 quasars from the Lick Observatory. Using these data, Baldwin was able to show a negative correlation between the continuum luminosity of a quasar (L_λ) and the equivalent width of the C IV emission line. If this trend can be analyzed and examined in great detail, a measurement of the equivalent width of a line can be used to calculate the luminosity of a quasar. This effect was first called the "Baldwin Effect" by Carswell & Smith (1978). Numerous physical reasons for the Baldwin Effect have been proposed, including quasar inclination angle (Netzer et al. 1992; Wilkes et al. 1999), covering factor (Wu et al. 1983), the existence of optically thin clouds (Shields et al. 1995), or changes in spectral energy distribution with luminosity (Wandel 1999a).

Later studies confirmed the existence of the Baldwin effect in a variety of lines and

conditions. Kinney et al. (1990) and Zamorani et al. (1992) expanded the original work of Baldwin to wider ranges of quasar luminosity and redshift. UV iron emission lines were shown to exhibit the Baldwin Effect by Green et al. (2001). The Baldwin Effect was observed in forbidden lines by Croom et al. (2002). Dietrich et al. (2002) measured the Baldwin Effect in 22 different lines.

A correct understanding of the nature of the Baldwin Effect can lead to what has long been considered the "Holy Grail" of quasar astrophysics: the use of quasars as standard candles. If quasars can be used as standard candles, they can be used for cosmological studies of the expansion of the universe (Baldwin 1977). Currently, the best studies of the effect of dark energy on cosmological expansion use approximately 500 supernovae (Betoule et al. 2014). The BOSS program currently has over 100,000 quasar spectra across a range of cosmologically interesting redshifts, which could be used to constrain models of dark energy and cosmological expansion.

Additionally, a Baldwin Effect for Fe Kα in the X-ray was discovered by Iwasawa & Taniguchi (1993). Here, the X-ray luminosity (at 2 keV) of a quasar is anticorrelated with the Equivalent width of the narrow Fe Kα line at 6.4 keV. This discovery was made using data from the X-ray observatory Ginga and later confirmed by data from ASCA (Tanaka et al. 1994) and Chandra and XMM-Newton (Page & et al. 2004; Zhou & Wang 2005; Jiang et al. 2006; Bianchi et al. 2007). The location of origin of Fe Kα within the quasar accretion disk is not known. The Broad Emission Line Region, the outer edge of the accretion disk, and the molecular torus surrounding the accretion disk have all been proposed as possible origins of the Fe Kα line (e.g., Weaver et al. 1992; Antonucci 1993; Krolik et al. 1994).

Despite this large quantity of studies and observations of the Baldwin Effect, there are no models which provide a complete explanation of the origin of the Baldwin Effect. Many models have been proposed to explain the Baldwin Effect (Wu et al. 2009; Zhang et al. 2013; Ricci et al. 2013, 2014).

1.6 Structure of the Dissertation

In Chapter 2, I discuss what is known about quasar physics, as well as some of the outstanding questions remaining. In particular, I discuss important properties of quasars, such as the spectral index and black hole mass, as well as how to determine these quantities through observations. I discuss reverberation mapping in detail, and present the method to determine the Eddington limit given a black hole mass. I also present the models which attempt to explain and predict the Baldwin Effect. In Chapter 3, I present the data

used in this dissertation. In Chapter 4, I explain the method used in creating a quasar composite spectrum, as well as the need for, the creation of, and the implementation of a spectrophotometric correction. This result is found in a paper recently accepted for publication by the Astronomical Journal (Harris et al. 2016). I also show that quasar composite spectra preserve the average spectral properties of quasar samples. In Chapter 5, I begin an exploration of quasar diversity. I first define the sample of quasars used and compare quasar catalogs used to find quasar properties. I also explain the methods used to derive quasar properties (such as black hole mass and bolometric luminosity) used in this work and how to create binned composites, find their errors, and find the equivalent width and its error. In Chapter 6, I present quasar composite spectra binned by redshift. I examine the differences between these quasar composite spectra and explain the origin of these differences. In Chapter 7, I measure the Baldwin Effect given various parameters. Here, I use this information to test the models which have been proposed to explain the Baldwin Effect. In Chapter 8, I conclude.

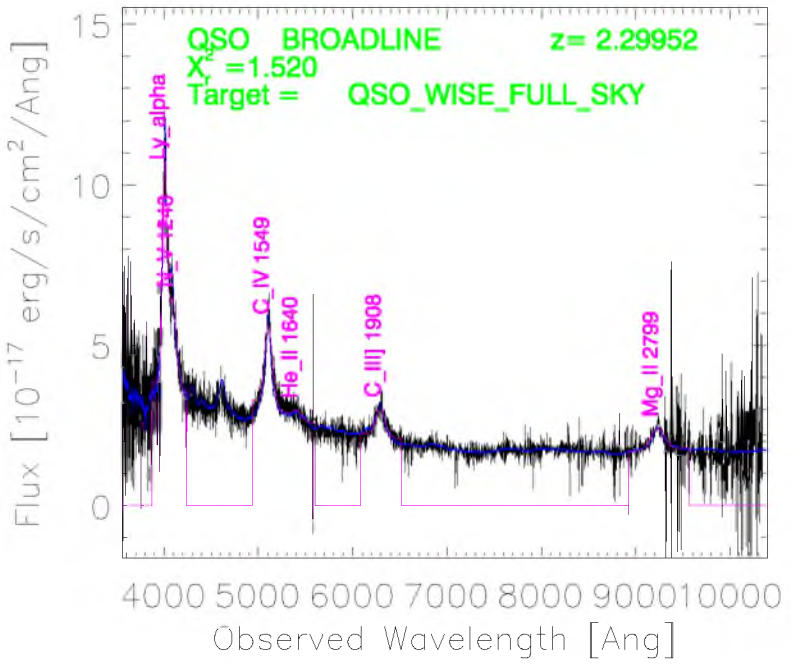

Figure 1.1: Example of a quasar spectrum. Spectrum of quasar observed on plate 6114, fiber 198, on MJD 52609. Quasar flux is shown in black, the smoothed flux is shown in blue, and lines and line identification are shown in purple.

Table 1.1: Common emission lines, their wavelengths, and the ionization energy required to create each species of ion.

Line	Wavelength (Å)	Ionization Energy (eV)
O IV	1034	113.9
N V	1240	77.7
He II	1640	54.4
He II	4686	54.4
C IV	1549	47.9
N IV]	1486	47.4
O III]	1663	35.1
O III]	5007	35.1
Si IV	1402	33.5
N III]	1750	29.6
Al III	1857	28.4
C III]	1909	24.4
Si III]	1892	16.3
Lyα	1216	13.6
Hγ	4340	13.6
Hβ	4861	13.6
C II	1335	11.3
Si II	1260	8.2
Fe II	UV Complex	7.9
Fe II	Optical Complex	7.9
Mg II	2798	7.6
O I	1305	0.0

CHAPTER 2

QUASAR PHYSICS

This chapter presents the relevant mathematical and physical background for quasar accretion and emission. I discuss the observed continuum of broadband emission and how we measure and report the shape of the continuum. I discuss the accretion rate and the related quantity, the Eddington limit. I discuss the primary method for determining the mass of a black hole in a quasar, known as reverberation mapping. Finally, I discuss models proposed to explain the Baldwin Effect.

2.1 Spectral Index

Quasar spectra generally exhibit a power law continuum. The spectral index describing this power law does not need to remain constant throughout the entirety of the spectrum. The spectral index can be presented in terms of α_λ or α_ν, being parameterized on the wavelength or the frequency, respectively. In general, optical and UV spectral indices are presented as α_λ and radio spectral indices are presented as α_ν, although there are numerous exceptions to this general rule. This is because optical spectra are generally recorded in units of f_λ ($ergs^{-1}cm^{-2}Ang^{-1}$) and radio spectra are recorded in units of f_ν ($ergs^{-1}cm^{-2}Hz^{-1}$).

Ionizing photons generally lie at shorter wavelengths than we use in this paper, but the spectral index of a quasar can allow us to estimate the flux of the ionizing continuum even at wavelengths unobservable on the surface of the earth and/or for low-redshift quasars. This is because the spectrum can be extrapolated to short, ionizing wavelengths through observations of optical and UV spectral index. The extrapolation is not perfect, but it gives a good order-of-magnitude estimate.

2.1.1 α_ν versus α_λ

The spectral index of a quasar spectrum can be expressed in terms of α_ν or α_λ. Here, we use α_λ, but it is instructive to show how the two are related.

If we assume a quasar flux distribution approximating a power law, we can assume

$$F(\lambda) = K_\lambda \lambda^{\alpha_\lambda} \tag{2.1}$$

where $F(\lambda)$ is the flux at wavelength λ, K_λ is a constant, and α_λ is the spectral index, a negative value. The energy in a wavelength interval can be expressed as

$$E(\lambda, \lambda + d\lambda) = K_\lambda \lambda^{\alpha_\lambda} d\lambda \tag{2.2}$$

since

$$\lambda = \frac{c}{\nu} \tag{2.3}$$

where c is the speed of light and ν is the frequency, this implies

$$\frac{d\lambda}{d\nu} = c\frac{-1}{\nu^2} \tag{2.4}$$

or

$$d\lambda = -c\frac{1}{\nu^2} d\nu \tag{2.5}$$

Using Equations 2.5, 2.2, and 2.3, we see

$$E(\nu, \nu + d\nu) = K_\lambda (fracc\nu)^{\alpha_\lambda} fracc\nu^2 d\nu \tag{2.6}$$

$$E(\nu, \nu + d\nu) = K_\lambda c^{\alpha_\lambda + 1} \nu^{-\alpha_\lambda} \nu^{-2} d\nu \tag{2.7}$$

$$E(\nu, \nu + d\nu) = K_\nu \nu^{-\alpha_\lambda - 2} d\nu \tag{2.8}$$

$$E(\nu, \nu + d\nu) = K_\nu \nu^{-(\alpha_\lambda + 2)} d\nu \tag{2.9}$$

Thus if

$$F(\nu) = K_\nu \nu^{\alpha_\nu} \tag{2.10}$$

then

$$\alpha_\nu = -(\alpha_\lambda + 2) \tag{2.11}$$

In quasars, α_λ is a negative value. This implies the flux density increases as wavelength decreases, and at steeper rates. Since α_λ is often around -1.5, this implies α_ν is often around -0.5.

2.2 Eddington Limit

An understanding of the relationship between black hole mass and quasar luminosity is vital to understanding the structure and physics of a quasar. The total equilibrium luminosity of a quasar is limited by the mass of the central black hole through what is called the Eddington limit. If we assume an equilibrium quasar where the mean radial acceleration is zero and apply Euler's equation of hydrostatic equilibrium, we see

$$\frac{du}{dt} = -\frac{\nabla p}{\rho} - \nabla\Phi = 0 \tag{2.12}$$

where u is the velocity, p is the pressure in the system, ρ is the density, and Φ is the gravitational potential. In a quasar, the pressure will be dominated by radiation pressure

as the density is too low to support other major types of pressure. We express radiation pressure as F_{rad}.

$$-\frac{\nabla p}{\rho} = \frac{\kappa}{c} F_{rad} \tag{2.13}$$

where κ is the opacity. The luminosity of an object bounded by a surface is

$$L = \int_S F_{rad} \cdot dS \tag{2.14}$$

and thus

$$L = \int_S \frac{c}{\kappa} \nabla\Phi \cdot dS \tag{2.15}$$

Using the Poisson equation and Gauss' theorem,

$$L = \frac{c}{\kappa} \int_S \nabla\Phi \cdot dS \tag{2.16}$$

$$L = \frac{c}{\kappa} \int_V \nabla^2\Phi dV \tag{2.17}$$

$$L = \frac{4\pi G c}{\kappa} \int_V \rho\Phi dV \tag{2.18}$$

$$L = \frac{4\pi G M c}{\kappa} \tag{2.19}$$

since

$$\kappa = \frac{\sigma_T}{m_p} \tag{2.20}$$

where σ_T is the Thompson cross-scattering area of an electron and m_p is the mass of the proton. Thus,

$$L_{Edd} = \frac{4\pi G M m_p c}{\sigma_T} \tag{2.21}$$

Using astrophysical values, this indicates

$$L_{Edd} = 1.26 \times 10^{31} (\frac{M}{M_\odot}) Watts \tag{2.22}$$

Typical quasars can have an Eddington ratio (the ratio between the actual luminosity and the Eddington luminosity) between 0.01 and 1.0. Values greater than 1.0 are possible, but not in equilibrium. A 10^8 solar mass black hole with an Eddington ratio of 1.0 has a luminosity of 1.26×10^{39} Watts, or 3.3×10^{12} solar luminosities, or approximately 250 times the luminosity of the Milky Way galaxy.

2.3 Understanding Baldwin Effect Models

The inverse relationship between emission line strength and quasar luminosity is known as the Baldwin Effect. The physical origin of the Baldwin effect is still under debate. Various models have been proposed to explain the origin of the Baldwin Effect. Wu et al. (1983) proposed two possible models. The ionization parameter may decrease with increasing luminosity, or the covering factor may change with luminosity. The covering factor is a measure of the angular area over which the central regions are covered by gas clouds, blocking their direct observation by outside observers. Changes to the ionization parameter with a changing luminosity have been examined primarily in the X-ray region, as in Ricci et al. (2013), but may be applicable in the mid-IR, as in Ricci et al. (2014). Netzer (1985) proposed the inclination of the accretion disk can simultaneously change the luminosity and the equivalent width of emission lines. This hypothesis was expanded upon by Korista et al. (1998).

The origin of the inverse relationship between emission line strength and quasar luminosity continues to be hotly debated within the quasar science community (Osmer & Shields 1999; Baskin & Laor 2004; Marziani & Sulentic 2014; Shemmer & Lieber 2015). Different models of quasar structure predict different functional forms of the Baldwin Effect. The spectral index may change at ionizing photon energies, leading to more or less ionized gas capable of producing specific emission lines. In all cases, both the structure (the disk, the gas, the ionizing photons, the black hole, etc.) and our understanding of the structure (through reverberation mapping, the Eddington Limit, and observations of the spectral index) are important considerations in these models. The black hole mass, the accretion rate, and the spectral index broadly define the diversity of quasars. The Baldwin Effect is the interpretation of that diversity through the relationship between luminosity and line strength.

2.4 Models of the Baldwin Effect

In this work, I examine four models proposed to explain the inverse relationship between emission line strength and quasar luminosity, or Baldwin Effect. These models make predictions based of assumptions of quasar physics. Thus, testing these models can improve our understanding in quasar physics. The four models examined are explained in detail in Wandel (1999a), Wandel (1999b), Korista et al. (1998), and Bachev et al. (2004). Hereafter, these models will be referred to as Wandel99a, Wandel99b, Korista, and the Modified Baldwin Effect, respectively. Wandel99a makes assumptions about quasar

luminosity and spectral index, and uses standard atomic physics to find the slope of the Baldwin Effect. Wandel99b assumes the Baldwin Effect is actually an evolutionary effect and makes predictions from there. Korista uses hydrodynamic simulations to identify the correlation between emission line strength and luminosity and models the slope of emission line strength with respect to luminosity accordingly. The Modified Baldwin Effect theorizes that the Baldwin Effect is not a function of luminosity, but a function of some other observable, such as black hole mass, Eddington ratio, or spectral index. Fundamentally, these models appear very similar, but the slope and curvature differs between models.

2.4.1 Wandel 99a Model

Wandel99a (Wandel 1999a) assumes that quasar luminosity is some amount less than the Eddington luminosity, $L_{Edd} = 1.26 \times 10^{31}(\frac{M}{M_\odot})Watts$, or

$$M_8 = 0.7R^{-1}L_{46} \tag{2.23}$$

where M_8 is $M/10^8 M_\odot$, M is the black hole mass and $M_\odot$ is one solar mass, R is the Eddington ratio or L/L_{Edd}, and L_{46} is $L/10^{46}$ erg s^{-1}, with L being the luminosity of the quasar.

Assuming a disk with constant temperature,

$$L < 4\pi R^2 \sigma T^4 \tag{2.24}$$

Given that

$$E \approx 3kT \approx (10eV)(\frac{T}{10^5 K}) \tag{2.25}$$

combining these gives

$$E \leq (10eV)L_{46}^{1/4} M_8^{-1/2} (\frac{R}{5R_S})^{-1/2} \tag{2.26}$$

where R_S is the Schwarzschild radius, $2GM/c^2$. Or,

$$M_8 \geq E_{ryd}^2 L_{46}^{1/2} (\frac{R}{5R_S})^{-1} \tag{2.27}$$

where E_{ryd} is the average photon energy in rydbergs.

Together, these allow for an estimate of the size of the black hole,

$$\frac{R}{R_S} = 13 L_{46}^{1/2} R E_{ryd}^{-2} \tag{2.28}$$

The variability of the quasar has a minimum timescale of the light-travel time across the black hole.

Wandel99a assumes the release of energy from the black hole is primarily from the release of gravitational potential energy, implying

$$L(R) = \frac{3GM\dot{M}}{8\pi R^3}(1 - (\frac{R_{in}}{R})^{1/2}) \tag{2.29}$$

where $\dot{M}$ is the mass infall rate and R_{in} is the inner disk radius.

Combining these, we can find the radial dependence of disk temperature:

$$T(R) \approx (\frac{3GM\dot{M}}{8\pi\sigma R^3})^{1/4} T(R) \approx 6 \times 10^5 (\frac{\dot{m}}{M_8})^(1/4) r^{-3/4} K \tag{2.30}$$

where $r = R/R_s$. This implies an accretion rate (Eddington ratio) of

$$\dot{m} = \frac{\dot{M}}{\dot{M_{Edd}}} \dot{m} \approx 2(\frac{M}{M_\odot} y r^{-1}) M_8^{-1} (\epsilon/0.1)^{-1} \tag{2.31}$$

The spectrum of a multiblackbody accretion disk is found by integrating over the disk. This integration shows that the highest frequency photons come from the inner edge of the disk.

Using this information, the mean energy of ionizing photons can be found.

$$E \approx (17 - 20eV) L_{46}^{1/4} M_8^{-1/2} \tag{2.32}$$

where the range in energy is due to the difference between nonrotating (Schwarszchild) and rotating (Kerr) black holes, respectively.

An empirical relationship, found from Wandel (1999b), shows the relationship

$$M_8 \approx 0.4 (\frac{L_{46}}{U n_{10}}) \nu_3^2 \tag{2.33}$$

where U is the ionization parameter, n_{10} is the density of the gas in units of 10^{-10} cm^{-3}, and ν_3 is the FWHM of $H\beta$ in 1000 km s^{-1}.

Combining these relationships with other empirical trends gives an equation for Effective Energy

$$E_{eff}(L) \approx E_c L_{46}^{-1/4} \tag{2.34}$$

Assuming a power law continuum, we find that

$$EW \approx exp(\frac{E_I - E_{ion}}{E_c L_{46}^{-1/4}}) \tag{2.35}$$

where E_I is the photon energy at the line and E_{ion} is the ionization energy of that species.

2.4.2 Wandel 99b Model

The Wandel99b model (Wandel 1999b) runs through the above but assumes different accretion models. The accretion models used are Constant Rate, Eddington limited, and Accretion from a homogenous spherical medium. Given a disk temperature model and an accretion rate, the relationship between quasar black hole mass and luminosity is presented.

2.4.3 Korista Model

Korista (Korista et al. 1998) estimates the slope of the equivalent width of emission lines versus quasar luminosity (the slope of the Baldwin Effect) by computationally modeling the accretion disk. That work describes the broad line region using Locally Optimally-emitting Clouds, or LOCs. This model assumes there are many individual clouds with a wide range of densities and sizes. That work uses this model to recreate quasar spectra. They use grids of photoionization models integrated over cloud properties to predict these spectra. The functional form of the model is:

$$log(EW) = \alpha + \beta log(\lambda L_\lambda) \tag{2.36}$$

2.4.4 Modified Baldwin Effect

Bachev et al. (2004) found a relationship between the Eddington ratio and the equivalent width in a sample of quasars even after the effects of luminosity were removed. That work used approximately 700 HST spectra on 141 objects extracted from the Hubble archive. Bachev et al. (2004) created median composite spectra from their sample to determine median line equivalent widths. Holding the luminosity of quasars constant, they found that the equivalent width of C IV fell by a factor of ten as the mass of the central black hole increased by a factor of 100.

A later work, Xu et al. (2008), took 26623 quasars from SDSS-I and found a relationship between the equivalent width and the luminosity, black hole mass, and Eddington ratio. In each case, Xu et al. (2008) found a statistically significant relationship between the observable and the line equivalent width. However, no attempt was made to isolate variables.

CHAPTER 3

DATA

This chapter describes the data used to create the initial composite. Many more composites will be created from these data. This chapter covers the observational surveys from which the data are taken, their target selection schemes, sample selection algorithms, and the flux correction steps.

3.1 Source of the Data

Quasar spectra used to create the composite are obtained from BOSS. Photometry used in calibration and for assessing broad-band synthetic photometry of our quasar composite spectrum were obtained from the imaging programs in SDSS-I, -II, and -III. Additional spectra for calibration were obtained from SDSS-I, -II, and BOSS. Hereafter, photometry and spectra from SDSS-I and SDSS-II are abbreviated collectively as coming from SDSS.

3.1.1 The SDSS Program

Imaging data employed in this analysis were taken in the North Galactic Cap during SDSS I/II (2000-2005), and for the South Galactic Cap in 2000-5 and 2008-9. Data were taken in five photometric bands (Sloan u, g, r, i, and z, Fukugita et al. 1996) by the Apache Point 2.5-m telescope (Gunn et al. 2006). The total imaging area was approximately 14,555 deg^2. All images were taken on dark photometric nights with good seeing (Hogg 2001). The final photometric data for the analysis were taken from SDSS Data Release 8 (DR8; Aihara et al. 2011). Papers on object detection and photometric measurement include Lupton et al. (2001) and Stoughton et al. (2002). Papers discussing the photometric calibration of the SDSS Imaging Program include Smith et al. (2002), Ivezić et al. (2004), Tucker et al. (2006) and Padmanabhan et al. (2008). The astrometric calibration is discussed in Pier et al. (2003). SDSS photometry is converted into AB magnitude Oke & Gunn (1983) data as shown in Table 3.1.

In addition to photometric data, this analysis uses a small sample of spectra obtained in SDSS-I and -II. The details of the spectra are presented in York et al. (2000).

3.1.2 The BOSS Program

The primary science goals of BOSS are to characterize the imprint of the Baryon Acoustic Oscillation (BAO) signal on the spatial distribution of Luminous Red Galaxies and the Lyman-α forest detected from quasar spectra. The BOSS BAO signal was most recently measured for Luminous Red Galaxies in Anderson et al. (2014) and in the Lyman-α forest in Delubac et al. (2015). The quasars utilized in the Lyman-α forest measurements of the BAO provide the basis for the quasar composite spectrum.

3.1.2.1 Quasar Target Selection in BOSS

Objects were selected from SDSS imaging data for BOSS spectroscopy with a goal of obtaining confirmed Lyman-α ($z \geq 2.15$) quasars at a density of 15 deg^{-2}. The selection of quasar candidates for spectroscopic observation is difficult due to large photometric errors in objects at $g = 22$. Additionally, most of the quasars observed are at $2.1 \leq z \leq 3.5$, and the quasar locus crosses the stellar locus at $z = 2.7$ (Fan 1999; Richards et al. 2002). The quasar locus is the region in which quasars are most likely to be found in color-color space. The stellar locus is the region in which stars are most likely to be found in color-color space.

To achieve the desired density of Lyman-α quasars, all point sources identified in the imaging data were passed through a number of different selection schemes. The two primary methods generated the CORE and BONUS samples (Ross et al. 2012). During the first year of operations, the CORE sample utilized the likelihood method explained in Kirkpatrick et al. (2011). Starting in the second year of operations, a method known as Extreme Deconvolution (XDQSO) selection was employed (Bovy et al. 2011). This method attempts to identify a uniform sample by deconvolving quasars from the stellar locus in color-color space after taking into account photometric uncertainties. The BONUS sample is not a uniform sample, but uses ancillary imaging data from a range of sources to maximize quasar density. Quasar candidates in the CORE and BONUS samples contribute 20 and 18.5 targets deg^{-2}, respectively; a few other selections bring the total to 40 deg^{-2}. These selection algorithms produce 15-18 $z > 2.1$ quasars deg^{-2} out to the BOSS magnitude limit of ($g \leq 22$ OR $r \leq 21.85$). In an effort to maintain consistency in the quasar sample, the quasar composite in this paper is generated from only two of these methods: the BONUS sample and the XDQSO subsample from the CORE sample.

Because the quasar locus for high-redshift ($z \approx 2.7$) quasars overlaps with the stellar locus in SDSS color-color space, many objects targeted as quasars are actually stars. These objects were not identified as stars until after the spectra were taken. Thus, we have a

sample of stars that are selected and observed in the same manner as the observed quasars. We call these objects "stellar contaminants"; most are A, F, or G-type stars. These stars tend to exhibit low variability and can be used as a template to test fluxing errors and validate improvements to the flux calibration (see Chapter 3.2.1).

3.1.2.2 BOSS Spectroscopic Observations

Spectroscopic observations with BOSS are performed using plates with a radius of 1.5deg on the sky (Smee et al. 2013). Each plate contains 1000 holes drilled for $2''$ diameter fibers. On each plate, approximately 160-200 fibers are allocated for quasar targets, and 20 fibers are reserved for standard stars chosen from photometric data consistent with main sequence F stars. The holes for each plate are drilled at a position according to the estimated local sidereal time (LST) of the observation to account for hour angle and Atmospheric Differential Refraction (ADR).

Most holes (including those for standard stars) are drilled with a position corresponding to the predicted ADR for the observation to maximize the throughput at 5400 Å. For convenience, we refer to fibers with ADR offsets designed to maximize 5400 Å throughput as the "red focal plane". Since quasar spectra are used to search for the BAO signal in the Lyman-α forest, the decision was made to maximize the flux at the shortest wavelengths of the quasar spectra. Thus, holes drilled for quasar targets were drilled at slightly different positions to maximize throughput at 4000 Å; we call this the "blue focal plane". Quasar fibers in this nomenclature are simply shifted parallel to the true focal plane of the standard stars to account for ADR. Holes drilled in the 4000 Å focal plane more than 1.02deg from the plate center are also augmented with washers to change the vertical position of the fibers to match the 4000 Å focus, causing a true offset from the focal plane (Dawson et al. 2013).

Once observations are completed, the data reduction follows two major steps. First, 1-D spectra are extracted and calibrated from the raw, 2-D CCD data (Stoughton et al. 2002). An integral phase of the extraction and coaddition process is flux calibration based on model spectra for the standard stars. This step introduces a distortion in the broadband flux in spectra observed in the blue focal plane relative to the red focal plane. In the second step of the data reduction, an automated classification and redshift is estimated for each 1-D spectrum (Bolton et al. 2012). One pixel in a BOSS spectrum has a velocity width of $\Delta\, v = 69$ km s^{-1}, or identically a width of 0.0001 in logarithmic wavelength.

In this work, the classification and redshift determination are not derived from the automated data reduction pipeline but instead rely on the visual inspections of all the

potential quasar spectra obtained in BOSS (Pâris et al. 2012). Several techniques to improve the precision of the redshift after visual inspection were used in Pâris et al. (2012, 2014); here, we use the Principal Component Analysis (PCA) redshift technique. The PCA eigenvectors are derived from a representative sample of 8,632 visually inspected quasars with high signal-to-noise ratio, no BAL features, and with redshift determined by the Mg II line.

3.1.3 Sample Selection

This work uses quasar data from the DR12Q catalog, presented in Paris et al (2015). There are 175,294 quasars in the redshift range $2.1 \leq z \leq 3.5$ included in the DR12Q catalog. We restrict the composite to that redshift range to better understand the quasar population utilized for BOSS Lyman-α forest studies. A total of 158,461 of these quasars are from the XDQSO and/or BONUS samples. After removing broad absorption line (BAL) quasars identified by Pâris et al. (2014) and Damped Lyman-α (DLA) quasars using the DLA catalog from Noterdaeme et al. (2012), we are left with 130,512 quasar spectra.

We also ignore all quasars observed at an airmass above 1.2, as the spectrophotometric correction is least certain at high airmass, as shown by the large scatter in the spectrophotometry in Chapter 3.2.1.2. We tested the effect of observed airmass and spectrophotometric errors on the quasar composite and found that a composite generated from quasars observed at an airmass greater than 1.2 had a 5% discrepancy in the shorter wavelengths compared to a composite with the full quasar sample used. Other airmass ranges with an equal number of quasars had discrepancies of 1% or less in the same range. The remaining sample is large enough that removing the 28,000 high-airmass quasars will not significantly negatively affect the final results. In total, 102,150 quasars were included in the composite. These numbers are detailed in Table 3.2. It must be noted that the sample selection for quasars used in the remainder of this work (excluding the creation of this composite spectrum) is not limited by redshift, but it is still limited by the other cuts described here.

3.1.4 Properties of the Final Sample

The first panel of Figure 3.1 displays the absolute magnitude distribution of the quasar sample used to create the composite spectrum; 68% of quasars fall between -24.37 and -26.22 in K-corrected (as in Pâris et al. 2012) i-band absolute magnitude. The second panel of Figure 3.1 shows the i-band absolute magnitude versus redshift distribution of the quasar sample. The median redshift in this sample is 2.457, and the median i-band absolute magnitude is -25.20.

The first panel of Figure 3.2 presents the redshift distribution of the quasar sample used to create the composite spectrum. The sample peaks at $z = 2.3$, where the wavelength range includes coverage to Lyman-β. The second panel of Figure 3.2 shows the number of spectra used for the composite per wavelength pixel. Comparatively few spectra (approximately 20,000) are used to cover the wavelength range less than 1000 Å or greater than 3000 Å. Pixels between 1000 Å and 2000 Å are covered by 90,000 to 100,000 spectra, which is the greatest coverage of any work on quasar composite spectra.

3.2 Flux Calibration

In this Section, we describe the process by which the spectrophotometric errors in BOSS quasar spectra are quantified and corrected. We compare BOSS spectroscopic data to SDSS photometric and spectroscopic data to quantify the errors and test the derived correction. The model for the correction is determined using only BOSS spectroscopy.

3.2.1 Spectrophotometric Errors

Two independent methods are used to quantify the spectrophotometric errors introduced by the quasar fiber hole offsets. In the first method, we calculate the average ratio between BOSS stellar spectra observed in the blue focal plane and the corresponding SDSS spectra for the same objects. In the second method, we compare the imaging data from SDSS to synthetic magnitudes calculated from BOSS spectra observed in the blue focal plane. These techniques are also used to test the spectrophotometric corrections in Chapter 3.2.2.2 and Chapter 3.2.2.4.

3.2.1.1 Spectral Comparison

Approximately 2000 stars targeted as quasars in the blue focal plane of BOSS (which we call "stellar contaminants") have previous spectra from SDSS. These matches are found by locating pairs of objects within $0.36''$ of each other from the DR12 catalog (for BOSS; Alam et al. 2015) and the DR8 catalog (for SDSS; Aihara et al. 2011). This sample is trimmed to include only A-, F-, and G-type stars with no redshift pipeline problems, and a g-band PSF magnitude brighter than 22. The objects satisfying these criteria are visually inspected in both the SDSS and BOSS spectra. Objects with radically different spectra (possibly from bad matching between spectra) and objects with significant and unreasonable flux differences are also rejected. Flux differences were considered unreasonable and rejected if one or more of the following conditions were met:

- A flux ratio of greater than three or less than one third in the region 6000 Å to 6500

Å

- A ratio which changed by more than a factor of three from less than 4500 Å to greater than 8000 Å

- Having a calculated standard deviation of more than 0.5 in the flux ratio over the region 6000 Å to 6500 Å.

After these cuts, 543 objects remained in the catalog.

The ratio of each BOSS spectrum to its corresponding SDSS spectrum provides an independent nonvariable sample by which one can judge changes in flux calibration between SDSS and BOSS. Since SDSS spectroscopy used a shorter wavelength range than BOSS, both sets of spectra are clipped to include only the wavelength range of SDSS spectra (3850 Å to 8500 Å). The ratio between the BOSS and SDSS spectra is calculated for each star as a function of wavelength. The median value of all BOSS/SDSS star ratios is taken at each wavelength bin. This median ratio is shown in Figure 3.3 in red. The BOSS/SDSS ratio is lowest at long wavelengths, corresponding to a deficit in flux in BOSS of roughly 20% relative to SDSS. At shorter wavelengths, the ratio is of order unity, having a peak of about unity at about 4000 Å and declining to either side. In this figure, pixels flagged by the Lyman alpha skymask are masked (Delubac et al. 2015).

3.2.1.2 Quantification by Photometric Comparison

A second test of the spectrophotometric errors involves the difference between the photometry from the SDSS imaging data (using PSF magnitudes) and the synthetic photometry from BOSS spectroscopy.

As in Section 3.2.1.1, we use stellar contaminants for the comparison but no longer restrict ourselves to objects with spectra in SDSS. The corresponding plate for each stellar contaminant is identified, and the median photometric difference is found for each plate in g, r, and i. The median photometric difference is plotted against the airmass at which the BOSS spectra were observed in the first row of panels in Figure 3.4. There is a clear trend in the difference in magnitudes of stellar contaminants. In g, r, and i, BOSS synthetic photometry indicates that BOSS views these stellar contaminants as being dimmer than in SDSS photometry, with a difference that increases with airmass. Only data for filters g, r, and i are shown because these have the most consistent coverage between SDSS filter bandpasses and BOSS spectral coverage. See Table 3.3 for the linear fits to the data. In general we expect a color bias in $g - r$ of 0.059 magnitudes and a color bias of 0.058

magnitudes in $r - i$, corresponding to the offsets observed at the median airmass of BOSS spectra.

3.2.2 Correcting the Spectrophotometric Errors

Having quantified the spectrophotometric errors, we now present an independent, empirical correction to the spectral response of the fibers in the blue focal plane. First, we generate a correction using BOSS spectroscopic information from a series of specially designed plates. Second, we test this correction by comparing synthetic photometry from corrected BOSS spectra to SDSS photometry. Third, we apply a scaling factor to the amplitude of the correction to minimize the color bias of the synthetic magnitudes of the corrected BOSS spectra.

To better understand the fluxing problems in the blue focal plane, a few plates (listed in Table 3.4) were drilled with standard stars in the blue focal plane. The data reduction pipeline was rerun using these standard stars instead of the normal ("red") standard stars. We call this the "blue reduction", whereas the usual data processing is referred to here as the "red reduction". The blue reduction includes 52 plates, each with more than 10 standard stars in the blue focal plane. These standard stars have the same spectral throughput as the quasars to provide direct flux calibration for the blue focal plane. The difference in the standard star spectra between the blue reductions and the red reductions captures the spectral distortion introduced by offsetting the fibers in the telescope focal plane. F_{BLUE} represents the flux of the custom standard stars in the blue reduction, while F_{RED} represents the flux in the red reduction.

3.2.2.1 Parameterizing the Correction

Before comparing the blue reduction to the red reduction, each spectrum is smoothed with a 201-pixel-weighted-mean smoothing routine. A smoothing routine assigns each pixel a value dependent upon the value of nearby pixels. For a weighted-mean smoothing routine, the new value for each pixel is the weighted mean (weighted by the pixel inverse variance) of nearby pixels. In this case, the 201-pixel-weighted-mean smoothing routine uses the nearest 201 pixels. That is, the 100 pixels just below in wavelength, the 100 pixels just above in wavelength, and the central pixel. We then calculate the ratio between the spectrum of each blue focal plane standard star in the blue reduction to the same spectrum in the red reduction. If no correction was necessary, the ratio would reveal a flat continuum valued at one. Figure 3.5 shows the ratio from all standard stars on plate 6149 and the median ratio for that plate. In this case, which is representative of the population of plates, uncorrected

flux errors reach 20% at long wavelengths (broadband 8500 Å), which is similar to the trend in Figure 3.3. This large difference would cause an incorrect interpretation of features such as quasar spectral indices. This procedure is performed for each plate listed in Table 3.4. We refer to the median spectral ratio for each plate as the "plate ratio". Note also the range of flux errors for this single plate; it is this effect that motivated the decision to model σ_{sys} in Section 4.2.2.

At each wavelength interval measured in BOSS spectra, we record the relationship between the plate ratio and the airmass. This relationship is fit assuming a simple linear model that is constrained to intersect a ratio of one at an airmass of one, thus providing no correction where there is no ADR offset between the red and blue focal planes. The slope of the fit with respect to airmass is recorded for each wavelength. An example of one of these fits is presented in the second panel of Figure 3.5. Some plates consistently provided fits that were outliers from the rest of the plates when considered at all wavelengths. Plates that fall more than 3σ from the rest of the sample over more than 40% of wavelengths are rejected, and this process is run once again. A total of 12 plates are excluded by this criterion. These accepted data are then used to correct BOSS quasar spectra in the following manner:

$$F_c(\lambda) = F(\lambda)[S(\lambda)X + I(\lambda)] \tag{3.1}$$

where F_c is the corrected flux density value at a given wavelength, F is the original flux density value at the given wavelength, S is the slope of the fit fixed to one as discussed above, X is the airmass of the plate on which the given quasar was observed, and I is the intercept of the fit discussed above. The best fit value of $S(\lambda)$ is determined at each wavelength using the sample of specially designed plates.

Table 3.4 lists the list of plates used for this analysis. It also reports the dispersion of the plate which is calculated by taking the rms dispersion of all the spectra on a plate at each wavelength from observer frame 5000 Å to 6000 Å, then taking the median of those wavelength-by-wavelength dispersions. Finally, we report the median slope of the ratio spectrum per thousand angstroms.

3.2.2.2 Tests to the Initial Correction

To test the quality of the initial correction developed in Chapter 3.2.2, we rerun the analysis presented in Chapter 3.2.1 on the data after the initial correction is applied. The results of these tests are presented in Figure 3.3 and in the middle row of panels in Figure 3.4.

Figure 3.3 demonstrates that after the correction, the ratio of BOSS to SDSS spectra is close to one for stellar contaminants observed in both programs over most of the spectrum,

but falls to 0.9 at short wavelengths. The average slope of this curve after the correction is 0.0092 per thousand angstroms in the 5000 Å to 7000 Å range.

The second row of panels in Figure 3.4 display the magnitude difference between SDSS imaging photometry and BOSS synthetic photometry after applying the correction. The results of this linear fit are reported in Table 3.3. Evaluating the results at the median airmass of $X = 1.095$, we expect a bias in color in $g - r$ of -0.033 and in $r - i$ of -0.012 magnitudes after the correction. This is a significant improvement over the differences before the correction.

One may expect the fit in each of the g, r, and i bands to have the same value at an airmass of one regardless of the spectrophotometric correction, as there is no correction at an airmass of one. However, this is only true for objects with a flat Spectral Energy Distribution (SED). In this case, the complex structure of the stellar SED, as well as variations in SED between stars, adds a nonlinearity to the correction at higher airmass which changes the slope and intercept of the fit by a small amount. This is the origin of the 0.02 magnitude shifts in the intercept of the fit in the r band and 0.03 magnitudes in the i band.

3.2.2.3 Refining the Initial Correction to Minimize Color Bias

Due to the small number of plates available from the Blue Reduction, we expect statistical uncertainty that is larger than desired for the much larger sample of plates covering the quasar spectra used in the composite analysis. The residual errors are demonstrated in the second row of Figure 3.4 as a population with nonzero slope. The spectrophotometric correction appears to overcorrect the bias introduced by fiber offsets.

We assume that the wavelength dependence of the correction is correct, but the amplitude is too high. We next seek to minimize the broad-band errors by keeping the shape of the correction but reducing its magnitude. The new modified correction is analyzed in the same manner as in Chapter 3.2.1. In particular, the offset between the PSF magnitudes from SDSS and the corrected BOSS synthetic magnitudes at the mean airmass of 1.095 is recorded at each reduced correction. Since one of the main results of this work is a measurement of the spectral index of the quasar sample, we choose to optimize the correction such that the colors measured in BOSS (using synthetic photometry) most closely match the colors measured in SDSS at the median airmass. We record the difference in $g - r$, $r - i$, or $g - i$ after scaling the slope ($S(\lambda)$) across all wavelengths by the same constant factor and identify the scale factor that minimizes the largest color bias (in $g - r$, $r - i$, or $g - i$). The best fit is a scale factor of 0.83, at which the color bias in $r - i$ is equal to 0.0186 magnitudes. The

results after applying this consistent scale factor are shown in Figure 3.4 in the third row of panels. These results include the correction outlined in Section 3.2.2, and the correction amplitude adjustment of 0.83. Also refer to Table 3.3.

3.2.2.4 Performance of the Final Correction

The correction model evaluated at eight different airmasses is presented in Figure 3.6. At an airmass of one, there is no correction, by design; as the airmass increases, the correction becomes more significant. The correction suppresses flux at wavelengths $\lambda < 4500$ Å and increases flux at longer wavelengths. At the average airmass of the quasar sample of $X = 1.095$, the correction at 4000 Å is 0.96 and the correction at 8500 Å is 1.21.

After the correction is applied, the ratio between BOSS and SDSS standard stars is close to one, as shown in Figure 3.6. The slope of the ratio between 5000 Å and 7000 Å is 0.00073 per thousand angstroms. Over this wavelength range, the ratio between BOSS and SDSS is one to the subpercent level. In general we expect a bias in color in $g - r$ of -0.018 magnitudes and in $r - i$ of $+0.019$ magnitudes after this final correction, a significant improvement over the previous results.

3.3 BOSS/SDSS Ratio

In Figures 3.3 and 3.6, a residual offset is visible between the final BOSS corrections and the SDSS spectra after the correction at wavelengths below 4500 Å and exceeding 5% at 3850 Å. To assess the origin of this residual, we derive a median spectrum of the ratio between standard stars observed in BOSS and SDSS. We exclude objects near other photometrically detected objects (objects with the CHILD flag set), as SDSS fibers are larger than BOSS fibers and may have included extraneous light from other objects. Even though these stars provide the reference calibration for both BOSS and SDSS, Figure 3.7 shows the same trend in the BOSS/SDSS spectral ratio below 4500 Å as presented in Figures 3.3 and 3.6. This result indicates the observed residual is not caused by the correction; instead, it is the result of an intrinsic difference between SDSS and BOSS flux calibrations.

Stellar spectral models, such as the Kurucz models, are sensitive to $T_{\rm eff}$ and [Fe/H], especially in the near-UV continuum (Allende Prieto & Lambert 2000). Good standard star target selection must account for this effect by using a set of standard stars with similar properties. We examine the color-color distribution of SDSS and BOSS standard stars and find that the BOSS standard stars are targeted in a more discriminating manner, restricting their range in color-color space compared to SDSS standard stars, as shown in Figure 3.8. We hypothesize this residual offset between BOSS and SDSS flux calibration in

the near-UV is caused by the sensitivity of Kurucz models to differences in T_{eff} and [Fe/H] of the standard stars coupled to the differing populations of stars selected between SDSS and BOSS. Improvements to the stellar models for calibration stars is beyond the scope of this work and left to a future effort.

Margala et al. (2015) take an independent approach to correcting spectrophotometric calibration of BOSS quasars. In that analysis, the effects of ADR across the focal plane are predicted from first principles given optimal guiding, seeing estimates, and plate design. We apply that correction to the same set of stellar contaminant spectra used in Section 3.2.1.1, and create a BOSS/SDSS median ratio spectrum similar to the one shown in Figure 3.6. We compare our correction and the Margala et al. (2015) correction in Figure 3.9. The two deviate most significantly at 3850 Å; the BOSS flux from our analysis is suppressed by 7% relative to SDSS, while Margala et al. (2015) is suppressed by 11%. Over the wavelength range $4800\text{Å} \leq \lambda \leq 8200\text{Å}$, the two corrections agree to better than 1%.

Table 3.1: Conversion from SDSS to AB magnitudes, in the form $\delta m = m_{AB} - m_{SDSS}$.

Sloan Filter	δm
u	-0.042
g	0.036
r	0.015
i	0.013
z	-0.002

Table 3.2: This table shows the number of quasars remaining in the sample after each sample selection criterion is applied.

Criterion	Remaining Quasars
$2.1 \leq z \leq 3.5$	175,294
XDQSO and BONUS	158,461
Remove BAL, DLA	130,512
Airmass ≤ 1.2	102,150

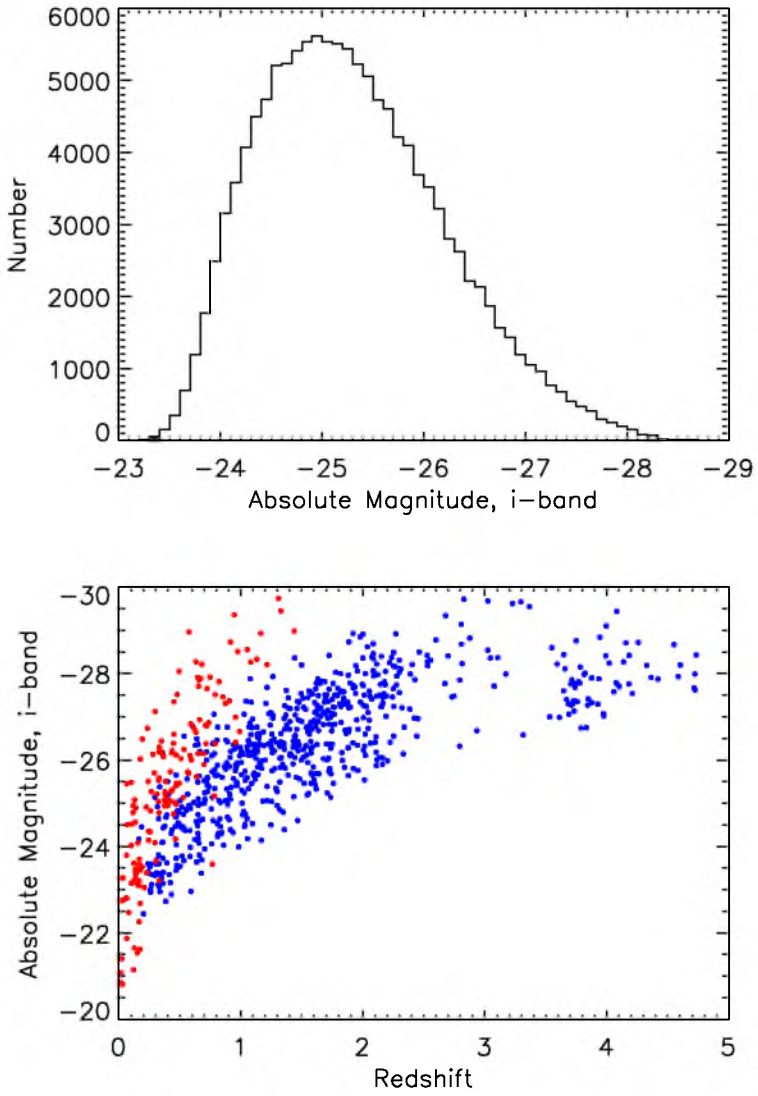

Figure 3.1: Magnitude range of this and similar works. First panel: Absolute i-band magnitude of the sample. Second panel: Absolute i-band magnitude versus redshift for this work (in black), V01 (in blue), and S14 (in red). A representative subsample of quasars in V01 and this work are shown due to the large number of objects in each sample. Due to the large number of quasar spectra used in this work and in V01, only one tenth (randomly chosen) of the quasars are shown here, to avoid clutter.

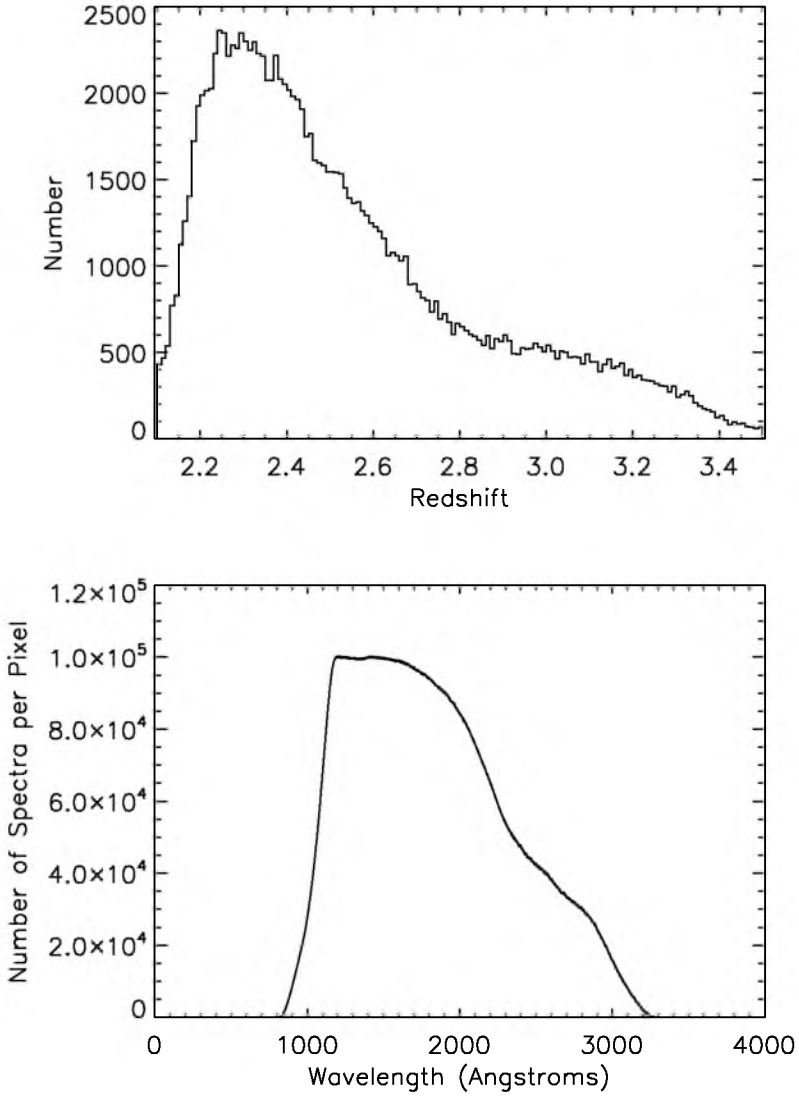

Figure 3.2: Quasar sample data. First panel: Redshift distribution of the sample. Second panel: The number of spectra at each wavelength of the composite.

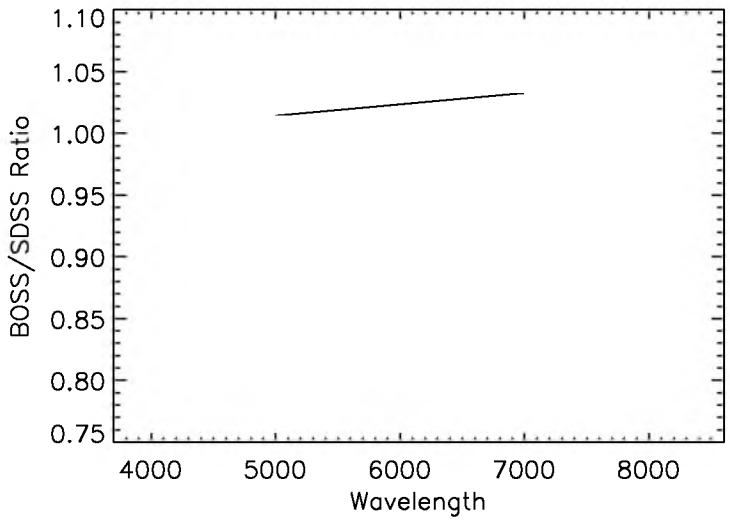

Figure 3.3: The ratio between BOSS stellar contaminant spectra and their counterparts in SDSS as a function of wavelength. The median ratio between uncorrected BOSS and SDSS spectra is shown in red, while the median ratio between BOSS spectra after the initial correction and SDSS spectra is shown in black (see Chapter 3.2.2). A fit to the corrected data ratio is shown in black, with a slope of 0.0092 per thousand Angstroms.

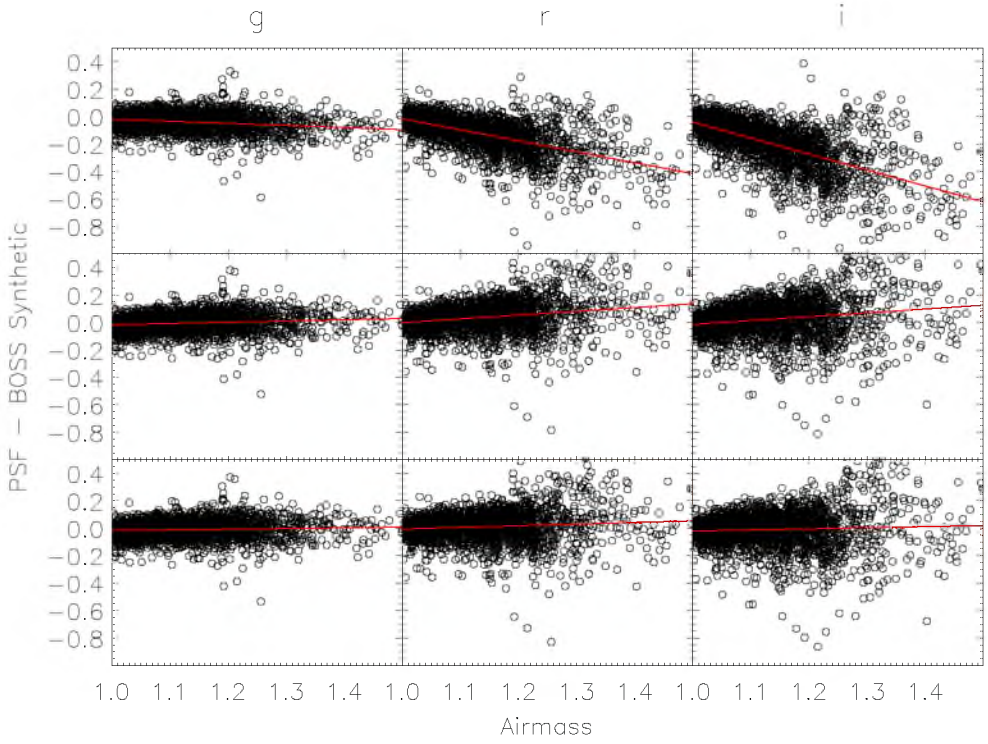

Figure 3.4: The top row shows the difference in magnitudes between SDSS imaging data and BOSS synthetic photometric filters g, r, and i. The middle row shows the difference after applying the initial correction found in Section 3.2.2. The bottom row displays the magnitude difference after the final correction. Fits to these data are listed in Table 3.3

Table 3.3: Data showing the fitted slope, intercept, and color bias at the average airmass of 1.095 for (SDSS PSF magnitudes - BOSS synthetic magnitudes) in the g, r, and i filters. The second column is the characteristic error in magnitude for each filter. The first set of columns is for the uncorrected raw data, the second set of columns shows the values after performing the first round of corrections, and the third set of columns shows the values after the final round of corrections.

Filter	Error	Slope	Intercept	At Mean	Slope	Intercept	At Mean
g	± 0.02	-0.15	-0.02	-0.03	0.05	-0.02	-0.01
r	± 0.03	-0.80	-0.02	-0.09	0.12	0.00	0.00
i	± 0.04	-1.16	-0.04	-0.15	0.08	-0.02	-0.01

Table 3.4: Plates used in making the spectrophotometric correction to the data using the blue reduction.

Plate	Standards	Airmass	RA (deg)	DEC (deg)	Dispersion	Slope
6116	13	1.121	354.5	21.41	0.0231	0.062
6118	11	1.265	337.3	21.36	0.0611	0.227
6119	22	1.281	339.6	21.16	0.0574	0.220
6120	23	1.313	342.2	20.94	0.0479	0.121
6121	17	1.249	344.8	20.71	0.0341	0.149
6125	15	1.223	354.1	19.75	0.0199	0.125
6126	23	1.040	356.5	19.54	0.0115	0.025
6128	12	1.034	345.7	18.72	0.0184	0.011
6130	21	1.121	350.1	18.30	0.0186	0.062
6131	22	1.136	352.3	18.07	0.0259	0.096
6133	15	1.085	357.6	17.73	0.0987	0.064
6136	21	1.177	351.1	16.38	0.0400	0.047
6137	24	1.044	353.5	16.19	0.0233	0.032
6139	21	1.080	358.7	15.96	0.0444	0.107
6140	11	1.219	345.4	15.02	0.0404	0.117
6141	20	1.073	347.2	14.85	0.0267	0.064
6142	22	1.137	349.4	14.67	0.0184	0.078
6146	15	1.186	346.6	13.10	0.0375	0.106
6148	11	1.097	351.1	12.79	0.0284	0.107
6149	23	1.122	353.6	12.65	0.0177	0.120
6157	22	1.097	352.9	10.94	0.0454	0.101
6161	15	1.112	355.2	7.32	0.0634	0.083
6162	17	1.089	346.9	9.43	0.0639	0.080
6163	16	1.090	349.4	9.32	0.0187	0.075
6165	22	1.095	353.8	9.11	0.0746	0.069
6168	11	1.116	347.9	7.55	0.0407	0.027
6169	14	1.114	350.2	7.46	0.0745	0.11
6176	15	1.073	1.6	12.49	0.0396	0.065
6185	14	1.062	5.6	16.19	0.0174	0.0863
6189	11	1.082	5.4	10.83	0.0406	0.0531
6198	19	1.203	10.3	16.58	0.0385	0.0986
6290	27	1.060	341.9	24.81	0.0166	0.0436
6291	20	1.222	338.5	23.21	0.0699	0.130
6296	23	1.159	340.4	26.92	0.0293	0.0608
6297	24	1.148	338.0	27.16	0.0244	0.0799
6298	27	1.241	339.7	25.06	0.0258	0.119
6308	22	1.242	343.3	22.74	0.0172	0.0867
6735	18	1.087	232.7	46.46	0.0182	0.0594
6737	16	1.028	223.7	46.19	0.0275	-0.0141
6752	21	1.031	217.2	46.82	0.0197	0.0206

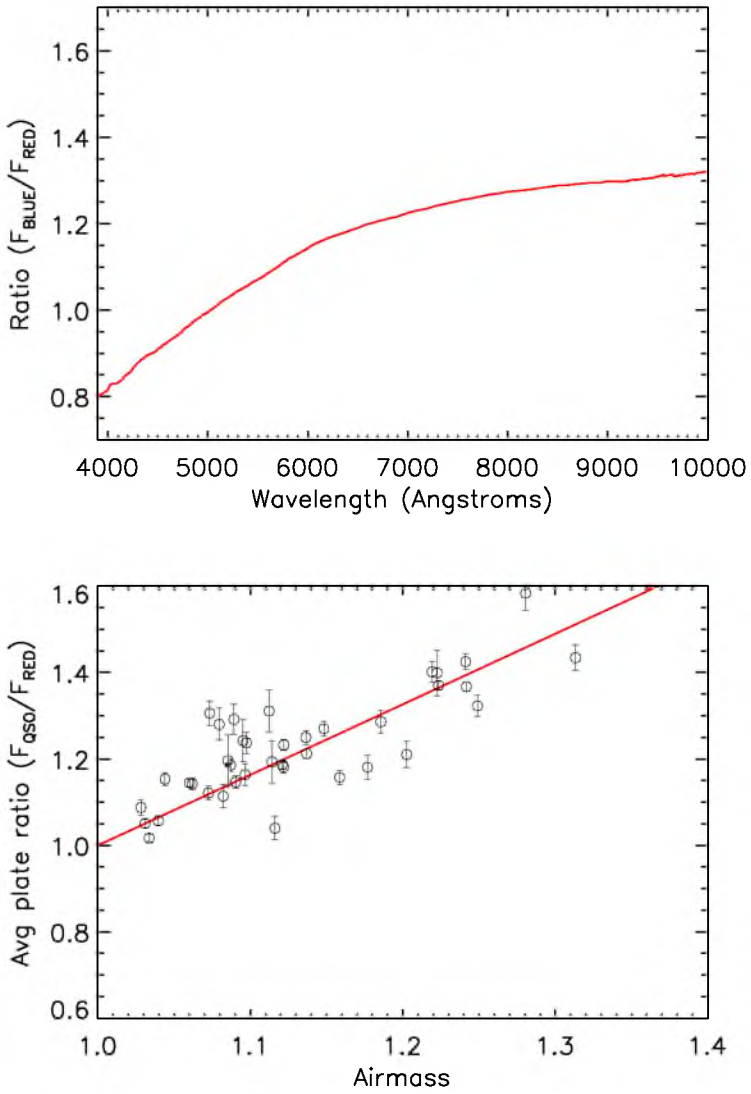

Figure 3.5: Spectrophotometri errors as a function of wavelength. First Panel: the ratio between BOSS and SDSS standard stars on plate 6149 (black) and the median ratio (red) for that plate. Second Panel: A plot of median plate ratios versus airmass at a wavelength of 7133 Å. Circles represent the median plate ratios at this wavelength, and the error bars represent the RMS scatter of that plate at that wavelength.

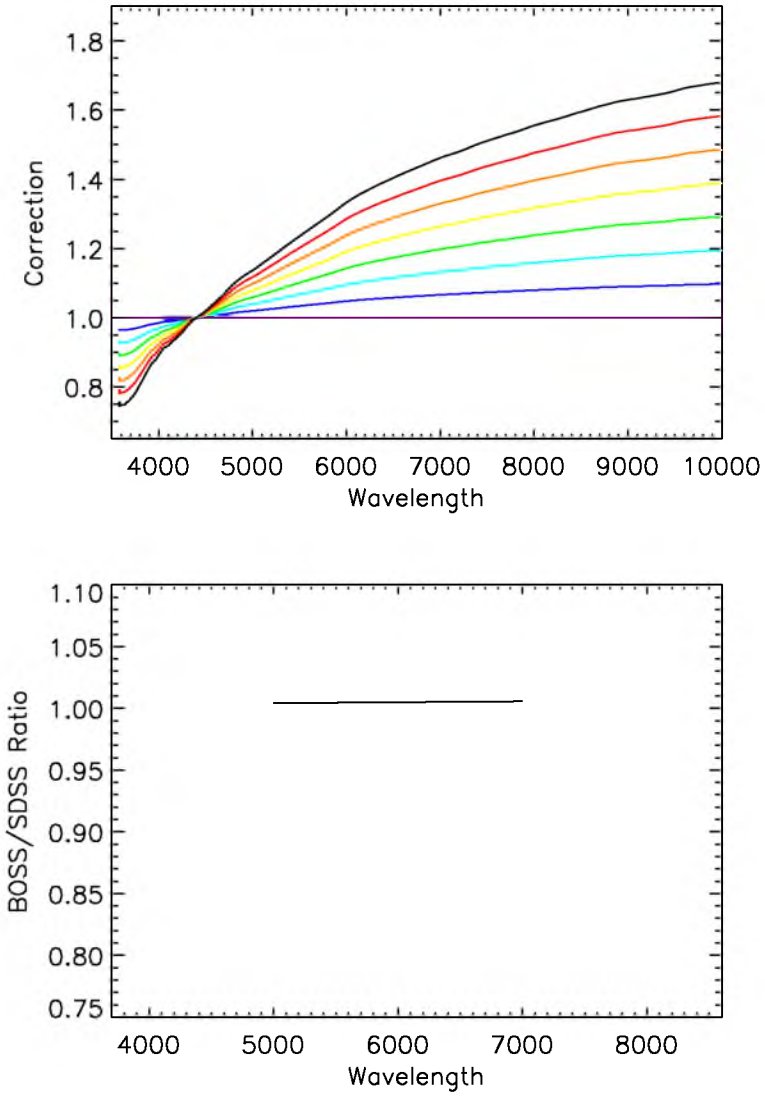

Figure 3.6: The final spectrophotometic correction as a function of wavelength and airmass. First Panel: Example corrections for spectra at different airmasses using the final spectrophotometric correction laid out in Subsection 3.2.2.4. Airmasses of bottom (purple) to top (black) lines: 1.00, 1.05, 1.10, 1.15, 1.20, 1.25, 1.30, 1.35. Second Panel: The horizontal axis is the wavelength in angstroms; the vertical axis shows the ratio between BOSS standard star spectra and their counterparts in SDSS. The median ratio between uncorrected BOSS and SDSS spectra is shown in red, while the median ratio between final corrected BOSS and SDSS spectra is shown in black (see Section 3.2.2.4). The slope of the fit to the corrected ratio, shown as the black line, is 0.00073 per thousand angstroms between 5000 Å and 7000 Å, and the fit at 6000 Å is 1.005.

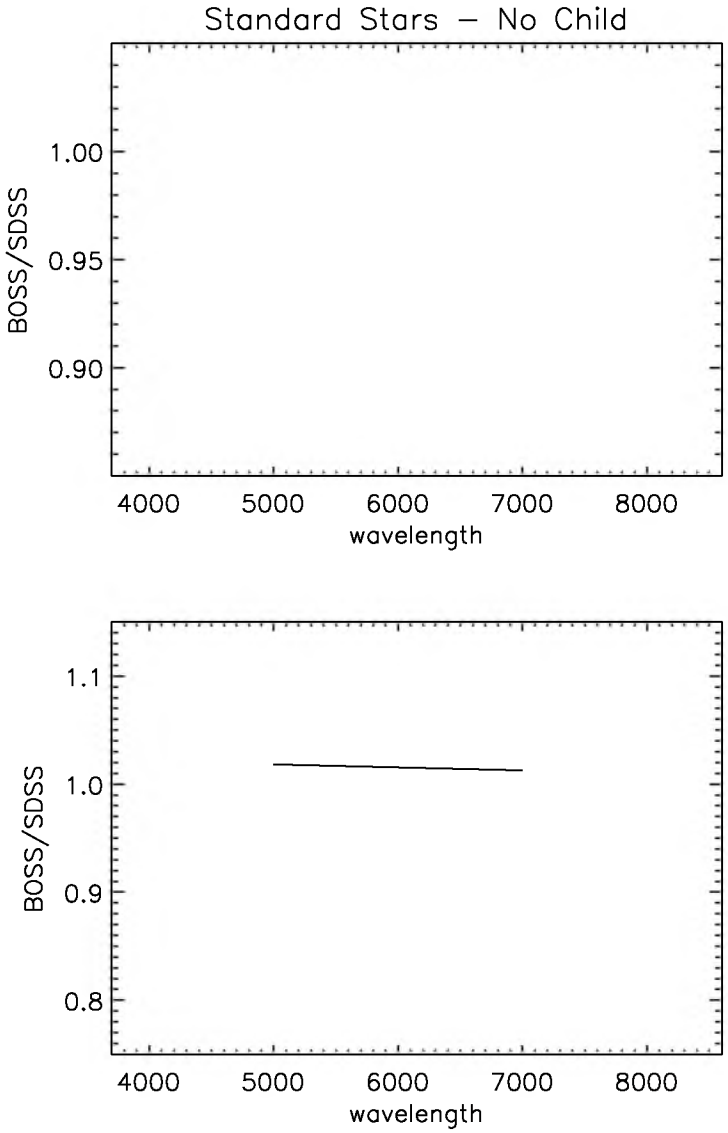

Figure 3.7: Quality of the spectrophotometric correction. First Panel: The ratio between BOSS and SDSS standard star spectra for standard stars at the red focal plane holes. Second Panel: The BOSS to SDSS ratio after the ratio spectrum on the right has been divided out for two cases: before and after the spectrophotometric correction has been applied, with red showing before and black showing after.

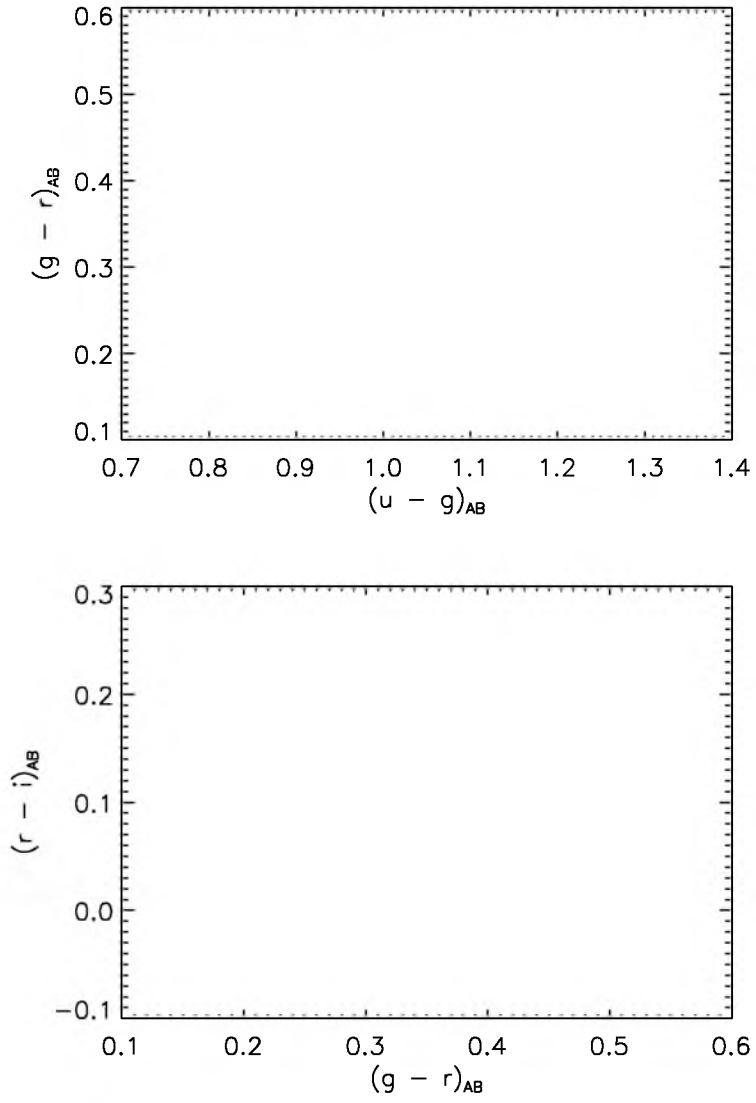

Figure 3.8: Color-color diagrams of the standard stars in SDSS. SDSS stars are shown in black. SDSS stars which also make the color-space cut to be considered as BOSS standards are shown in green.

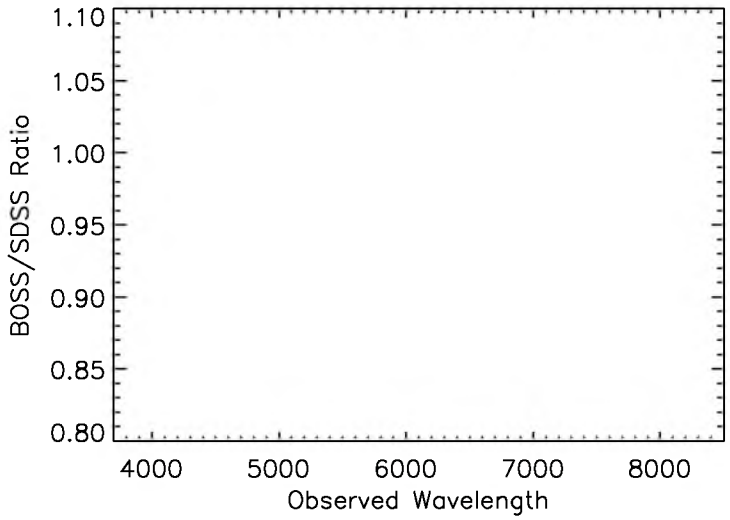

Figure 3.9: The BOSS flux of stellar contaminants relative to the SDSS flux of the same objects as a function of wavelength. The median ratio between BOSS and SDSS spectra corrected using the method in this work is shown in black, while the median ratio between corrected BOSS and SDSS spectra using the correction in Margala15a is indicated in red.

CHAPTER 4

QUASAR COMPOSITE SPECTRUM

In this chapter, we create a quasar composite spectrum from 102,150 quasars observed in the Baryon Oscillation Spectroscopic Survey (BOSS; Dawson et al. 2013), a component of SDSS-III (Eisenstein et al. 2011). These quasars cover a redshift range of $2.1 \leq z \leq 3.5$ and a restframe wavelength range of 800 Å to 3300 Å, and do not include Broad Absorption Line (BAL) quasars or Damped Lyman-α (DLA) quasars. This work differs from previous efforts by increasing the number of quasars and restricting the sample to objects which lie in a smaller region of redshift and i-band absolute magnitude space. This composite can be used in testing theoretical iron line templates (Bruhweiler & Verner 2008) and detecting new quasar spectral lines (Vanden Berk et al. 2000). This spectrum will allow more detailed studies of known quasar spectral lines, including line strengths, line widths, and velocity offsets, which can be used to constrain theoretical models of quasar structure (Grier et al. 2015). The methods discussed here to create a quasar composite spectrum are used to create "master" composite spectra of more than 10,000 quasar spectra. The method used to create quasar composite spectra from fewer than 10,000 quasars is discussed later. This composite spectrum will be used to study quasar spectral diversity.

This chapter discusses the differences between this work and other quasar composite spectra works, explains the assembly of the quasar composite spectrum, and shows that the composite closely recreates the colors of the original quasar sample. This shows the robustness of this method. The final composite spectrum closely matches the spectral features of the sample of quasar spectra, indicating the utility of composite spectra in studies of quasar spectral diversity.

4.1 Previous Quasar Composite Spectra

This work differs significantly from other quasar composite spectrum studies. Primarily, this work seeks to generate a composite spectrum from a very large sample of quasars covering a relatively narrow range of redshifts and i-band absolute magnitudes. In particular, we use quasars intended for BOSS Lyman-α forest BAO studies. Other works have focused

on different ranges in wavelength coverage, different redshift ranges, and smaller numbers of quasar spectra. Recent works are summarized in Table 4.1 and in Figure 3.1. Here we use a narrower interval in i-band absolute magnitude than either V01 or S14. The 68% redshift range is smaller than V01 and comparable to, but slightly larger than, S14, though this work operates at a much higher redshift range than S14.

Because this composite is generated from a tighter sample of quasars than V01 in both redshift and i-band absolute magnitude, this composite will be more representative of quasars falling within its smaller sample selection size. This allows for more detailed studies of quasars within this region, as there is less dispersion between fundamental quasar properties here than in V01. S14 generates a composite from a comparably sized redshift range but at much lower redshift. The i-band absolute magnitude range in S14 is also substantially larger.

As V01 is the most direct predecessor of this work, it is instructive to examine the differences in greater detail. This work differs from V01 in the following ways:

1. This work is more restrictive in classifying an object as a quasar, requiring the object to be a point source. In V01, an object was declared to be a quasar if it was found to be extragalactic (through redshift determination by visual inspection) with at least one broad emission line and had a continuum that was not dominated by stars. This selection includes Seyfert galaxies. V01 also restricted their quasar sample to objects with C IV, Mg II, and/or Balmer line FWHM greater than about 500 km s^{-1}. In this work, quasar identification is made by visual inspection described in Pâris et al. (2012) and uses only objects at $z > 2.1$.

2. This work uses quasars covering a narrower range in redshift and i-band absolute magnitude. The V01 sample drew quasars from the SDSS survey, which used quasars selected from regions in color-color-color-color space ($u - g$, $g - r$, $r - i$, and $i - z$) (Richards et al. 2002). BOSS employs a rigorous quasar target selection scheme which has been shown to be $> 90\%$ complete to $g < 22$.

3. More quasars are included in this work than in V01. V01 used 2204 spectra, whereas this work uses 102,150 spectra, allowing this work to generate a composite at a much higher S/N.

4. The redshifts used in this work are more accurate. V01 redshifts came from two sources. For objects with a visible [O III] line, that line was used for redshift. [O III] is not visible in higher redshift quasars, above $z = 0.7$ in SDSS spectra. A composite of

373 quasars with [O III] redshifts was generated and used as a template to determine the redshifts of the higher redshift quasars. In BOSS a variety of methods largely tested against visual inspection were used (Pâris et al. 2012). For this work, we use PCA redshifts found from the catalog described in Pâris et al. (2012), which is calibrated against Mg II, an emission line not known to display velocity shifts with respect to the systematic redshift.

4.1.1 Constructing the Composite

In this section, we construct the quasar composite spectrum. Quasar spectra are dereddened using the extinction model of Fitzpatrick (1999) and the extinction map of Schlegel et al. (1998). A mask from Delubac et al. (2015) is applied to each quasar to mask skylines. Each quasar spectrum is shifted to the restframe and rebinned by log-linear interpolation to a logarithmic binning scheme with the same pixel width as all BOSS spectra. The quasars in this sample cover a wide redshift range where there is significant evolution in optical depth ($\tau_{\rm eff}^{\rm Ly\alpha}$) due to Lyman-$\alpha$ absorption; however, the exact form of this evolution is unknown and remains a focus of current research (Faucher-Giguère et al. 2008; Becker et al. 2013). We therefore prepare the sample of quasar spectra both with and without a correction for optical depth.

For the composite spectrum that includes a correction for $\tau_{\rm eff}^{\rm Ly\alpha}$, we use the parameterization $\tau_{\rm eff}^{\rm Ly\alpha} = \tau_0 * \sum_{i=2}^{\infty} i^{-1.6}(1+z)^{\beta}$ for each order of the Lyman transition at each pixel in the spectrum. In this formalism, i represents the final energy state of the transition and z is the redshift of that transition at the observed wavelength of the pixel. The sum is performed over all transitions where the wavelength of the transition is longer than the wavelength at that pixel in the rest frame of the quasar. We assume values $\tau_0 = 0.0067$ and $\beta = 3.0$. We assume a correction beyond the Lyman limit that scales as $0.394(1+z)^2 * 0.937 log_{10}[(1+z)\lambda_{\infty}]$, where λ_{∞} is the wavelength of the Lyman limit. Each quasar spectrum is then rescaled at restframe wavelengths $\lambda < 1216$ Å according to the $\tau_{\rm eff}^{\rm Ly\alpha}$ estimates computed for the quasar redshift.

The method employed to create the quasar composite spectrum in this work is based on the method used by V01 and Shull et al. (2012). In both cases, spectra were first ordered by redshift and used to create an intermediate composite each time a new quasar was added. The overlapping region between the composite and the subsequent spectrum was found, and the subsequent spectrum was scaled such that it had the same mean flux as the composite in the overlapping region. This work uses approximately 50 times as many quasars as V01,

thus following the same procedure becomes computationally expensive. Instead, we bin quasars in groups of 500 to reduce the computation time. The quasar composite spectrum is constructed using the following steps:

1. Spectra are ordered by increasing redshift, from lowest to highest.

2. An "overlap region" is chosen for the first 500 spectra. This overlap region covers $\lambda_{\rm blue}$ to $\lambda_{\rm red}$, where $\lambda_{\rm blue}$ is the bluest pixel with measured flux in the 1st spectrum and $\lambda_{\rm red}$ is the reddest pixel with measured flux in the 500th spectrum.

3. The first 500 spectra are individually multiplied by a scaling factor chosen such that each spectrum has a weighted mean of one over the wavelength range $\lambda_{\rm blue}$ to $\lambda_{\rm red}$.

4. For the next 500 spectra a new overlap region (again defined as $\lambda_{\rm blue}$ to $\lambda_{\rm red}$) is chosen. In this case, $\lambda_{\rm blue}$ is the bluest pixel with data in the 1st spectrum, and $\lambda_{\rm red}$ is the reddest pixel with data in the 1000th spectrum. The calculated weighted mean of the first 500 spectra in the overlap region is computed and used as a scale factor by which to normalize each of the following 500 spectra.

5. Each spectrum from the 501st to the 1000th is multiplied by a scaling factor such that the weighted mean of the flux in the overlap region of that spectrum is made equal to the overlap target from the previous step.

6. Every subsequent spectrum is normalized in batches of 500 following the above procedure.

7. After all the spectra are ordered and scaled, the clipped median value at each wavelength is recorded as the value of the composite at that wavelength.

The resulting composite spectrum for the 102,150 quasars is shown in Figure 4.1.

A composite created with the median flux value at each wavelength preserves the line ratios, while a composite created with the geometric mean flux value at each wavelength preserves the mean spectral index of the quasar continuum (see V01). These spectra individually have a low signal-to-noise ratio, and sometimes the recorded flux is less than zero. Thus, a standard geometric mean cannot be used in this case. Instead, we use the median composite spectrum to preserve the line ratios, then distort the composite to match the appropriate spectral index as described in Section 4.2.

Errors are computed through a bootstrap resampling examination of the median. A total of 200 new median composites are made with the same number of quasar spectra

as the main quasar composite, but the quasar sample is taken randomly from the main sample, one at a time, with the possibility of repeats. This is the most computationally expensive aspect of this analysis. The standard deviation of the 200 composite spectra at each wavelength is recorded as the error on the normalized flux estimate at that wavelength. Errors are presented in Figure 4.1 and compared to the errors from V01 in Figure 4.2. This work has approximately half the fractional error of V01 in the region from 2000 Å to 3000 Å. In addition, this work samples the quasar composite at finer wavelength intervals, especially at short wavelengths. Thus, the signal-to-noise ratio per angstrom (rather than the signal-to-noise ratio per pixel) is much higher in this work. At wavelengths blueward of Lyman-α, this work has fractional errors approximately ten times smaller than V01. The mean fractional error between 2000 Å and 2300 Å is 0.11%.

Figure 4.3 shows the composite spectrum generated in this work along with the composites generated by V01 and S14. Most notably, S14 is not constrained by atmospheric absorption of UV light, as data taken for S14 was from the Cosmic Origins Spectrograph (Green et al. 2012) on the Hubble Space Telescope. Thus, S14 can explore the Far and Extreme UV, but their work excludes longer wavelengths as the spectrometer is specifically designed for the UV. S14 recovers flux lost due to $\tau_{\rm eff}^{\rm Ly\alpha}$ by modeling absorption features in individual quasars and restoring the flux based on the estimated H I column density.

These three composites target different ranges of absolute i-band magnitude and redshift, as shown in Table 4.1. This is the primary contributor to the difference between these composites. Some emission lines (C IV, Mg II, C III], and others) have 20-60% greater equivalent widths in this work than in V01. In particular, the reconstructed C IV] and Mg II emission lines have equivalent widths about 60% larger in this work than in V01; C III is about 20% larger compared to V01. These differences originate from the Baldwin Effect (Baldwin 1977), as the ranges of i-band absolute magnitude in each composite spectrum differ. The continuum shape is consistent to the several percent level.

4.2 Spectral Index

For this composite to be useful for studies involving the quasar broad band continuum, we further modify the composite spectrum to have a spectral index consistent with the median spectral index of the full sample of quasars. The spectral index is characterized by fitting a power law to the composite spectrum and to each individual quasar. We confirm the choice of spectral index for the final quasar composite by comparing the spectrum to the photometric colors of the quasar sample as a function of redshift.

4.2.1 Composite and Sample Spectral Index

We use the same rest frame wavelength range for the composite spectrum and for each quasar to determine spectral indices. The wavelength range was chosen after a visual inspection of the composite and of a subsample of individual spectra in the sample. The range of wavelengths we chose to model the quasar continuum is 1440 Å to 1480 Å and 2160 Å to 2230 Å. These two intervals are sufficiently separated from O IV] to avoid contamination from emission lines even in the case of quasars with very broad lines. To determine the spectral index, a simple power law is fit to the flux density and errors in the above range. The spectral index of the composite itself is $\alpha_\lambda = -1.4854 \pm 0.0004$. The error on the median spectral index was found through a bootstrap resampling method. The sample of spectral indices was resampled 200 times to determine the RMS dispersion of the median.

The spectral index of each quasar is measured in the same manner. The median spectral index of the 102,150 quasars in this sample is $\alpha_\lambda = -1.4613 \pm 0.0017$. We then warp the composite spectrum using the simple relation:

$$f(\lambda)_{final} = f(\lambda)_{\rm initial}\lambda^{\delta\alpha} \tag{4.1}$$

where $\delta\alpha$ is the difference between the spectral index of the quasar sample and the spectral index of the composite. This results in a new composite, which is displayed in Figure 4.4.

4.2.2 Quasar Sample Median Spectral Index Binned by Redshift

We next characterize the distribution of intrinsic quasar spectral indices as a function of redshift. The spectral indices for individual quasar spectra were calculated as above and binned by quasar redshift in increments of $\delta z = 0.01$. The true variation in quasar spectral indices contributes only a fraction of the observed RMS dispersion in the population. We assume the three contributions add in quadrature as follows:

$$\sigma^2_{\rm total} = \sigma^2_{\rm stat} + \sigma^2_{\rm sys} + \sigma^2_{\rm intrinsic} \tag{4.2}$$

where σ_{total} is the observed standard deviation in the spectral indices in a given bin, $\sigma_{\rm stat}$ is the median statistical error of the fit, $\sigma_{\rm sys}$ is the systematic error remaining after the spectrophotometric correction, and $\sigma_{\rm intrinsic}$ is the actual RMS dispersion of the spectral indices in the quasar population for that redshift bin.

The systematic error ($\sigma_{\rm sys}$) of the spectrophotometric correction is found in a study of the ratio between BOSS and SDSS spectra of the same stellar contaminants. The selection algorithm to choose appropriate stars for the comparison is described in Section 3.2.1.1.

These ratios between BOSS and SDSS stars are called "star ratios" and should be identically equal to one at all wavelengths. The spectrophotometric correction used on each quasar spectrum in the composite is applied to the BOSS spectra before computing the ratio.

A spectral index is fit to each star ratio spectrum over the wavelength ranges that would correspond to a quasar at $2.1 \leq z \leq 2.64$ in bins of 0.01. The fit continues only to $z = 2.64$ because the star ratio spectra are truncated at the maximum SDSS wavelength of approximately 8500 Å. The weighted median spectral index at each redshift increment is also determined. The systematic error ($\sigma_{\rm sys}$) is found with the following formula:

$$\chi^2_{\rm red} = \frac{1}{N-1} \sum_i \frac{(\alpha_i - \alpha_{\rm median})^2}{\sigma^2_{\rm fit,i} + \sigma^2_{\rm sys}} \tag{4.3}$$

where $\chi^2_{\rm red}$ is the reduced χ^2, N is the number of quasars in each bin, α_i is each spectral index of the i^{th} quasar, $\alpha_{\rm median}$ is the median spectral index in the given redshift bin, $\sigma_{\rm fit,i}$ is the uncertainty in the fit to the spectral index of the i^{th} quasar, and $\sigma_{\rm sys}$ is the systematic error. In each redshift bin, the value of $\sigma_{\rm sys}$ is computed such that $\chi^2_{\rm red} = 1$. We repeat the process until successive iterations converge on the same values of $\alpha_{\rm median}$ and $\sigma_{\rm sys}$ to $< 1\%$ tolerance. The final value of $\sigma_{\rm sys}$ is taken to be the systematic error of the spectrophotometric correction in a given redshift bin. The parameter $\sigma_{\rm intrinsic}$ is found to range between 0.2 to 0.5, generally declining at higher redshifts.

The median spectral indices of the quasars used in this work, binned by redshift, are shown in Figure 4.5. The median spectral indices vary from approximately $\alpha_\lambda = -1.45$ ($2.1 \leq z \leq 2.6$) to $\alpha_\lambda = -1.40$ ($2.7 \leq z \leq 3.5$). There is an apparent trend with magnitude, but we hesitate to attribute that trend to redshift evolution in the spectral index. Because flux calibration uncertainty can introduce broadband errors, it is possible that the trend is simply due to the residual errors in synthetic photometry on $g - r$ and $r - i$ presented in Table 3.3. In fact, the blue residual in $g - r$ would introduce a bias toward more pronounced spectral indices for the lower redshift quasars, and the red residual in $r - i$ would introduce a bias toward less pronounced spectral indices at higher redshift, exactly the trend that is shown in Figure 4.5. The biases in these two color measurements are of order 0.02 magnitudes, which in fact could cause larger trends in spectral index than seen here. However, given the uncertainty in the exact form of the residual fluxing errors, we are unable to improve the flux calibration any further in this analysis. We reserve that effort for future pipeline development by the BOSS team.

4.2.3 Comparing Spectral Index to Quasar Color

In each redshift bin, a broadband correction described by a power law is applied to the composite spectrum such that the composite has the same spectral index as the median of the quasar sample at that redshift. We do the same to warp the composite spectrum to match the spectral index at the $+1\sigma$ and -1σ bounds of the distribution of spectral indices in each redshift bin. We only have accurate estimates of the distribution of the spectral indices over $2.1 \leq z \leq 2.64$, so for higher redshifts we assume the same range of α_λ as that in the $z = 2.64$ redshift bin. As described in Section 4.1.1, the quasar composite spectrum has been corrected for the mean optical depth of the Lyman-α forest region. No correction has been made to the photometric data to account for mean optical depth, so we model the suppression due to mean optical depth of neutral hydrogen by applying the same model as that presented in Section 4.1.1 to the $\tau_{\rm eff}^{{\rm Ly}\alpha}$-corrected composite.

The synthetic $u-g$, $g-r$, $r-i$, and $i-z$ colors of these modified composites for each redshift bin are presented in Figures 4.6 and 4.7. Also displayed are the median photometric colors and the standard deviations of the imaging sample in each redshift bin.

Figure 4.8 shows the trend in $u-g$ against $g-r$ of the spectral index and optical depth corrected composite and displays the stellar locus for comparison. The colors indicated here are found in the same manner as above. Here, the data for the composite synthetic photometry are ignored at redshifts above 3.0 for the reasons stated above concerning the discrepancy in u magnitude.

The colors of the composite spectra reproduce the photometric colors of the quasar sample across most of color and redshift space remarkably accurately. In $g-r$ at a redshift of $3.2 \leq z \leq 3.5$, we see an offset of 0.15 magnitudes likely caused by incorrect modeling of mean optical depth of the Lyman-α forest. In most colors, the difference between photometric and synthetic photometric data increases in the vicinity of $z = 2.7$ (in $u-g$ by -0.2, in $g-r$ by -0.03, in $i-z$ by $+0.06$, and in $r-i$ the difference is consistent with the scatter between bins). At this redshift, the quasar locus approaches the stellar locus as shown in Figure 4.8. As the quasar target selection schemes tend to avoid objects near the stellar locus, the quasars targeted at this redshift may not be as representative of the full quasar population around this redshift. In $u-g$, the offset between the observed photometry and the synthetic photometry of the modified composite begins to grow around a redshift of 2.9 to approximately 0.5 magnitudes. This behavior likely appears because the photometric bandpass extends to shorter wavelengths than the synthetic photometry and the two measurements have differing sensitivity to quasar flux beyond the Lyman limit at

912 Å. In addition, the composite is poorly constrained at $\lambda < 912$ Å as shown in Figure 4.4 by the nonphysical break in continuum at short wavelengths in the composite spectrum that has been corrected for $\tau_{\rm eff}^{\rm Ly\alpha}$. This result could potentially be improved with better models for absorption of ionizing photons over the redshifts covered by the BOSS quasar sample.

4.3 Spectral Features

Having completed the characterization of the continuum to show that the broad band colors of the quasar spectrum are consistent with quasar photometry, we now investigate quasar spectral lines. The high signal-to-noise quasar composite spectrum allows for detailed investigation of these lines, a comparison to previous work, and the identification of new faint lines.

4.3.1 Line Fitting

Measurements of line features are subject to assumptions of continuum modelling and complexity in line structures such as those in the Fe complex. The work here represents one specific approach to estimating continuum and parameterizing line profiles. While the fits performed here appear to describe the lines quite well, we encourage the readers to make their own fits to the composite spectrum for lines of special interest. In particular, we note that the fit in the C III] region is complicated by multiple blended features and a series of known Fe III lines that we were unable to resolve.

We proceeded to measure the line profiles in a semimanual fashion. We measured each line and its underlying continuum independently, adding additional parameters to the fit when there was clear blending upon visual inspection. In some cases, the additional parameters resolve blended lines with different central wavelengths. In other cases, such as *Ly*α, multiple components with effectively the same central wavelength but different widths are required to describe a single emission line. Our procedure for fitting each line is as follows:

1. Two continuum-fitting regions are identified in the vicinity of the line. Each region is typically 5 Å wide. These regions are separated by the centroid of the line by at least one FWHM. The continuum-fitting regions are visually inspected to ensure the absence of faint lines and to ensure an appropriate approximation of the local continuum. A power law is fit to the composite spectrum over the wavelength regions identified to model the continuum.

2. The line region is fit with a single Gaussian. A wavelength range (typically covering a

wavelength region spanning twice the FWHM) is chosen to perform the fit of the line. A single Gaussian fit is first performed and visually inspected to ensure that emission line wings are well described.

3. If clear residuals are found by visual inspection, a second Gaussian is introduced to improve the fit. Likewise, additional Gaussians are introduced until there are no obvious residuals. In cases of slightly blended lines, these additional parameters allow us to accurately describe the individual components of overlapping lines. In the case of complex line profiles, these additional parameters allow us to separate broadline regions with velocity offset and/or varying dynamics into discrete components.

4. We begin at the bluest region of the spectrum and continue until 3000 Å, where the composite spectrum begins to show degradation.

The results of the line fitting are reported in Table 4.2. In that table, we list the properties of the detected lines in the rest frame, followed by the central wavelength, equivalent width, and the Gaussian RMS width associated with each component of the fit. In total, 40 distinct emission features were identified. Of those, nine features were blends that we were unable to resolve. The six strongest features (Lyβ / O IV, Lyα, Si IV/O IV, C IV, C III], Mg II) each required multiple components to accurately describe the line profile.

4.4 Discussion of the Composite

This work presents a very high signal-to-noise quasar composite spectrum using 102,150 BOSS quasar spectra. The spectra used to create this composite spectrum are a uniform sample with $2.1 \leq z \leq 3.5$, excluding BALs and DLAs, and an observed airmass less than 1.2. The large number of quasar spectra used in this work and the uniformity of the sample represent a significant improvement over previous works, such as V01, and samples a different wavelength range than other recent works, such as S14.

The composite spectrum is shifted to match the median spectral index of the Lyman-α forest sample after performing spectrophotometric corrections. The spectrophotometric corrections are parameterized on only airmass and reduce the color bias to less than 0.02 magnitudes. The measured spectral index of -1.4613 ± 17 differs from some other studies (Wilhite et al. 2005; Ruan et al. 2014), most likely due to sampling a different region of redshift-luminosity space. We examine the properties of this composite and the initial

sample in color-color space to show that the synthetic photometry of this quasar composite spectrum closely recreates the photometry of the quasar sample.

Future work will include the examination of luminosity-redshift binned subsamples, searching for trends in quasar properties in luminosity and redshift, and thus trends in quasar evolution. Differences between normal and BAL quasars can be examined by making composites from these subsamples. In general, the composite we have created can be used to study relative line strengths, widths, and velocity offsets in quasars at z 2.5, opening up new avenues to the study of quasar structure at high redshift. New lines may also be detected in this composite, as the signal-to-noise ratio is significantly better than in other works. Theoretical iron templates can be tested against this composite.

Table 4.1: The respective ranges of redshifts and K-corrected i-band absolute magnitudes in recent composites, including this work. Also included is the equivalent width of the C IV emission line in each composite.

	Redshift			Abs. Mag.			
Composite	16%	Median	84%	16%	Median	84%	C IV EW (Å)
V01	0.679	1.472	2.298	-24.47	-26.38	-27.75	77.0
S14	0.104	0.366	0.717	-23.12	-25.32	-27.51	36.3
This Work	2.249	2.457	2.895	-24.37	-25.20	-26.22	48.5

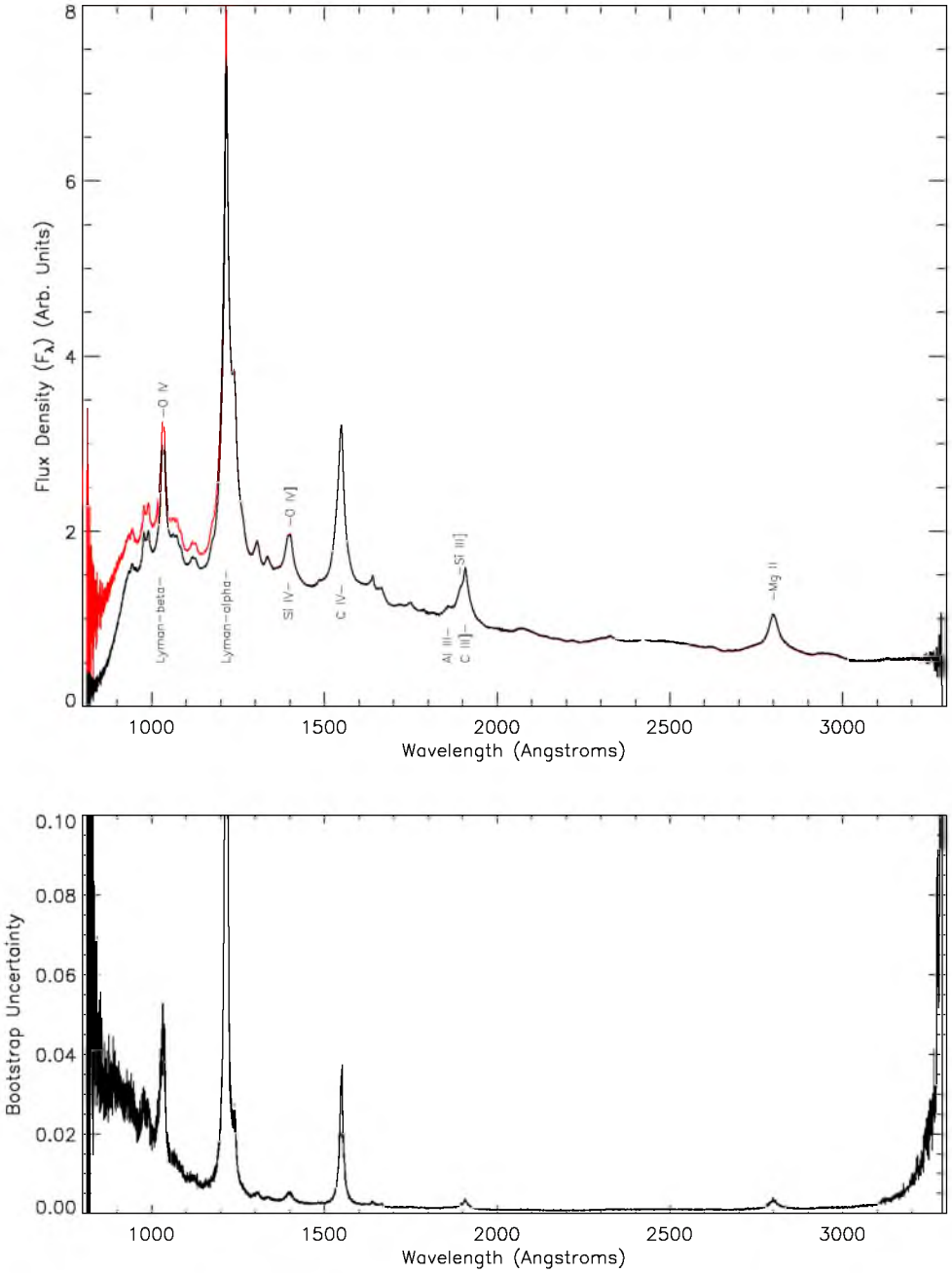

Figure 4.1: The initial composite generated by this work. First panel: The composite without optical depth correction is shown in black, and the composite with optical depth correction is indicated in red. This composite spectrum has not yet been warped to match the median specral index of the quasar sample, as performed in Section 4.2 and shown in Figure 4.4. Second panel: The fractional error of the median flux measurement in each pixel, generated by the bootstrap resampling method. The creation of the composite and the error array are discussed in Section 4.1.1.

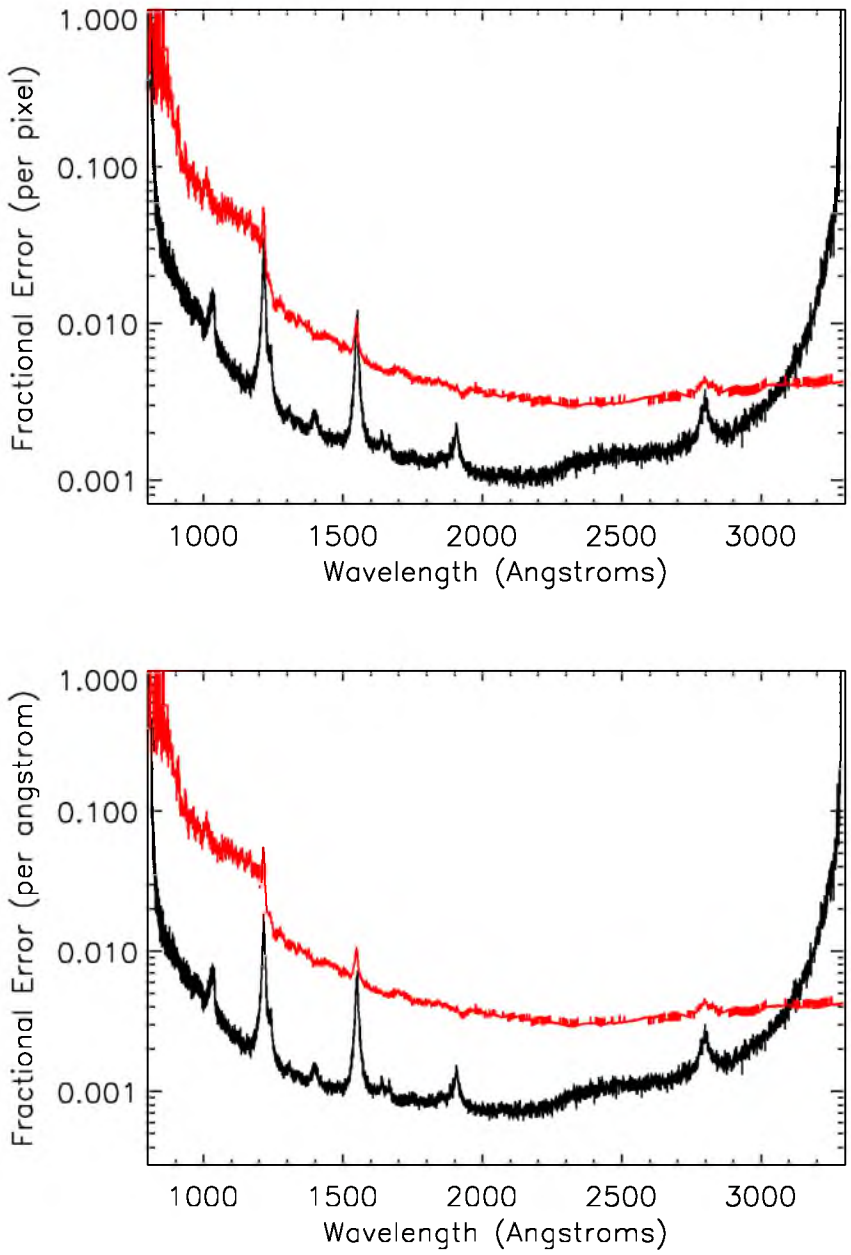

Figure 4.2: Comparison between fractional errors in V01 (red) and this work (black). First Panel: The errors in this work are as small as 0.001 in the continuum, and are smaller than V01 at almost all wavelengths, the exception being at greater than 3160 Å, which is at the red edge of the wavelength range of the BOSS Lyman-α forest sample. Second Panel: Fractional error scaled by the square root of the relative pixel scales.

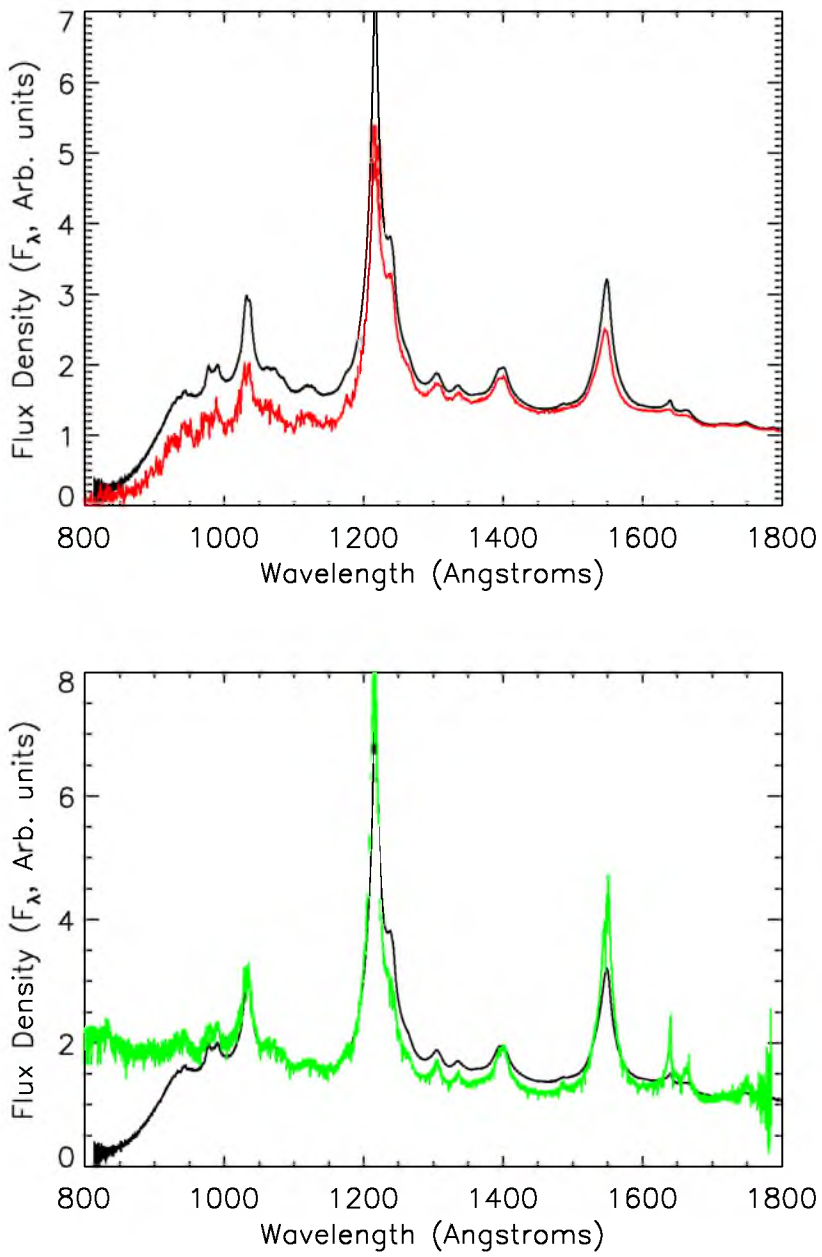

Figure 4.3: Comparison between the quasar composite spectrum generated in this work to other recent works. First Panel: Comparison between the quasar composite spectrum generated in this work without optical depth correction (in black) and V01 (in red). Second Panel: Comparison between the quasar composite spectrum generated in this work without optical depth correction (in black) and S14 (in green). The quasar composite spectrum generated in this work has been warped such that the spectral index of this composite spectrum is the same as the median spectral index of the quasar sample, as explained in Section 4.2. Arbitrary scaling factors have been applied to V01 and S14 for illustrative purposes.

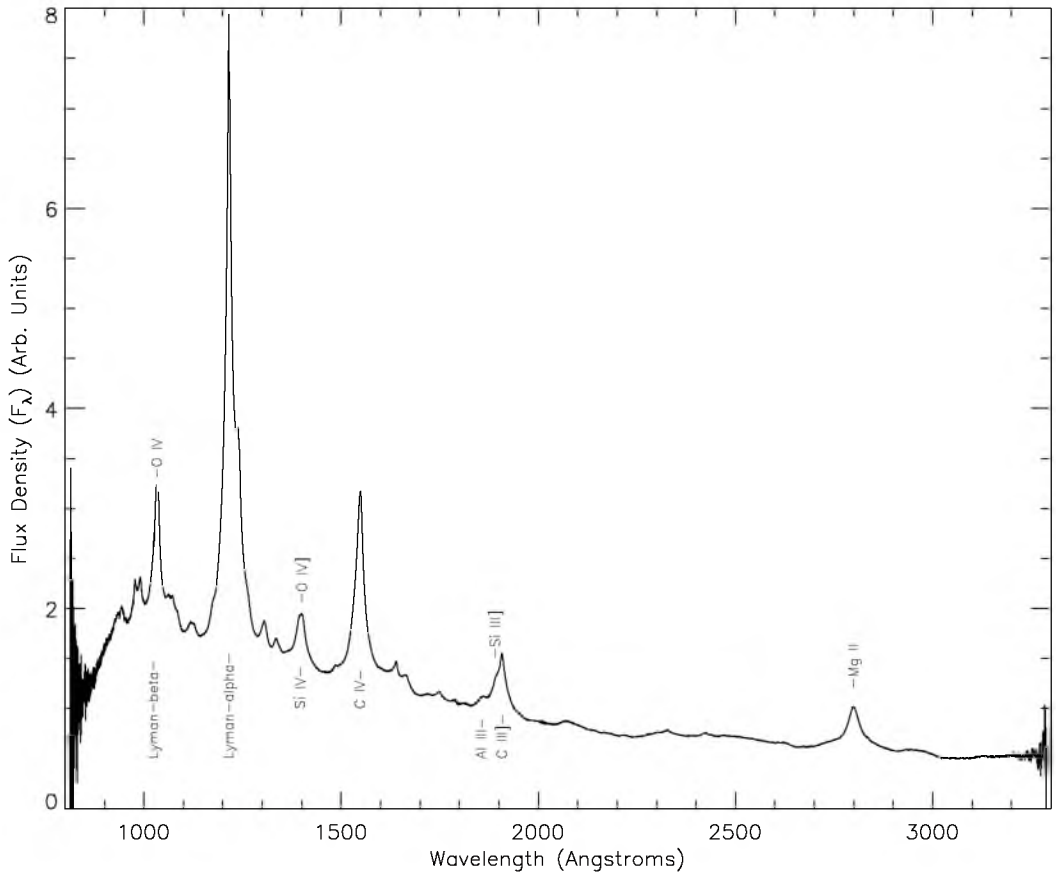

Figure 4.4: Optical-depth-corrected quasar composite spectrum after having been warped to match the median spectral index of the quasar sample as described in Section 4.2.1.

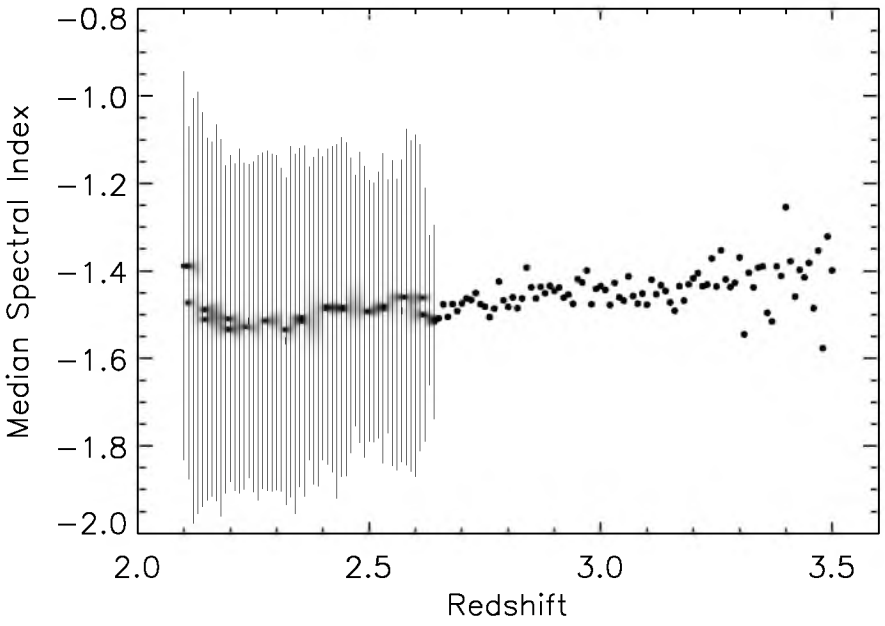

Figure 4.5: Median spectral index of quasars, binned by redshift. The median spectral index is unitless and measured relative to the flux.

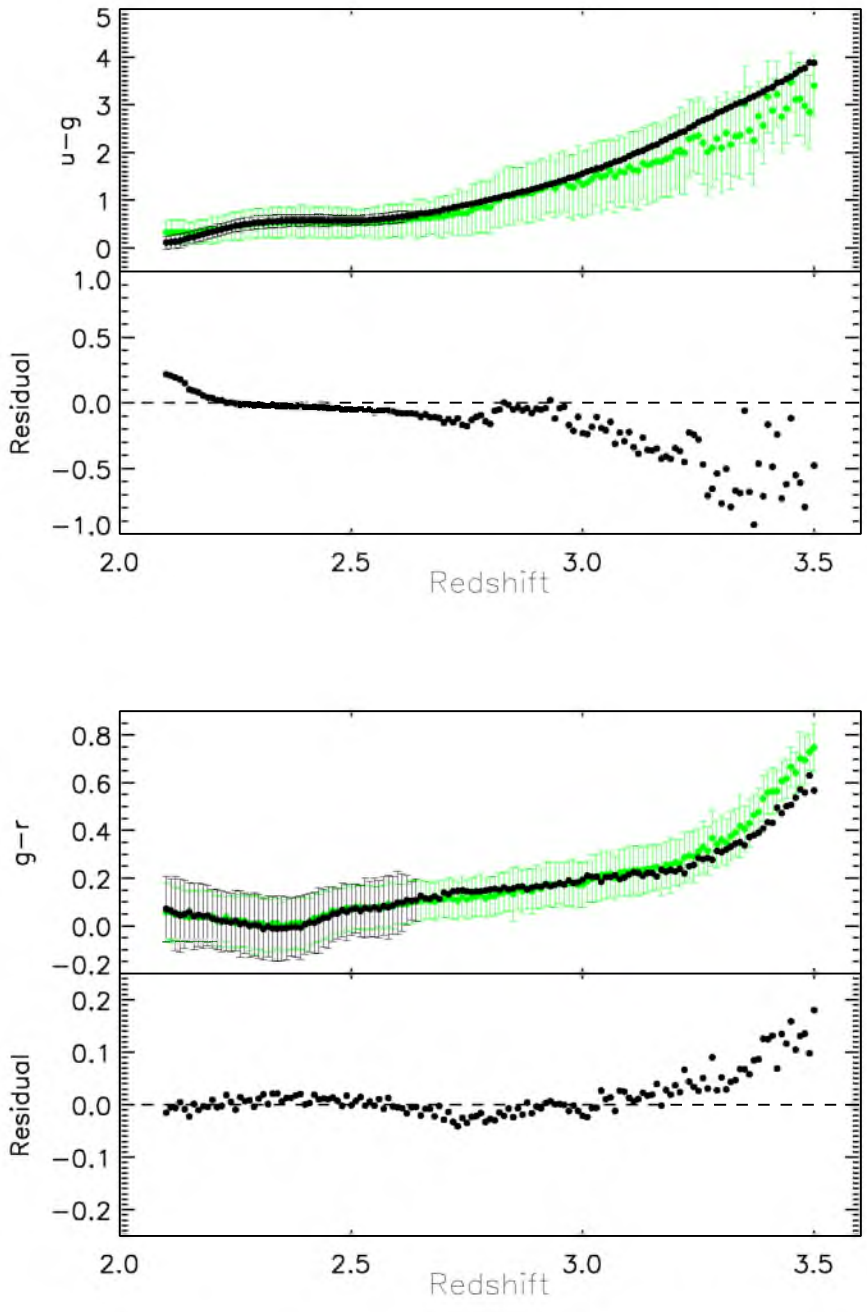

Figure 4.6: The progression of the composite through color-redshift space. The photometric color of the quasar sample is shown in green, along with the $+1\sigma$ and -1σ of the distribution. The synthetic colors of the spectral-index-matched composites are shown in black, along with the synthetic colors of the spectral-index-matched composites of the $+1\sigma$ and -1σ of the distribution of the actual quasar sample. First Panel: $u-g$. Second Panel: $g-r$.

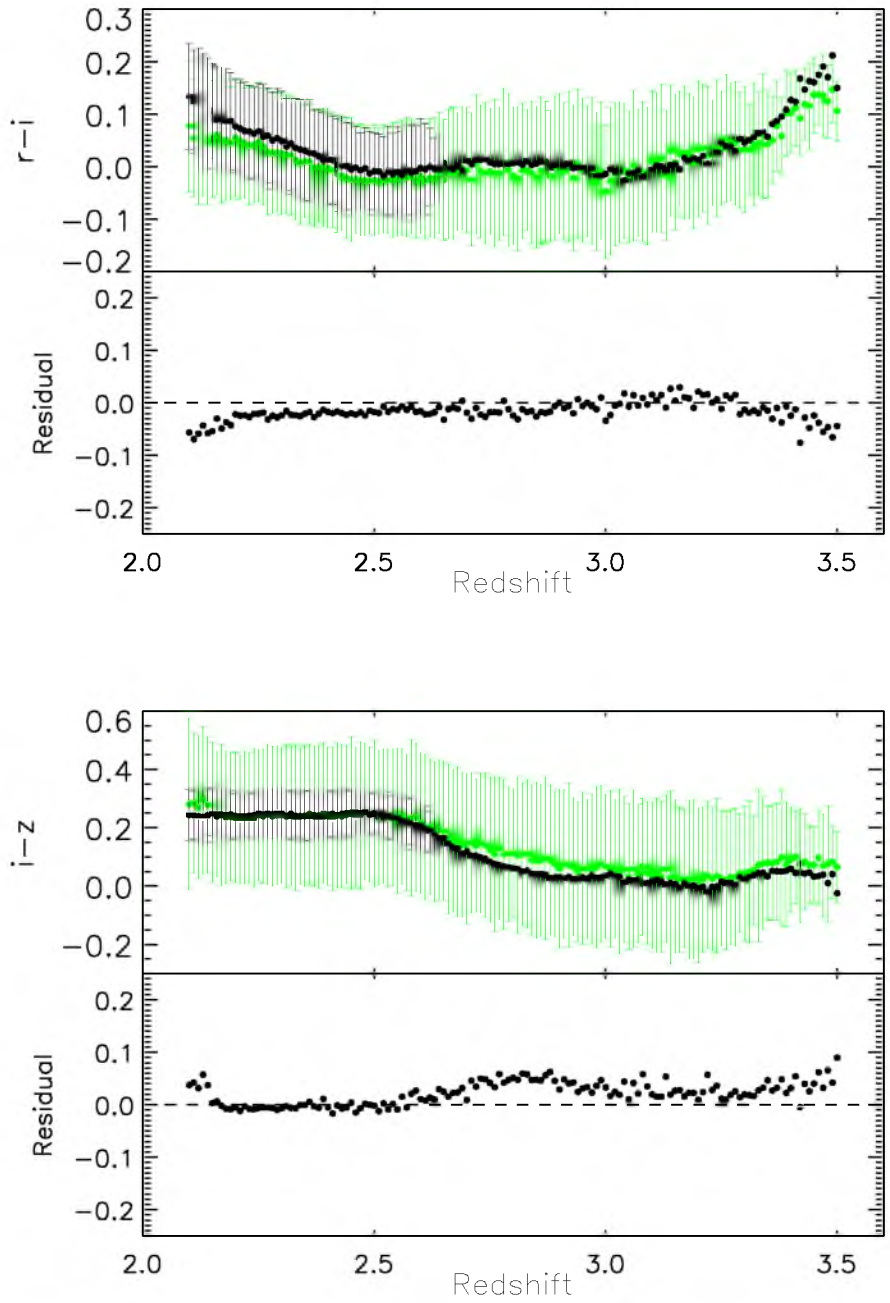

Figure 4.7: The progression of the composite through color-redshift space. The photometric color of the quasar sample is shown in green, along with the $+1\sigma$ and -1σ of the distribution. The synthetic colors of the spectral-index-matched composites are shown in black, along with the synthetic colors of the spectral-index-matched composites of the $+1\sigma$ and -1σ of the distribution of the actual quasar sample. First Panel: $r - i$. Second Panel: $i - z$.

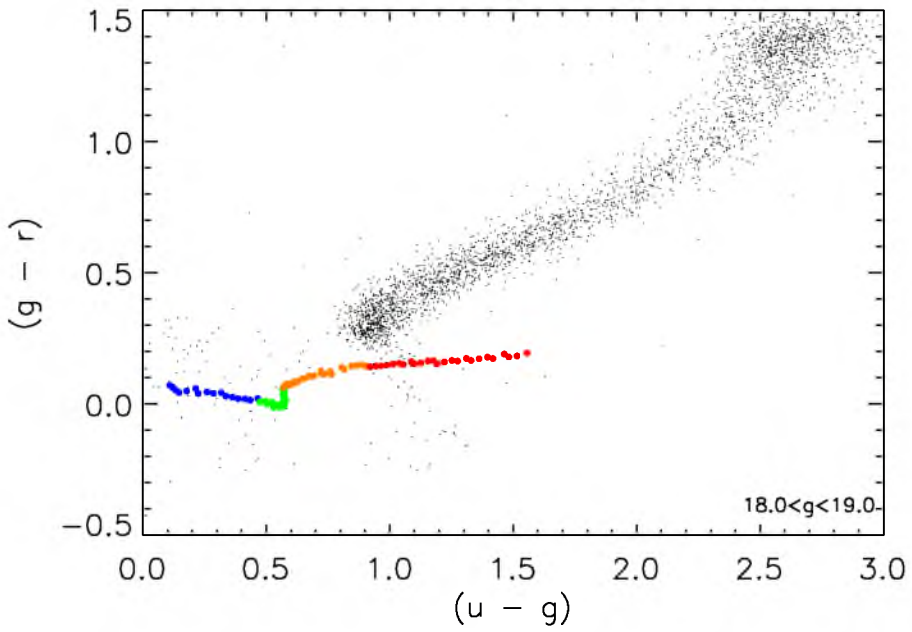

Figure 4.8: The progression of the composite through $(g-r)$ versus $(r-i)$ color-color space. The composite at $2.1 \leq z < 2.25$ is shown in blue, green indicates $2.25 \leq z < 2.5$, orange indicates $2.5 \leq z < 2.75$, and red indicates $2.75 \leq z \leq 3.0$. The black dots indicate stellar colors from SDSS photometry.

Table 4.2: Emission lines detected in the composite spectrum generated in this work compared to known wavelengths and the measurements from V01. Entries that required multiple fits to describe the emission feature are listed with an additional suffix (e.g. Lyα-1 and Lyα-2). Blends are presented with each discrete component in the lab frame and by the multiple components in the observed data (e.g. Si IV / O IV).

Lab ID	Lab λ	λ	Equivalent Width	σ	ID
Lyϵ	937.80	942.66	1.50 ± 0.07	5.33	Lyϵ/Lyδ
Lyδ	949.74				
C III	977.02	977.74	1.53 ± 0.03	4.12	C III
N III	990.69	989.73	1.50 ± 0.03	4.14	N III
Lyβ	1025.72	1031.48	13.53 ± 0.10	13.15	Lyβ / O VI-1
O VI	1033.83	1034.07	4.26 ± 0.15	4.84	Lyβ / O VI-2
unknown	1062.7	1064.01	2.90 ± 0.04	7.66	unknown
unknown	1073.0	1073.53	0.71 ± 0.08	3.51	unknown
N II[a]	1083.99	1083.31	1.32 ± 0.04	5.32	N II
Fe III	UV 1	1117.85	0.76 ± 0.07	5.26	Fe III
Fe III[b]	UV 1	1127.55	0.46 ± 0.06	4.11	Fe III
C III	1175.7	1174.91	2.49 ± 0.01	7.68	C III
Lyα	1215.67	1215.86	19.08 ± 1.03	4.85	Lyα-1
		1216.94	66.63 ± 4.01	16.56	Lyα-2
N V	1240.14	1241.73	9.22 ± 0.02	6.89	N V
Si II	1262.59	1260.81	4.47 ± 0.008	7.91	Si II
O I	1304.85	1305.31	1.73 ± 0.02	5.74	Si II/O I
Si II	1306.82				
C II	1335.3	1335.43	0.77 ± 0.01	4.73	C II
Si IV	1396.76	1398.16	5.07 ± 0.12	19.54	Si IV/O IV-1
O IV	1402.06	1398.22	5.01 ± 0.17	8.81	Si IV/O IV-2
N IV][a]	1486.5	1485.50	0.15 ± 0.01	3.25	N IV]
C IV-1	1548.19	1545.57	28.51 ± 0.03	17.00	C IV-1
C IV-2	1550.77	1548.28	8.92 ± 0.04	6.11	C IV-2
He II	1640.42	1639.46	1.53 ± 0.01	4.35	He II
O III]	1663.48	1663.21	1.94 ± 0.01	8.22	O III]/Al II
Al II	1670.79				
N IV	1718.55	1717.47	0.13 ± 0.01	5.20	N IV/Fe II
Fe II	UV 37				
N III]	1750.26	1748.94	0.81 ± 0.01	6.37	N III]
Fe II	UV 191	1787.41	0.30 ± 0.02	5.37	Fe II
[Ne III]	1814.73	1816.34	0.54 ± 0.02	8.86	Si II/Ne III
Si II	1816.98				
Al III	1857.4	1857.40	3.47 ± 0.08	11.01	Al III
Si III	1892.03	1893.24	0.55 ± 0.03	3.99	Si III/Fe IV
Fe III	UV 34				
C III]	1908.73	1903.61	20.51 ± 0.09	20.81	C III]-1

CHAPTER 5

DATA CATALOGS AND COMPOSITE SPECTRA ANALYSIS

There are two possible directions in which to study the Baldwin Effect with this sample of quasars. First, the line strengths and continuum luminosities can be found for each individual quasar. This requires excellent fits to the data. BOSS spectra have low signal-to-noise ratios, making line fits difficult. This means that any analysis of the Baldwin Effect or emission line equivalent widths will have high scatter. The Equivalent Width is, by definition, a measure of two quantities: The strength of the emission line and the luminosity of the continuum. Errors in each of these measurements are errors in the measurement of the Equivalent Width. To see the result of such work, see the work of Xu et al. (2008). That work measured the Baldwin Effect on a sample of 26,000 SDSS quasars from the fifth data release. The scatter in their data is large. The trend that work finds is well fit, however, due to the large number of data points.

The second option to examine the Baldwin Effect is to first create quasar composite spectra in "regions" binned on the parameter in question. For example, most theories on the Baldwin effect parameterize the strength of the effect (or the slope of the Baldwin Effect) as a function of the bolometric luminosity of the quasar in the quasar restframe. Thus, quasars can be binned by quasar bolometric luminosity with composite spectra assembled from quasars in each bin. Other theories of the Baldwin Effect, usually referred to as the "Modified Baldwin Effect", are parameterized on quantities such as the Black Hole mass or the Eddington Ratio. Again, the quasar sample can be binned on these quantities and quasar composite spectra can be made from the binned quasar spectra. This work uses the second method, as the first method has already been used on the BOSS quasar population by Xu et al. (2008). Here, we can bin on any observable quasar parameter.

5.1 Data

This work uses data from several sources. First, the spectra are taken from the BOSS program, as explained earlier. Second, fitted parameters are taken from the BOSS Data

Release 12 Quasar Catalog (DR12Q Pâris et al. 2014). Fitted parameters from DR12Q include the Full Width at Half Maximum of the Mg II and C IV lines, which are later used to calculate the mass of the central black hole of each quasar and the Principal Component Analysis (PCA) Redshifts of each quasar. For testing purposes, the quasar catalog from Shen et al. (2011) is also used, primarily to compare derived quantities (C IV FWHM, Black Hole Mass, Bolometric Luminosity, redshift, and Eddington Ratio) from this work to a published catalog. The composite created in Chapter 4 uses quasars in the redshift range $2.1 < z < 3.5$. To increase the quasar sample and the ranges in observed properties, the quasar sample used from this point on covers all redshifts.

5.2 Calculated Quantities

5.2.1 Black Hole Mass

This work uses the procedure for calculating the mass of a black hole within a quasar from Shen et al. (2011), given here:

$$log(M_{BH,vir}/M_{sun}) = a + blog(\lambda L_\lambda/10^{44} ergs^{-1}) + 2log(FWHM/kms^{-1}) \tag{5.1}$$

where a and b are constants empirically derived for different emission lines, $M_{BH,vir}$ is the virial black hole mass, M_{sun} is the mass of the sun, λL_λ is the bolometric luminosity of the quasar in the quasar rest frame, and FWHM is the Full Width at Half Maximum of the emission line being used to calculate the black hole mass. Hereafter, the mass of the black hole in units of the mass of the sun is abbreviated M_{BH} or "black hole mass" and the λL_λ is referred to as the "bolometric luminosity". The constants a and b are derived empirically from black hole reverberation mapping studies. Shen et al. (2011) notes the scatter in black hole mass from the reverberation-mapping scaling relations is approximately 0.4 dex. The emission line used for the term that includes the FWHM of a line depends on the redshift of the quasar. For quasars at a redshift $z > 1.9$ the CIV emission line is used. The constants a and b are found to be $a = 0.660$ and $b = 0.53$ according to Vestergaard & Peterson (2006).

5.2.2 Full Width Half Maximum

In this work, the FWHM of emission lines are taken from the DR12Q catalog. The continuum in DR12Q is calculated by creating principal components of the line region. Linear combinations of the principal components are made to fit the observed profile, and the FWHM is measured from the model. The DR12Q catalog calculates the continuum by fitting a power law over the region 1450 Å to 1500 Å, 1700 Å to 1850 Å, and 1950 Å to 2750 Å.

5.2.3 Bolometric Luminosity

The bolometric luminosity of the quasar is calculated in the manner following Xu et al. (2008), which in turn was from Richards et al. (2006). To find the bolometric luminosity, the continuum luminosity at $\lambda = 1350\mathring{A}$ is multiplied by an empirically derived constant. The constant used by Xu et al. (2008) and found by Richards et al. (2006) is four. Unfortunately, the 1350 Å region is not visible in every quasar, and as such a different region had to be found for quasars at $z < 1.9$, as this is the redshift at which the 1350 Å region moves to a much lower signal-to-noise region of the spectrum. The second region, used to calculate the bolometric luminosity for quasars at a redshift $z < 1.9$, is chosen to be at 2510 Å. To find the scaling constant for luminosity determined from the quasar continuum at 2510 Å is multiplied by four to find the bolometric luminosity, the median luminosity of quasars at 1350 Å is divided by the median luminosity of quasars at 2510 Å. These median luminosities are found using a quasar composite spectrum created from all quasars in the BOSS catalog that were observed at an airmass less than 1.2 and are not BALs or DLAs. This flux ratio is almost exactly 2.5. Thus, if the bolometric luminosity of a quasar is four times the luminosity at 1350 Å, and the median luminosity at 1350 Å is 2.5 times the median luminosity at 2510 Å, then the bolometric luminosity of the quasar must be approximately $4 * 2.5 = 10$ times the luminosity at 2510 Å. These simple relationships are the basis for calculating the bolometric luminosity of the quasar.

5.2.4 Eddington Luminosity and Eddington Ratio

The Eddington luminosity is the maximum rate that a black hole can accrete mass, in terms of the mass energy, as a function of black hole mass. The Eddington luminosity is $1.26x10^{31}(M_{BH}/M_{sun})$ Watts, or $1.26x10^{38}(M_{BH}/M_{sun})ergs^{-1}$. The Eddington ratio is simply

$$R_{edd} = L_{bol}/L_{edd}(M_{BH}) \tag{5.2}$$

or, in terms of logarithms,

$$Log(R_{edd}) = log(L_{bol}) - log(fracM_{BH}M_{\odot}) - 38.1 \tag{5.3}$$

as the log of $1.26x10^{38}$ is 38.1.

5.3 Comparing the Data Catalogs

Because this method uses both novel and simple methods for calculating certain quasar properties, it is necessary to compare these derived quasar properties to a pre-existing catalog. Shen & Ho (2014) has already calculated many of these parameters for use in

studies of black hole mass. Here, we compare the quantities and properties calculated in this work to the quantities and properties calculated in that work. This is possible because the Shen catalog examined SDSS quasars, some of which were reobserved in the BOSS program. Thus, there exists a subset of quasars which are both in the Shen catalog and usable for this work. Catalogs were matched by the names assigned by SDSS. Please note the following sections compare the Shen catalog and the DR12Q catalog. The DR12Q catalog is more recent and more refined, but both use high-quality data. These comparisons are to indicate possible sources of systematic error in the creation of subcatalogs.

5.3.1 Redshift

The first panel of Figure 5.1 compares the Shen catalog redshfits from the SDSS pipeline to the redshifts from the DR12Q catalog, specifically the PCA redshifts. This shows a very tight correlation between the two redshifts of the quasars. The second panel of Figure 5.1 shows the difference in SDSS redshifts and DR12Q redshifts plotted against the redshifts from SDSS. The median offset between these quantities is almost equal to zero, while the scatter $\sigma_z = 0.01$. This tiny scatter affects the calculated bolometric luminosity and a host of dependent parameters, but the tiny scatter indicated that systematic errors introduced here will be very small. There exists a slight discontinuity in the second panel at a redshift of $z = 2.2$. This arises due to the manner in which the Shen catalog found redshifts. The Shen catalog uses the Mg II line to find redshift, which disappears from SDSS spectra at a redshift of approximately $z = 2.2$. Above this redshift, spectra are matched to a quasar composite spectrum using quasars at a redshfit $z < 2.2$.

5.3.2 Bolometric Luminosity

The comparison between bolometric luminosities is shown in the first panel of Figure 5.2. The units here are the logarithm of the bolometric luminosity in $ergs^{-1}$. The correlation between the two quantities is fairly strong. The second panel of Figure 5.2 shows the difference in the Shen catalog bolometric luminosity and the bolometric luminosity calculated here versus the bolometric luminosity calculated in the Shen catalog. At luminosities higher than Log(Lbol)= 46.2, there is very little trend with bolometric luminosity. Below Log(Lbol)= 46.2, bolometric luminosities calculated in this work are preferentially larger than the bolometric luminosities calculated in the Shen catalog. The scatter between these catalogs in bolometric luminosity is 0.13 dex and the median difference between the catalogs is -0.02 dex. This may be due to quasar continuum variability over the 5-10 years between the SDSS photometric observation and the SBOSS spectroscopic observation. A systematic

error of 0.13 dex is equivalent to a 35% error. However, the systematic offset is only 5%, and should have minimal adverse consequences on this work.

5.3.3 Full Width Half Maximum

The FWHM of lines are calculated slightly differently in Shen & Ho (2014) and Pâris et al. (2014). In the Shen catalog, the FWHM is calculated by fitting multiple Gaussians to the line profiles. Each line is handled differently. As this project uses several of these methods later, it is instructive to explore these methods here.

5.3.3.1 Method for Calculating FWHM

For C IV, the Shen catalog ignores iron emission, as it is generally weak. That work did find that ignoring iron emission does not significantly change the FWHM of the C IV line, though it does reduce the equivalent width of C IV by approximately 0.05 dex, a minor factor in these calculations. They also use a power law fit to find the continuum, which is subtracted from the line emission. The windows for this fit are 1445 Å to 1465 Å and 1700 Å to 1705 Å. The window for the line emission is 1500 Å to 1600 Å. The C IV line is fitted with 3 Gaussians and the FWHM is determined from the model generated.

For $H\alpha$, the Shen catalog calculates the FWHM by fitting the $H\alpha$ line with the optical iron line template from Boroson & Green (1992). The continuum window, from 6000 Å to 6250 Å and 6800 Å to 7000 Å, is fit with a power law which is subtracted from the flux. The iron lines are also fit in this region. The line fitting region is from 6400 Å to 6800 Å. Within this region, the narrow line components of $H\alpha$, [N II] (6548 Å), [N II] (6584 Å), [S II] (6717 Å), and [S II] (6731 Å) are fit with a single Gaussian each. For each, the velocity offsets and redshifts are set to be equal. The relative flux ratio between [N II] (6548 Å) and [N II] (6584 Å) is set to be equal to 2.96. The FWHM of these lines is set to be no greater than 1200 km s^{-1}. The broad component of $H\alpha$ is modeled by a single Gaussian with a FWHM greater than 1200 km s^{-1}.

For $H\beta$, the Shen catalog again uses the Boroson & Green (1992) optical iron line templates. Their fitting window for the continuum and iron lines is 4435 Å to 4700 Å and 5100 Å to 5535 Å. The narrow lines around $H\beta$ are fit similarly to the narrow lines around $H\alpha$. [O III] (4959 Å) and [O III] (5007 Å) are constrained to have the same redshift, but are modeled with two Gaussians. The broad component is fit with one Gaussian over the range 4700 Å to 5100 Å, and the FWHM is derived from that.

Finally, for Mg II, the iron line and continuum fitting region is 2200 Å to 2700 Å and 2900 Å to 3090 Å. The Mg II line is fit over 2700 Å to 2900 Å with up to four Gaussians.

The FWHM is determined from the Gaussians with a FWHM greater than 1200 km s^{-1}.

5.3.3.2 Comparison of FWHM

Figure 5.3 shows the relationship between the FWHM of the lines used for black hole mass estimation. As almost all quasars which were matched between the Shen catalog and the DR12Q catalog are above a redshift of $z = 1.9$, only a tiny fraction of the data points seen in this figure are for the Mg II FWHM. Almost all the points shown represent the FWHM of the C IV emission line. This first panel shows an interesting trend. For most of the points, the FWHMs in both catalogs are similar, although with a trend such that quasars at a high C IV FWHM have a higher C IV FWHM in the Shen catalog than in the DR12Q catalog. However, the DR12Q catalog shows hardly any quasars with a C IV FWHM greater than 8,000 km/s, while the Shen catalog shows a significant number of quasars with a C IV FWHM greater than 8,000 km/s. Similarly, the DR12Q catalog shows hardly any quasars with a C IV FWHM less than 2,000 km/s, while the Shen catalog shows a significant number of quasars with a C IV FWHM less than 2,000 km/s.

Generally speaking, two possibilities arise to explain this discrepancy. Either the "true" C IV FWHM is better modeled by the DR12Q FWHMs, with the Shen catalog FWHMs having some systematic offset from the "true" value, or the C IV FWHM is better modeled by the Shen catalog FWHMs, with the DR12Q FWHMs having some systematic offset from the "true" value. In the first case, one could think of the Shen catalog FWHMs usually being close to the true value (which DR12Q does a fair approximation of), but some fraction of the time, the reported value is randomized between 0 and 15,000 km/s. In the second case, if the Shen catalog FWHMs are more correct, then the DR12Q FWHMs could be the true (approximately Shen catalog) value modified by some value such that the reported value is randomized between 2,000 and 8,000 km/s. This by itself is an interesting result. These results are symmetrical.

The two results can be further examined by plotting the difference between the catalog's FWHMs by the FWHMs in a particular catalog. The first panel of Figure 5.4 shows the FWHM of quasars in the Shen catalog minus the FWHM of quasars in the DR12Q catalog versus the FWHM of quasars in the Shen catalog. Here, there is a significant trend with FWHM. At low FWHM, Shen catalog FWHMs are universally lower than their DR12Q counterparts. At high Shen catalog FWHM, the Shen catalog FWHMs are universally higher than their DR12Q counterparts. At moderate values of FWHM, the two catalogs are more likely to agree. The assumption DR12Q FWHMs are biased indicates a very

preferential bias, only making significant modifications outside a specific range of FWHMs, and always to higher values. The second panel of Figure 5.4 shows the FWHM of quasars in the Shen catalog minus the FWHM of quasars in the DR12Q catalog versus the FWHM of quasars in the DR12Q catalog. In this case, there is very little trend with FWHM. While the scatter is significant, There is no trend in the scatter with DR12Q FWHM. If the DR12Q FWHMs are more consistent with the "real" value and the Shen catalog FWHMs are the real value plus or minus some random value in some cases, then this figure would show that the random value is not a function of the "real" value. Based on this, the idea that Shen catalog FWHMs are a product of adding or subtracting a random value to or from the "real" value is more credible than the alternative. The scatter in the FWHMs between the two catalogs is 1,220 km/s, while the median offset is 340 km/s. The scatter affects the measured black hole mass, discussed in the next section.

5.3.4 Black Hole Mass

Because the black hole mass is a quantity derived from the FWHM of an emission line, and the relationship between the FWHM of the C IV line in the DR12Q catalog and the FWHM of the C IV line in the Shen catalog is not straightforward, it stands to reason that the relationship between the black hole masses in the Shen catalog and the black hole masses in the DR12Q catalog would also not be straightforward. This can be seen in Figure 5.5. Black hole masses are plotted as the logarithm of the black hole mass in solar masses. The first panel of Figure 5.5 shows the trend of black hole mass calculated here against the black hole mass calculated in the Shen catalog. The trend is slight, but the range in black hole mass in this work seems to be tighter than the range in the Shen catalog, and the slope appears to be slightly shallower than one. The second panel of Figure 5.5 plots the trend of the difference in black hole mass (Shen catalog black hole mass minus black hole mass in this work) versus the black hole mass in this work. There is very little trend with the black hole mass in this work. The median difference between Shen catalog black hole masses and black hole masses in this work is 0.04 dex, while the scatter is 0.22 dex. This compares favorably to the scatter in calculated black hole masses due to various uncertainties, at 0.4 dex.

5.3.5 Eddington Ratio

Finally, Figure 5.6 shows the relationship between the Eddington ratios in the Shen catalog and the Eddington ratios in this work. Again, this is a derived quantity, taking in the quasar bolometric luminosity and the black hole mass, which in turn is a function

of the FWHM of an emission line (usually C IV). There appears to be little trend with Eddington Ratio that cannot be explained by the difference in FWHM discussed above. The second panel of Figure 5.6 shows the trend as the difference in Eddington Ratio versus the Eddington Ratio as calculated in this work. This also shows no trend with Eddington Ratio. The median difference is -0.06 dex and the scatter is 0.20 dex.

5.4 Comparing Quantities

This section explores the relationships between quantities. One goal of this work is to determine upon which quantity or quantities the Baldwin Effect is parameterized. To do so, the relationships between parameters must be understood.

The relationship between i-band absolute magnitude and bolometric luminosity, shown in Figure 5.7, is obvious, and the correlation is sound.

The relationship between absolute i-band magnitude and redshift, shown in Figure 5.8, is a function of target selection, as described in Chapter 3. As black hole mass increases, the luminosity increases, as shown in Figure 5.9. There is little correlation between eddington ratio and absolute i-band magnitude as shown in Figure 5.10. The trend between redshift and bolometric luminosity, shown in Figure 5.11, is set by target selection. The black hole mass and bolometric luminosity are strongly correlated, as shown in Figure 5.12.

The trend between redshift and black hole mass, shown in Figure 5.13, is also set through target selection, as black hole mass is related to luminosity. There is a slight trend between redshift and Eddington ratio, shown in Figure 5.14, again related to target selection.

There is a slight downward trend in Eddington ratio as black hole mass increases, as shown in Figure 5.15, likely due to the fact that low mass black holes need to have a high accretion rate to be bright enough to detect. As the Eddington ratio increases, the bolometric luminosity also increases, as shown in Figure 5.16.

There is no trend associated with spectral index, as shown in Figures 5.17, 5.18, 5.19, 5.20, and 5.21.

5.5 Composite Spectra Analysis

5.5.1 Composite Spectra and Errors

Composite spectra are generated in a slightly different way than as described in Chapter 4. Hereafter, spectra are ordered by increasing quantity of the observable in question. Thus, when studying the Baldwin Effect in bolometric luminosity, the quasar spectra are ordered by increasing bolometric luminosity. BALs, DLAs, and objects not observed under

the XDQSO or BONUS targeting schemes are rejected. Galactic extinction is corrected for as in earlier methods. The airmass-dependent correction found earlier is applied.

A composite of the first 2000 spectra is then created. In the previous method, spectra are ordered by redshift and taken at 500 at a time to normalize. This is not ideal in this situation, as there will only be four normalizations for 2000 spectra. Instead, quasar spectra are matched to a master spectrum. The master spectrum is a quasar composite spectrum created from the full sample of all quasars that are not BALs or DLAs, and are not observed at an airmass greater than 1.2. This is 138,335 quasar spectra. This quasar composite spectrum is created in the same way as the previous composite of 102,150 spectra in Chapter 4. This quasar composite spectrum is referred to as the master quasar composite spectrum. Individual quasar composite spectra used in testing the Baldwin Effect are thus created by matching their individual component spectra to the master quasar composite spectrum (by matching the clipped, weighted medians of the two) and averaged by taking the weighted, clipped median. This is repeated in bins of 2000 spectra in order of increasing quantity of interest.

Using this method to create sample quasar composite spectra raises a potential concern. Does creating the quasar composite spectra in this way "pollute" the sample quasar composite spectra, confusing the Baldwin Effect in some way? This seems unlikely, as the only major effect caused by this change should be that the the spectral index of the sample quasar composite spectrum will not precisely match the median spectral index of the quasars used to create the particular sample quasar composite spectrum. Another minor issue is that the relative line strengths will be different here than in the master quasar composite spectrum, and thus a slightly incorrect scaling factor will be applied to the spectra used in creating the sample quasar composite spectrum. This effect should be very small, as the scaling factor is applied to line and continuum regions equally, and the Equivalent Width is a fractional quantity.

Errors to the quasar composite spectrum are calculated through a bootstrap resampling method. The quasar population in each bin is randomly resampled N times, where N is the number of quasars in the original sample. This resampling involves randomly choosing N spectra from the initial sample, with the possibility of repeats if the same spectrum is chosen multiple times. This newly created sample, a subset of the previous sample, is used to create a new composite. This is repeated 50 times. At each wavelength, the standard deviation in flux between all these quasar composite spectra is measured and recorded as the error at that wavelength.

This sample of quasars and the ability to create quasar composite spectra from subsamples of the quasar sample (following Harris et al 2015) allows for an examination of the Baldwin Effect with unprecedented signal to noise. To examine the Baldwin Effect one must first create quasar redshift/i-band-absolute-magnitude-binned quasar composite spectra. Binning in i-band absolute magnitude is necessary, as the Baldwin Effect's independent variable is the absolute magnitude of the quasar, and the data available for absolute magnitude are in the i-band, from DR12Q (Pâris et al. 2014). DR12Q calculates the i-band absolute magnitude at $z = 2$ and corrects for galactic extinction and also assumes a power law continuum of -0.5 in terms of frequency. DR12Q also uses the K-corrections from Richards et al. (2006).

5.5.2 Measuring Equivalent Width

With these quasar composite spectra created, individual moderate- to high-signal-to-noise quasar emission lines can be identified, with those lines to be examined for the Baldwin Effect. Seven lines or line complexes are identified: The C II line, the C III], Si III], and Al III complex, the Mg II line, the C IV line, the O I and Si II complex, the Si IV and O IV] complex, and the He II line. Continuum and emission regions are chosen for each line. The continuum and emission line regions for C IV and Mg II are taken from Shen et al. (2011). All other continuum and emission line regions are found via visual inspection of the quasar composite spectrum. Continuum and emission line regions are shown graphically in Figure 5.22, Figure 5.23, Figure 5.24, Figure 5.25, Figure 5.26, Figure 5.27, and Figure 5.28. For each line in each composite, a power law is fit to the continuum region. The equivalent width is found by taking the flux at each wavelength minus the fitted power law continuum at that wavelength, all divided by the fitted power law continuum at that wavelength. This gives the proportional flux compared to the continuum at each pixel. These values are multiplied by the width of the pixel in units of angstroms. This then gives the effective equivalent width of the emission line at each wavelength interval. These effective equivalent widths are summed to find the total equivalent width of the line. This is done for each emission line in every composite.

The error on the equivalent width is calculated, making use of the aforementioned quasar composite spectrum error. The method is, in effect, a reverse of the bootstrap resampling method. At each pixel of the quasar composite spectrum, the error at that pixel is read in from the bootstrap resampling error. A random number chosen through a Gaussian random number generator with a standard deviation equal to the standard deviation reported in the error array for that wavelength is added to the flux of the quasar composite spectrum at

that corresponding wavelength. This is done across the spectrum and the equivalent width is found using the same method as above. This is then done 50 times and the standard deviation of the reported equivalent widths is calculated. This standard deviation of the equivalent widths is reported as the error in the equivalent width.

5.6 Preservation of Spectral Properties in Composite Spectra

Bachev et al. (2004) found that composite quasar spectra preserve the median spectral properties of the quasar sample. Specifically, that work determined through visual inspection that bins of more than 100 quasars preserved line shape. In addition, that work generated and coadded sample line profiles and showed that the type of line profile was preserved in the composite. Denney et al. (2016) shows that this is generally true, with exceptions for low-SNR spectra, which introduce biases into composite spectra line profiles.

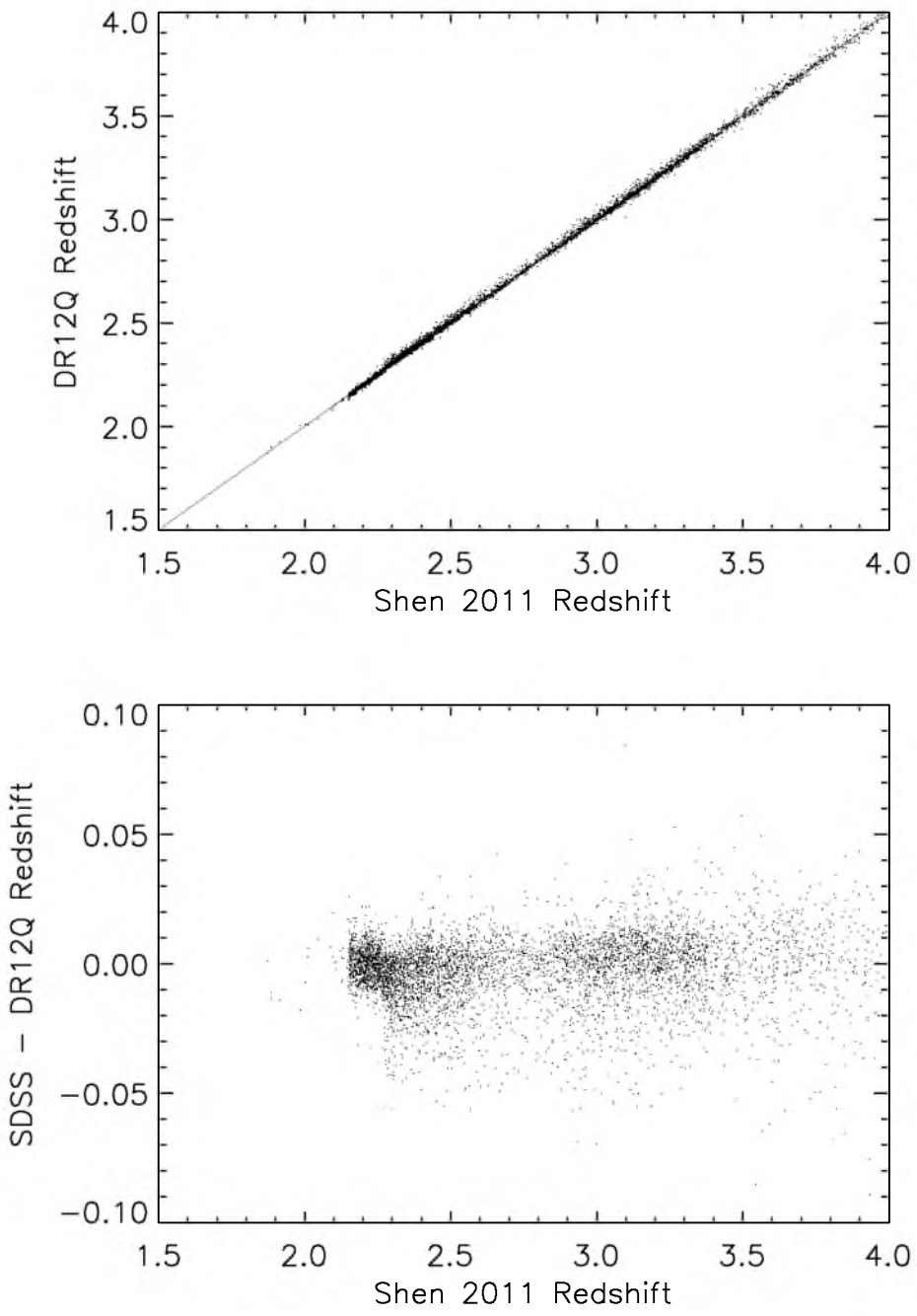

Figure 5.1: Comparison between the redshifts documented in DR12Q and the Shen catalog. Top Panel: The DR12Q redshift versus the Shen catalog redshift, with a line at $1 = 1$ to guide the eye. Bottom Panel: Shen catalog redshift minus DR12Q redshift versus Shen catalog redshift. This shows general agreement, with little redshift dependence.

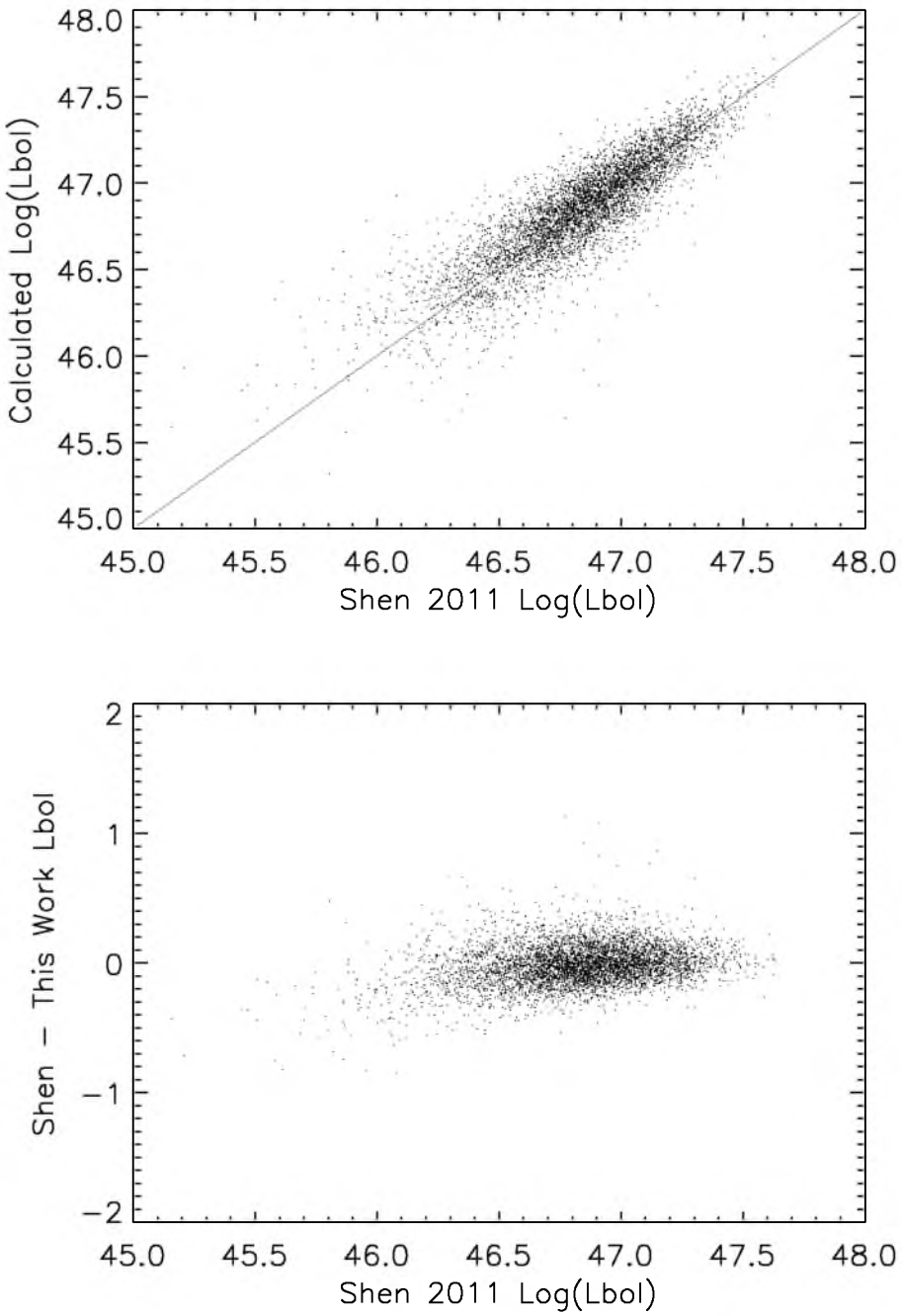

Figure 5.2: Comparison between the bolometric luminosities calculated here and calculated for the Shen catalog. Top Panel: Bolometric luminosities calculated here versus the Shen catalog bolometric luminosities, with a line at 1 = 1 to guide the eye. Bottom Panel: Shen catalog bolometric luminosities minus the bolometric luminosities calculated here versus Shen catalog bolometric luminosities. This shows general agreement, with little dependence upon bolometric luminosity except at low bolometric luminosity, less than $10^{46} ergs^{-1}$.

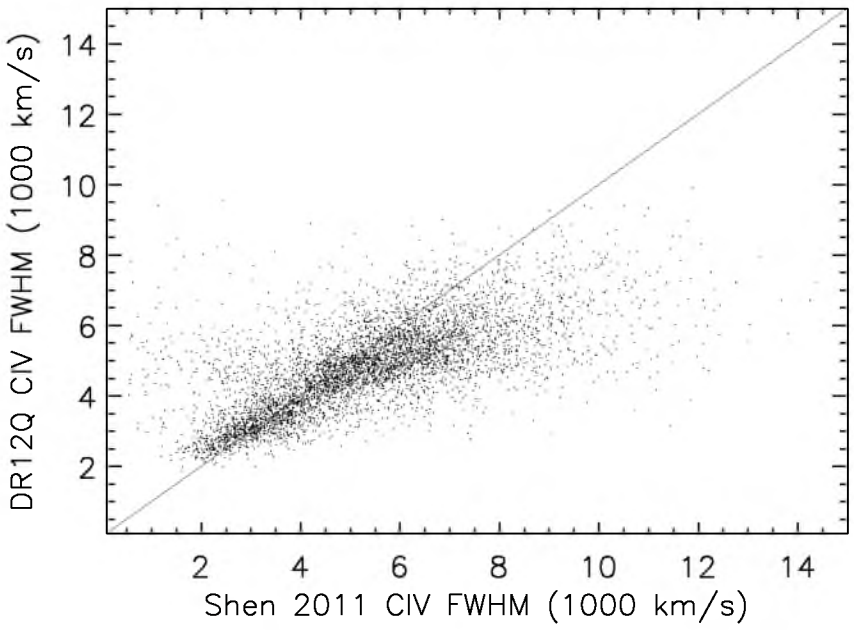

Figure 5.3: Comparison between the full width at half maximum of the C IV line in the DR12Q catalog and the Shen catalog. The structure here is peculiar.

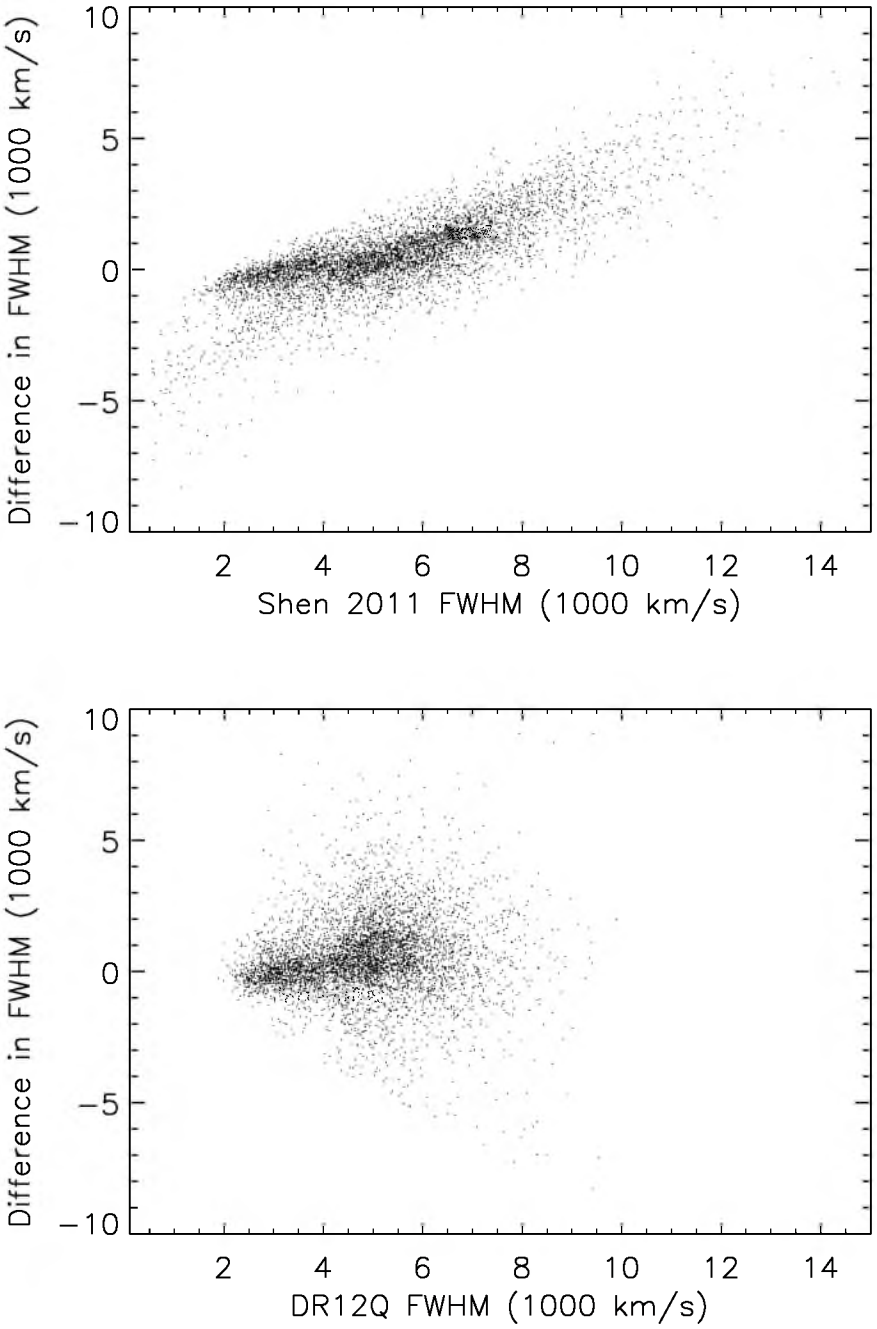

Figure 5.4: Comparison between the full width at half maximum documented in DR12Q and in the Shen catalog. Top Panel: Full width at half maximum documented in DR12Q minus the full width at half maximum in the Shen catalog versus the full width at half maximum in the Shen catalog, both for C IV. Bottom Panel: Full width at half maximum documented in DR12Q minus the full width at half maximum in the Shen catalog versus the full width at half maximum in the DR12Q catalog, both for C IV.

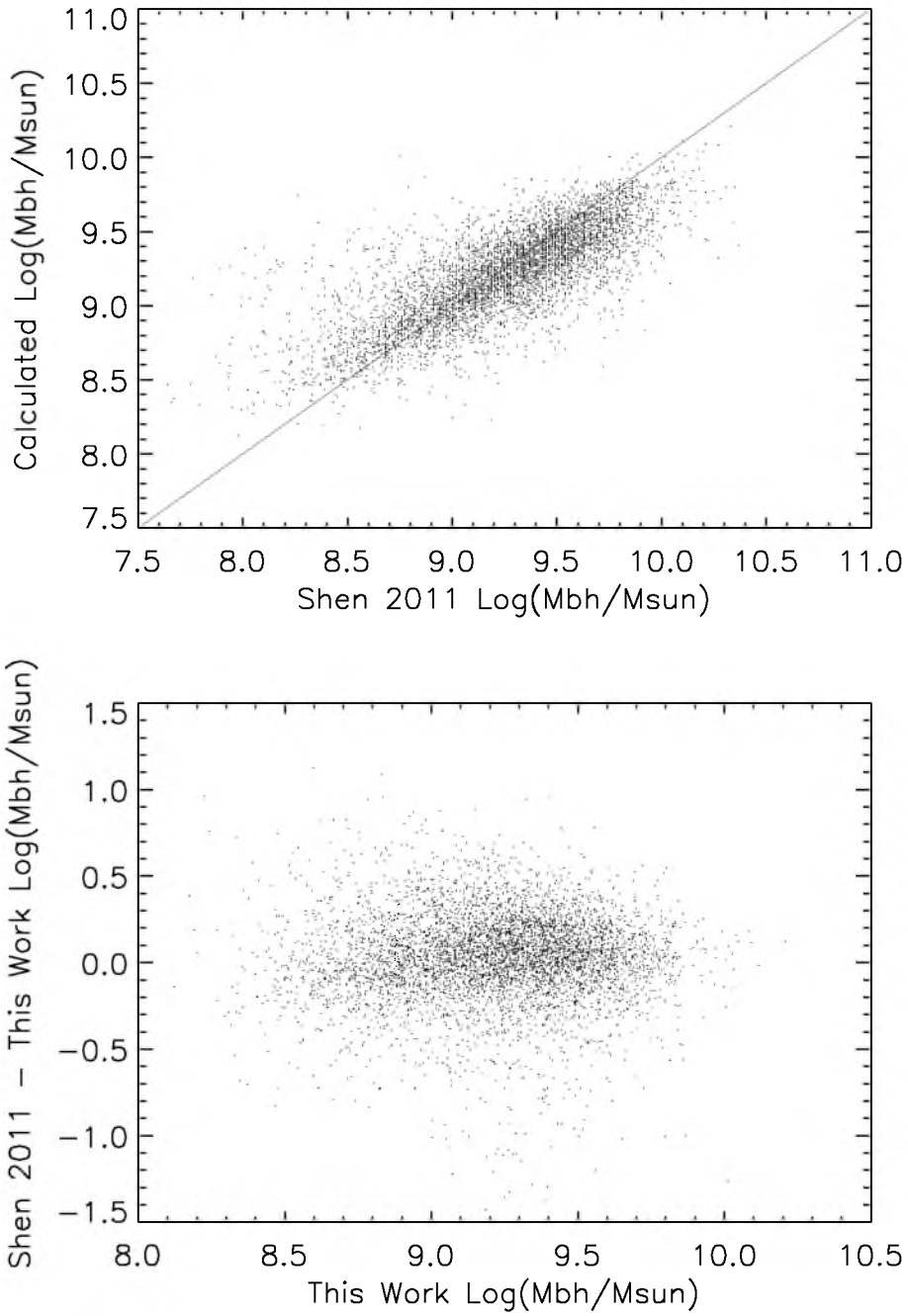

Figure 5.5: Comparison between the black hole masses calculated here and calculated for the Shen catalog. Top Panel: Black hole masses calculated here versus the Shen catalog black hole masses, with a line of unity slope to guide the eye. Bottom Panel: Shen catalog black hole masses minus the black hole masses calculated here versus Shen catalog black hole masses. The discrepancies are due primarily to the difference in full width at half maximum detailed above.

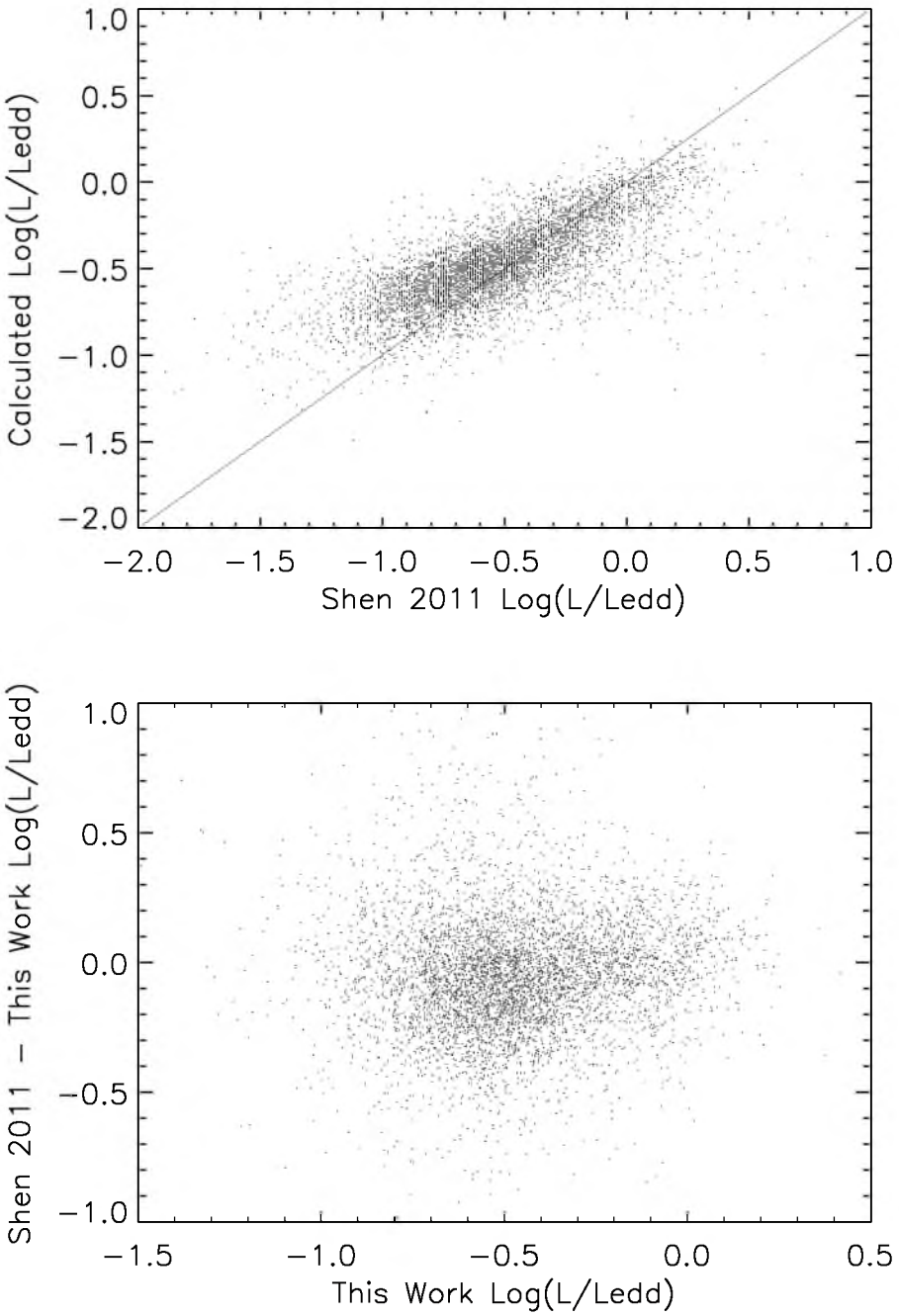

Figure 5.6: Comparison between the Eddington ratios calculated here and calculated for the Shen catalog. Top Panel: Eddington ratios calculated here versus the Shen catalog Eddington ratios, with a line at $1 = 1$ to guide the eye. Bottom Panel: Shen catalog Eddington ratios minus the Eddington ratios calculated here versus Shen catalog Eddington ratios. The discrepancies are due primarily to the difference in full width at half maximum detailed above.

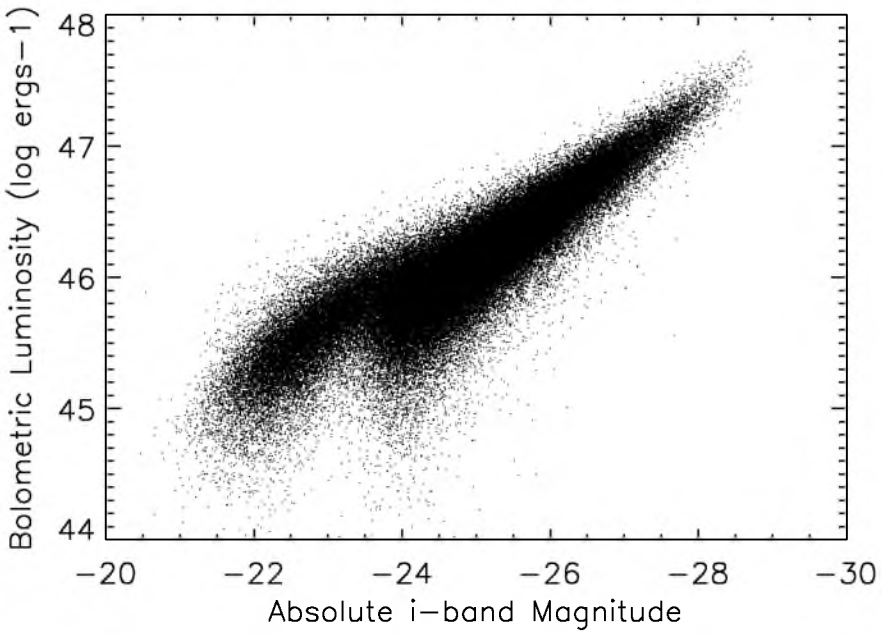

Figure 5.7: Comparing the absolute i-band luminosity to the calculated bolometric luminosity.

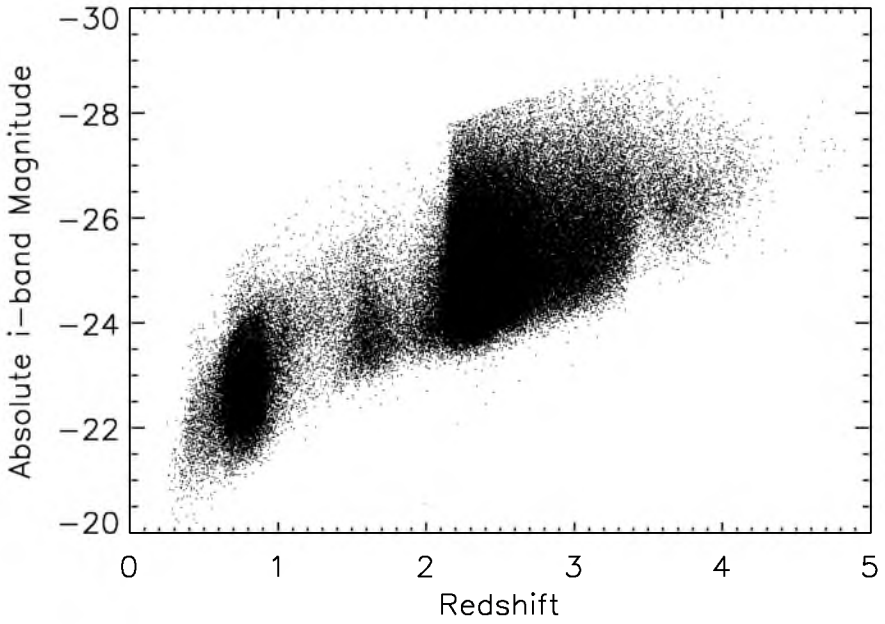

Figure 5.8: Comparing the absolute i-band luminosity to the redshift. The absolute i-band luminosity is measured in magnitudes.

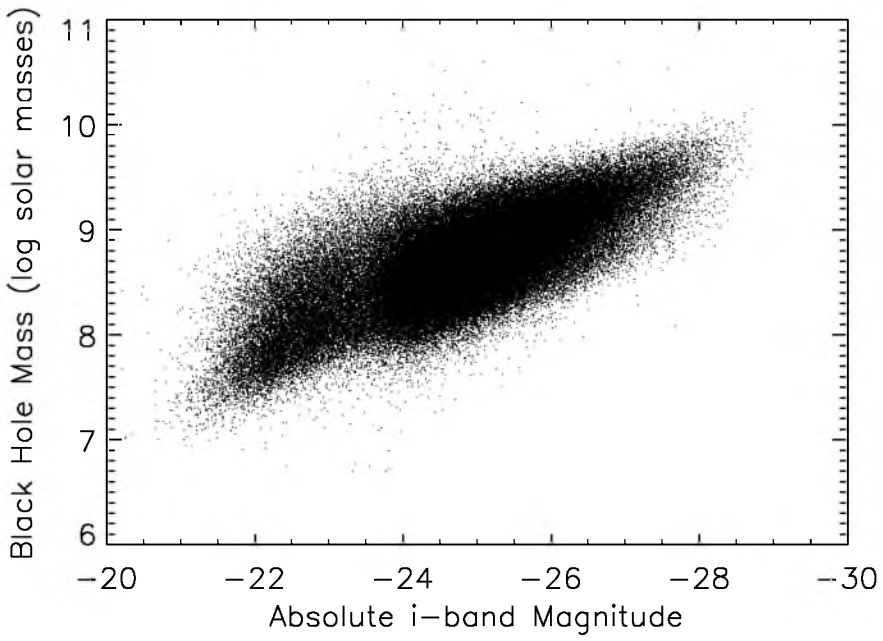

Figure 5.9: Comparing the absolute i-band luminosity to the black hole mass. The black hole mass is in units of solar mass.

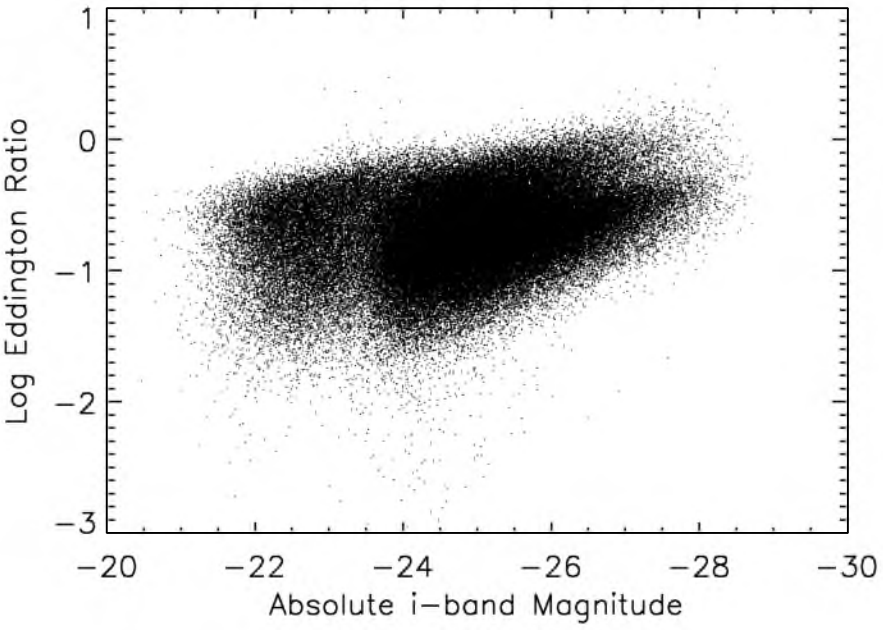

Figure 5.10: Comparing the absolute i-band luminosity to the Eddington ratio. The Eddington ratio is unitless.

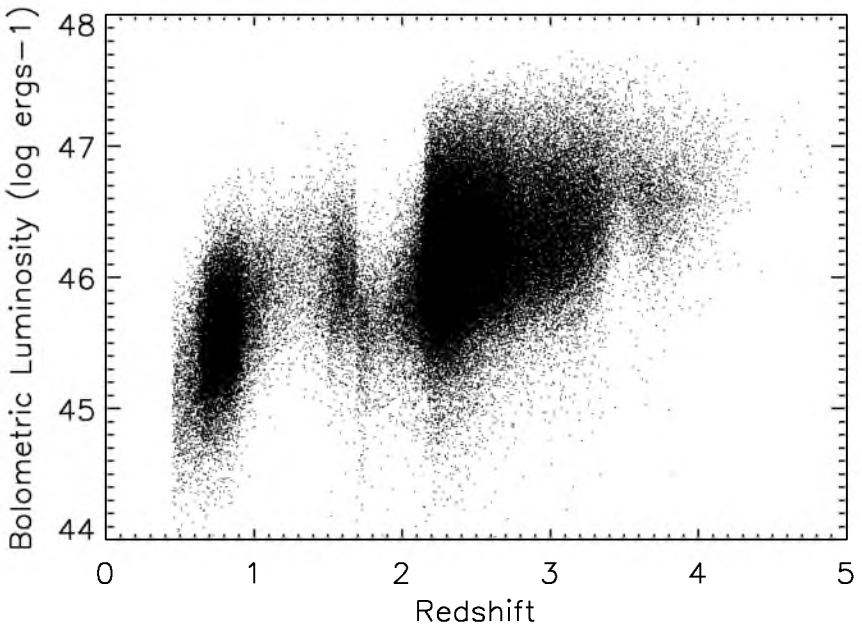

Figure 5.11: Comparing the redshift and bolometric luminosity. The bolometric luminosity is in units of solar luminosity.

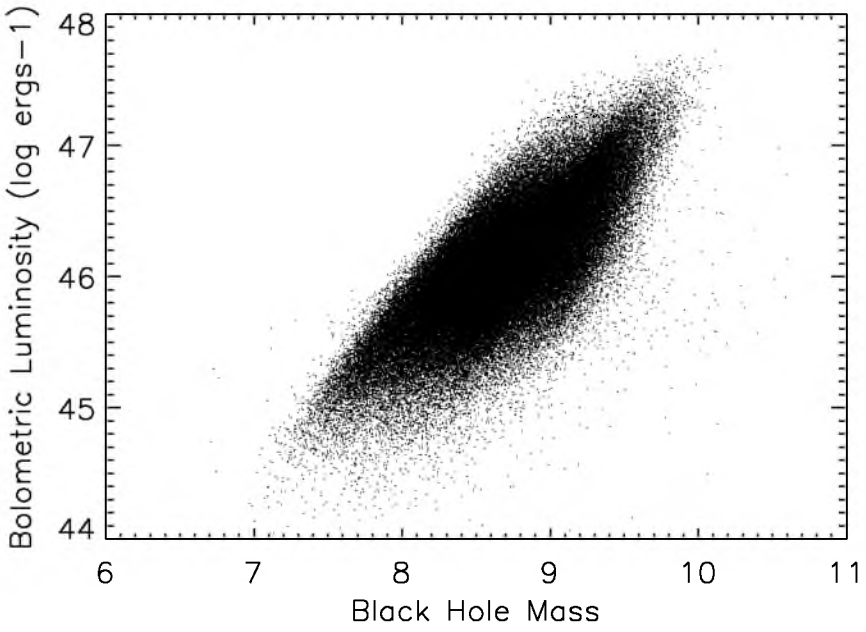

Figure 5.12: Comparing the black hole mass and bolometric luminosity. The bolometric luminosity is in units of solar luminosity.

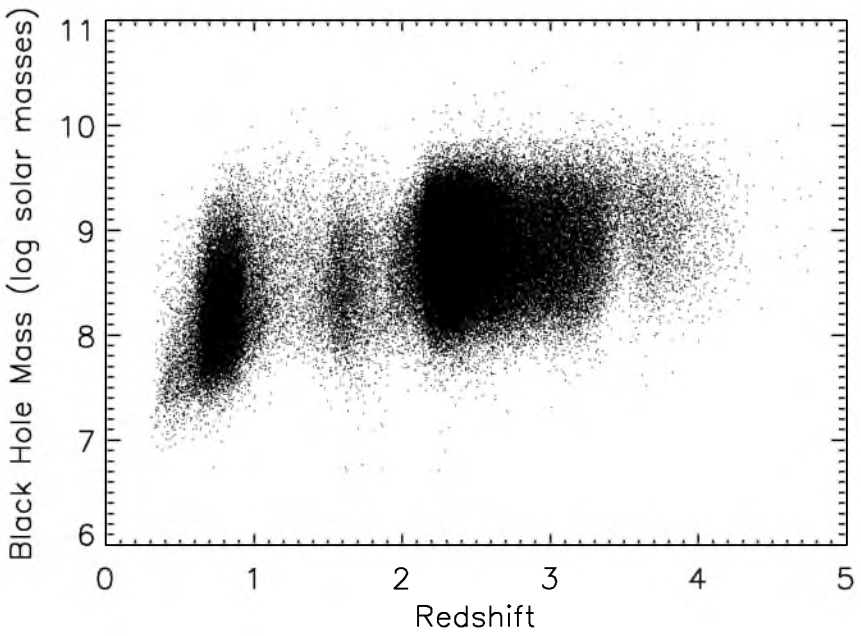

Figure 5.13: Comparing the redshift and black hole mass. The black hole mass is in units of solar mass.

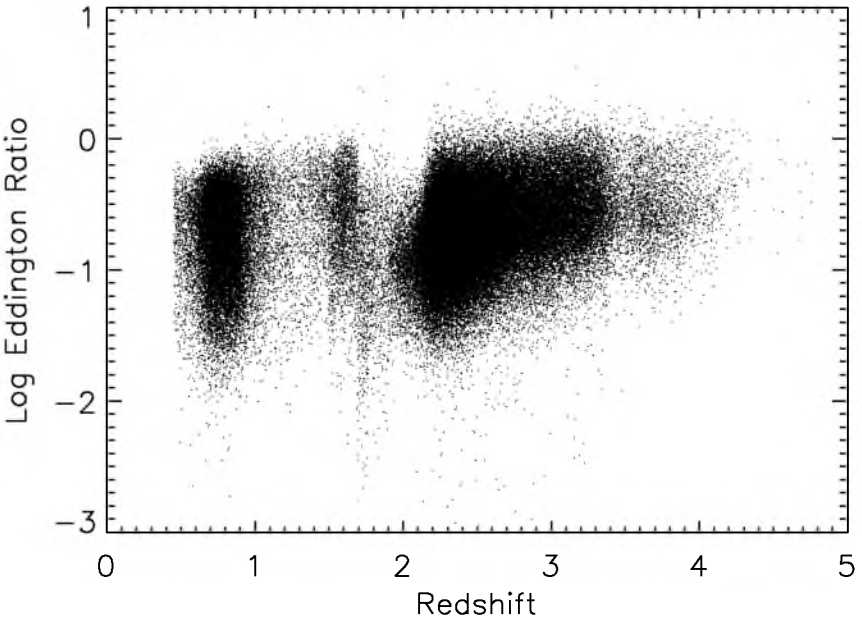

Figure 5.14: Comparing the redshift and Eddington ratio. The Eddington ratio is unitless.

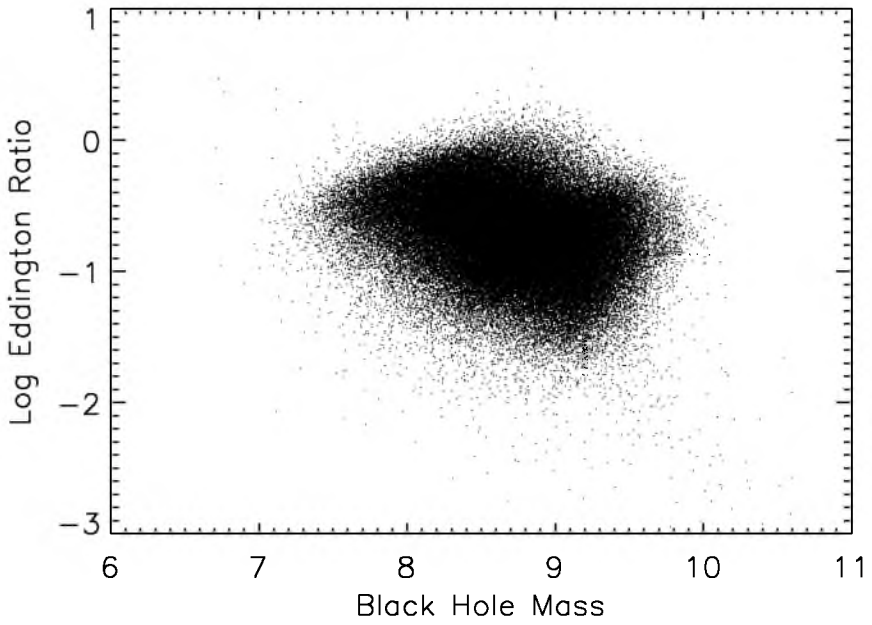

Figure 5.15: Comparing the black hole mass and Eddington ratio. The Eddington ratio is unitless.

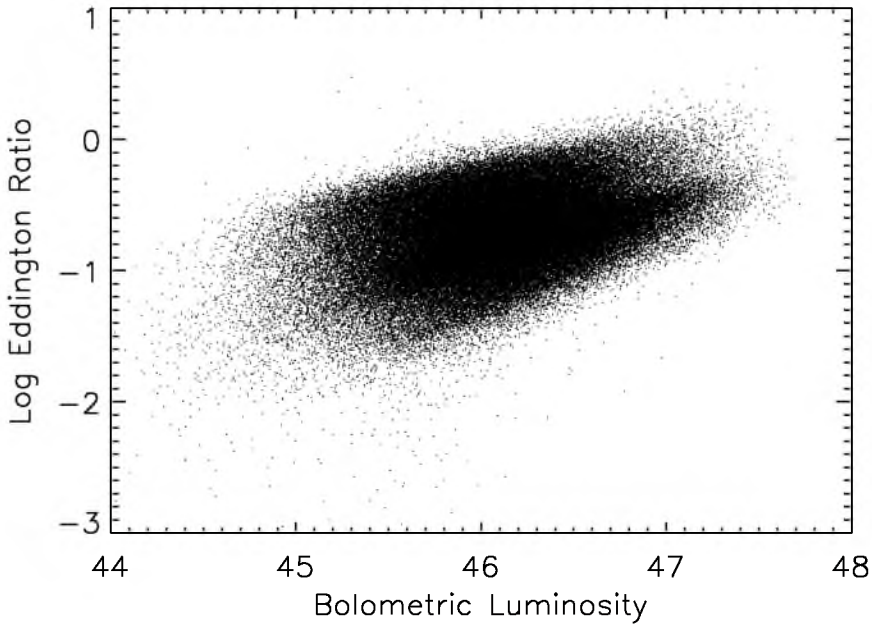

Figure 5.16: Comparing the bolometric luminosity and Eddington ratio. The Eddington ratio is unitless.

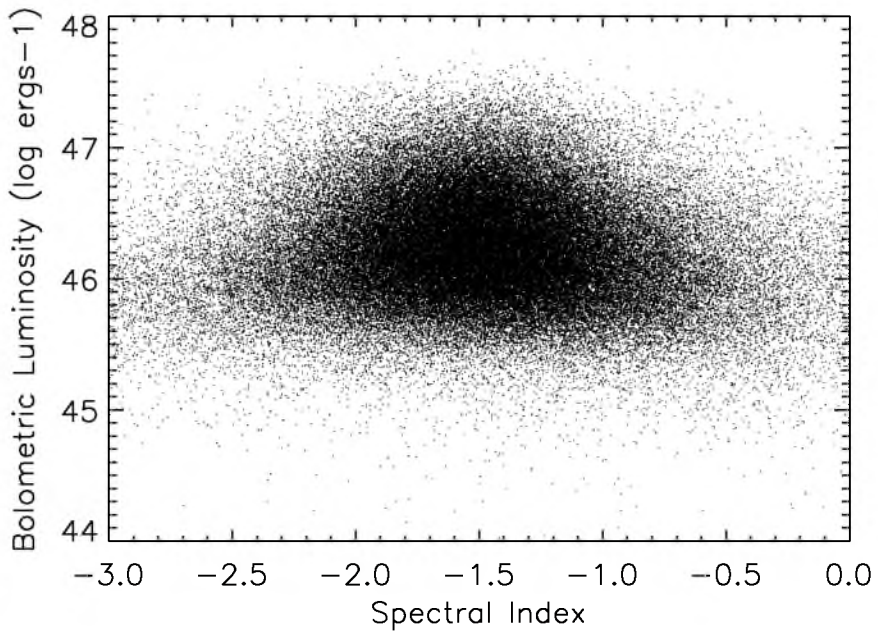

Figure 5.17: Comparing the spectral index to the calculated bolometric luminosity. The bolometric luminosity is in units of solar luminosity.

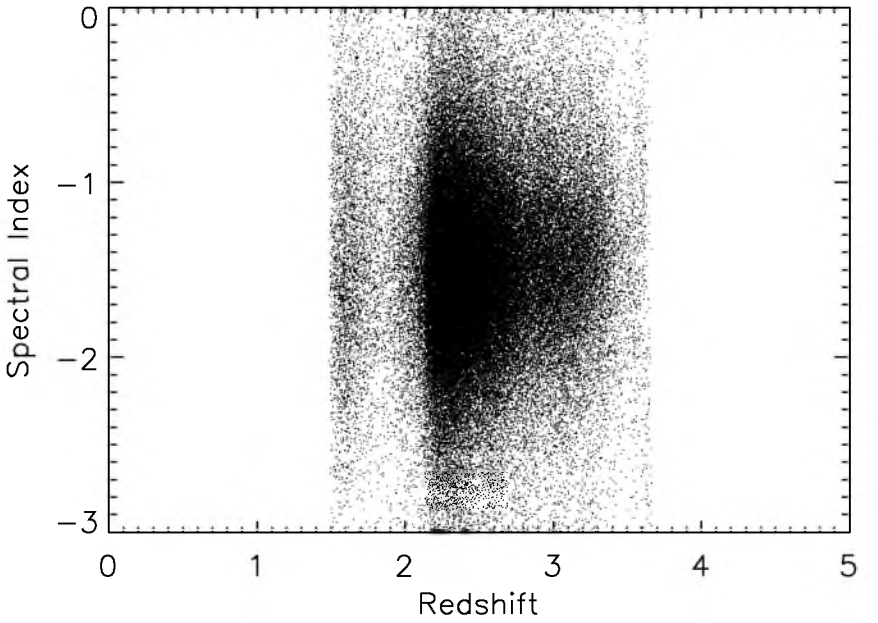

Figure 5.18: Comparing the spectral index to the redshift. The spectral index is unitless.

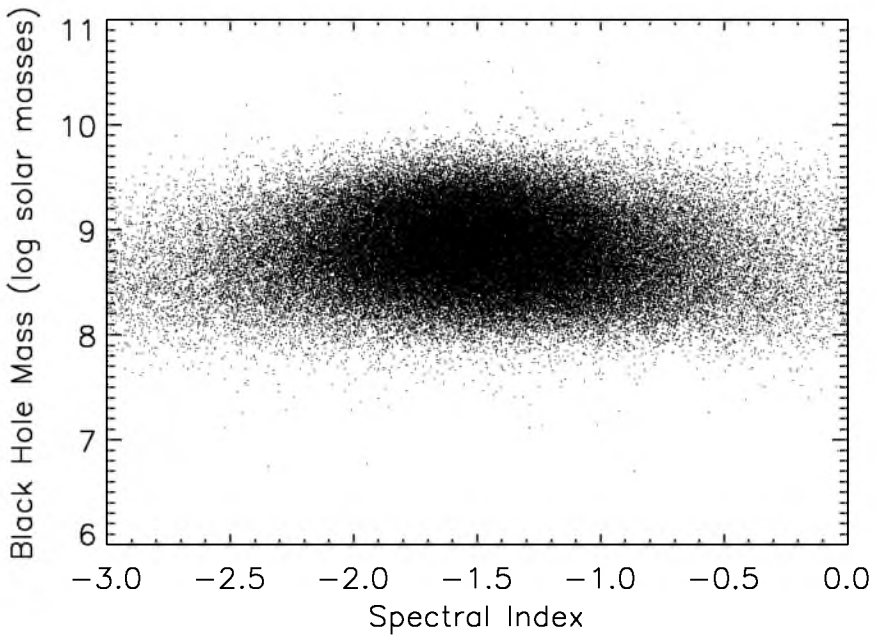

Figure 5.19: Comparing the spectral index to the black hole mass. The black hole mass is in units of solar mass.

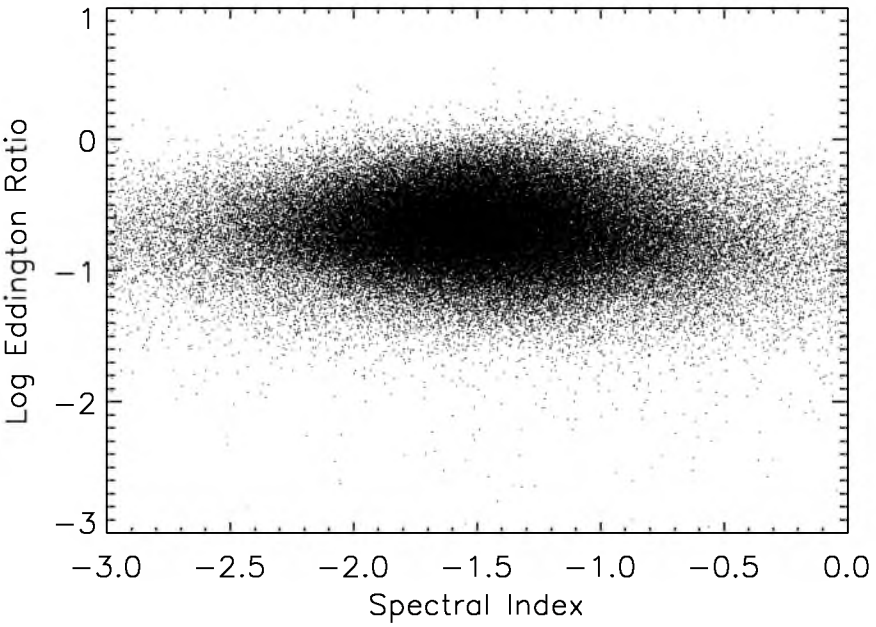

Figure 5.20: Comparing the spectral index to the Eddington ratio. The Eddington ratio is unitless.

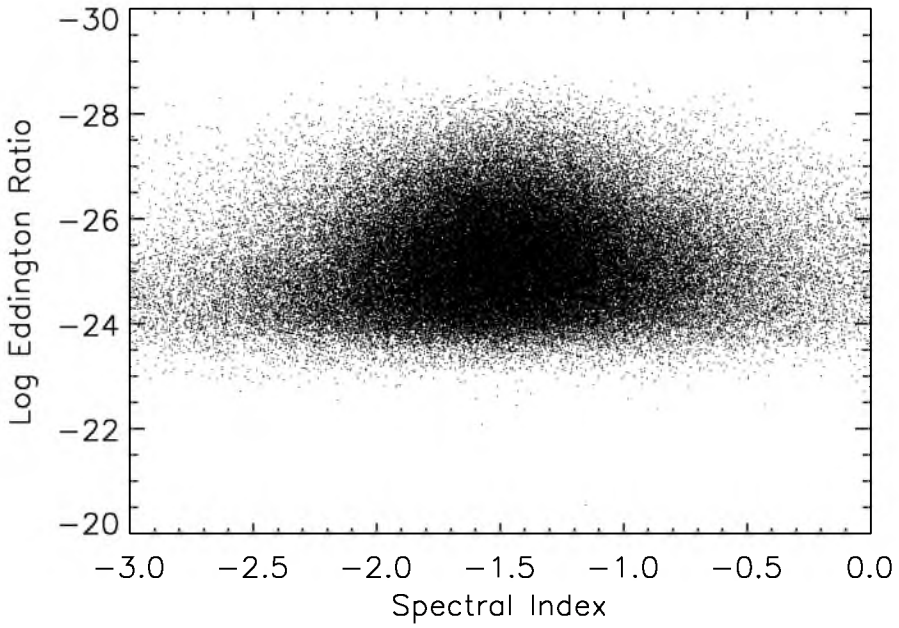

Figure 5.21: Comparing the spectral index to the absolute i-band luminosity. The absolute i-band luminosity is measured in magnitudes.

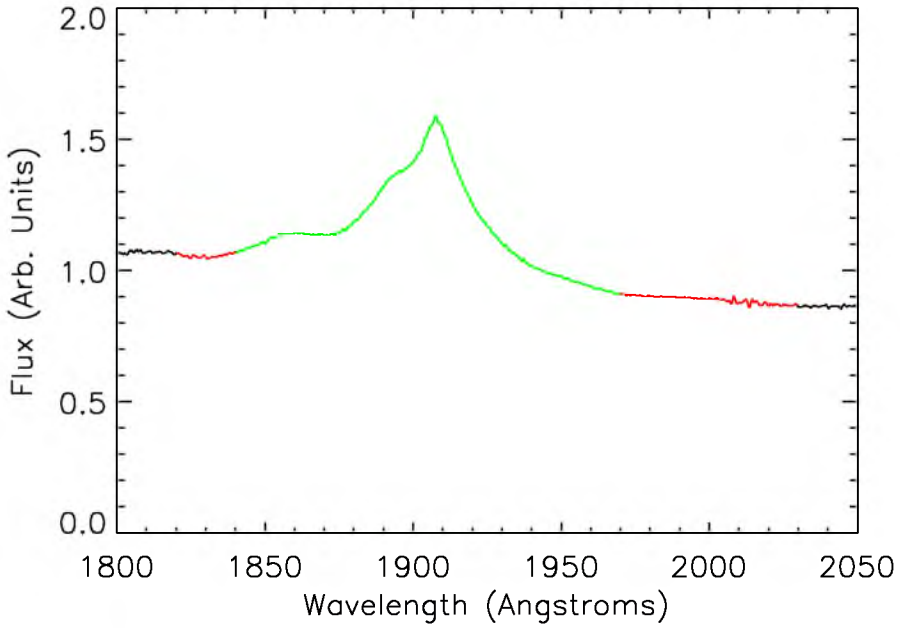

Figure 5.22: The continuum and line fitting regions for the C III, Si III, and Al III lines. The continuum fitting region is shown in red. The line fitting region is shown in green.

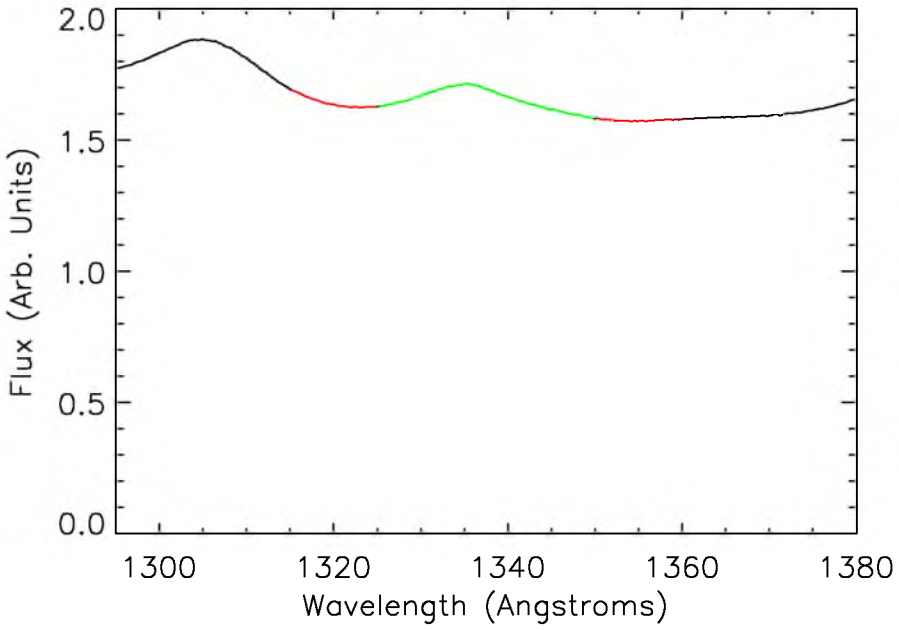

Figure 5.23: The continuum and line fitting regions for the C II line. The continuum fitting region is shown in red. The line fitting region is shown in green.

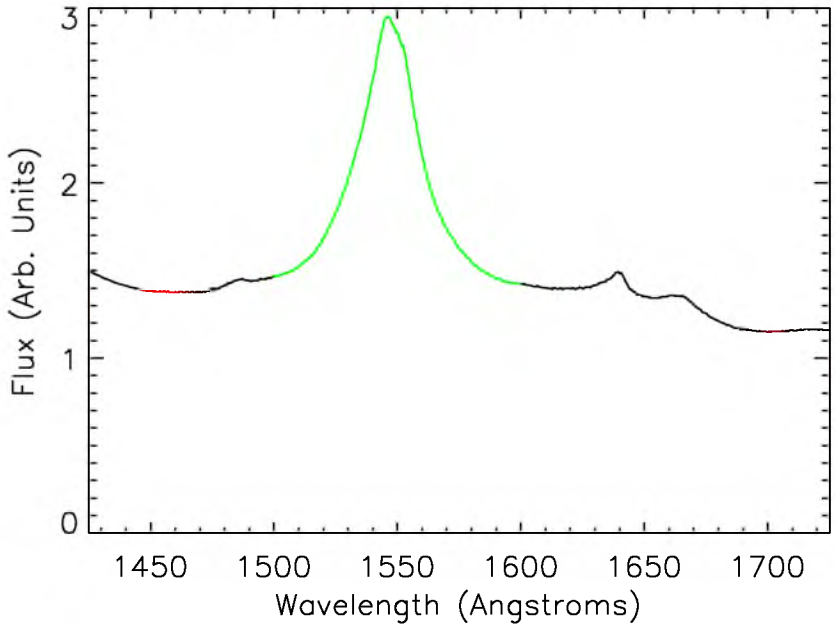

Figure 5.24: The continuum and line fitting regions for the C IV line. The continuum fitting region is shown in red. The line fitting region is shown in green.

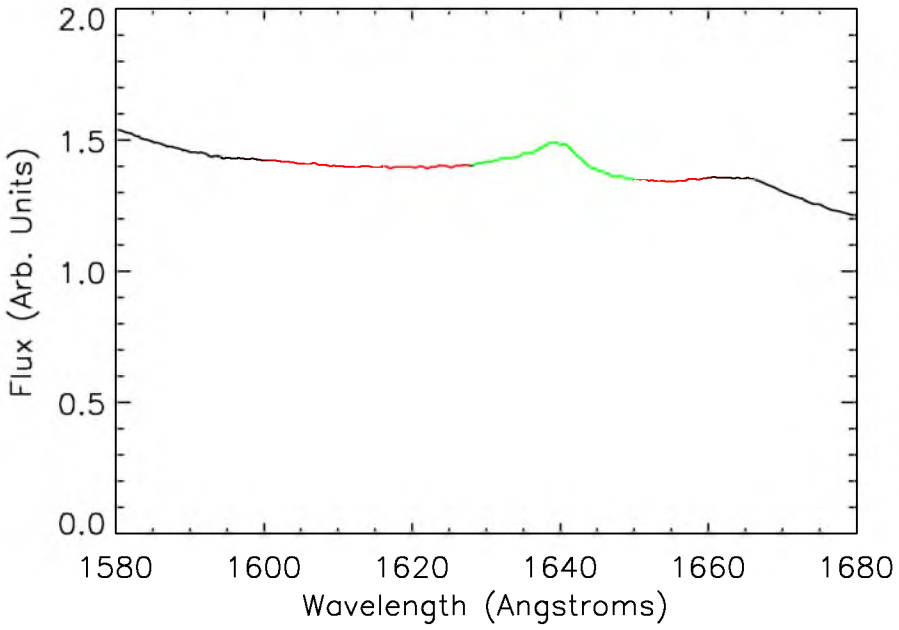

Figure 5.25: The continuum and line fitting regions for the He II line. The continuum fitting region is shown in red. The line fitting region is shown in green.

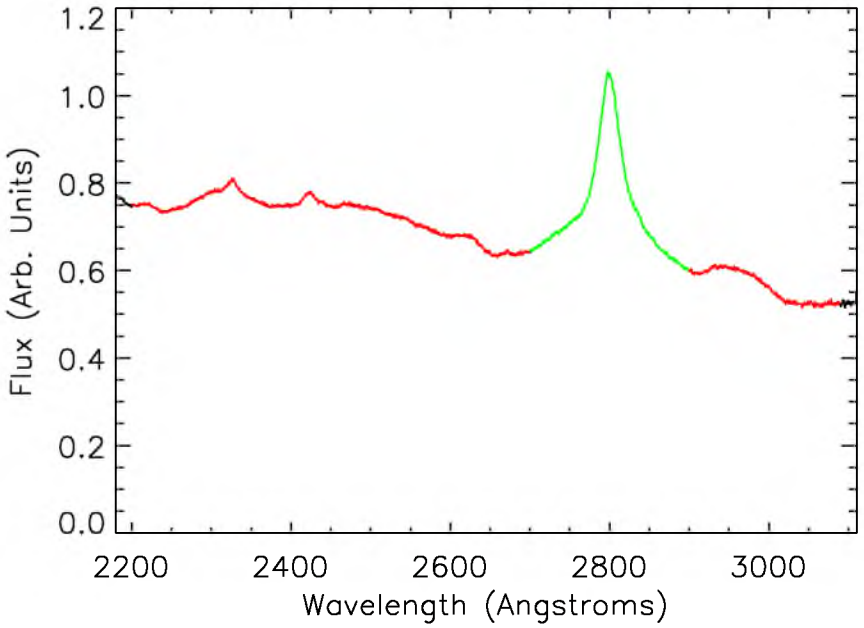

Figure 5.26: The continuum and line fitting regions for the Mg II lines. The continuum fitting region is shown in red. The line fitting region is shown in green.

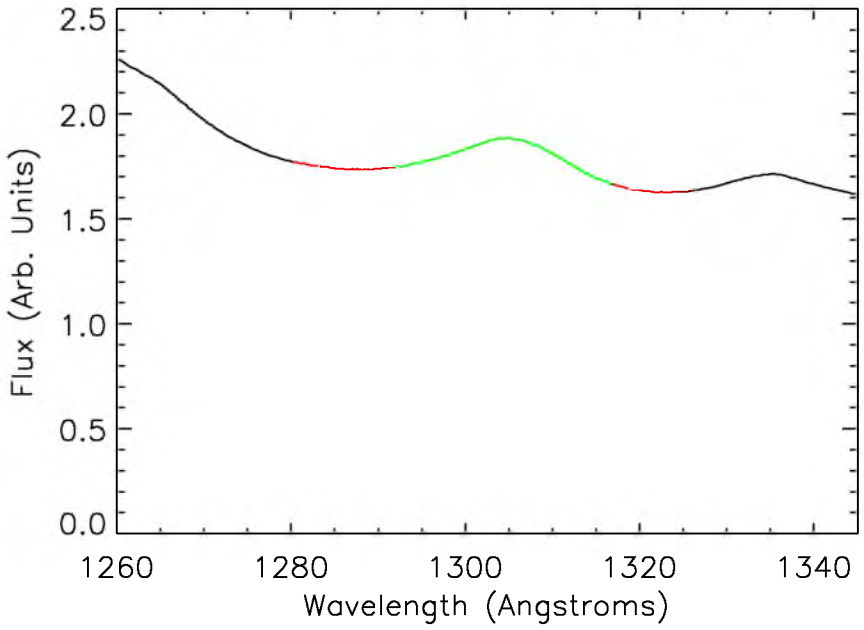

Figure 5.27: The continuum and line fitting regions for the O I and Si II lines. The continuum fitting region is shown in red. The line fitting region is shown in green.

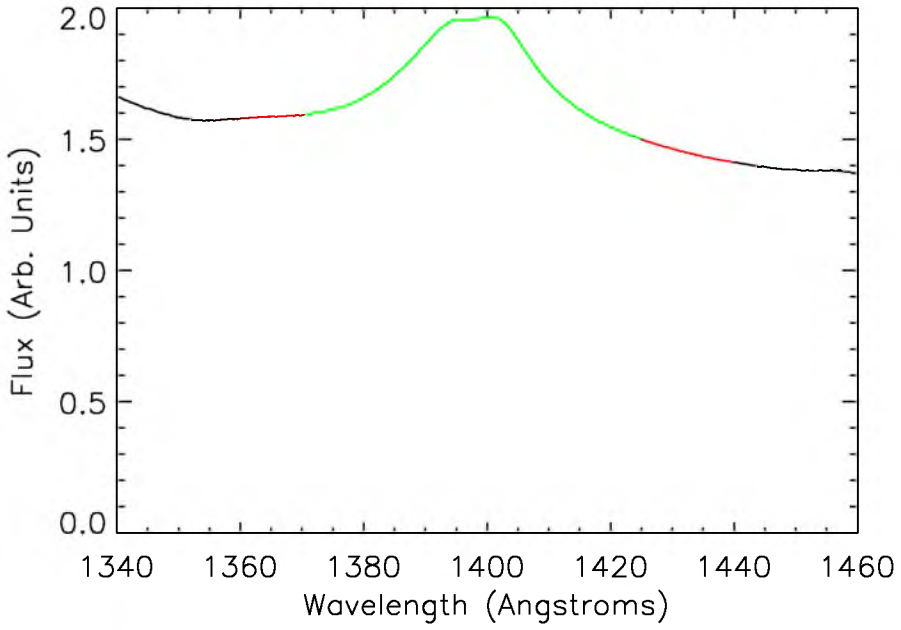

Figure 5.28: The continuum and line fitting regions for the Si IV and O IV lines. The continuum fitting region is shown in red. The line fitting region is shown in green.

CHAPTER 6

THE REDSHIFT DEPENDENCE OF QUASAR SPECTRAL PROPERTIES

In this chapter, I examine the similarities and differences between composite spectra binned by redshift. I create six quasar composite spectra binned by redshift and required to have an i-band absolute magnitude between -25 and -28. The spectra are normalized such that they all have the same mean flux between 1600 Å and 1800 Å. These spectra are presented in Figure 6.1. The clearest difference is at wavelengths shorter than Lyman-α. At these wavelengths, the flux decreases as the redshift increases. This is due to the increasing optical depth as the line of sight extends, and is a product of the Lyman-α Forest. The second clear difference is in the strength of the lines. The C IV line (1549 Å), in particular, is clearly stronger at lower redshift. I use this information to assess the scale of any possible redshift dependence of the Baldwin Effect. This is challenging to do rigorously, as quasar luminosity (upon which the Baldwin Effect is traditionally characterized) evolves with redshift. This is mostly due to target selection. Quasars at higher redshift appear dimmer due to their distance and cosmological effects. Thus, at higher redshift, only high-luminosity quasars are observed in the BOSS program.

Recall, the goal of this work is to assess models purporting to explain the origin of the inverse relationship between line equivalent width and quasar luminosity. None of these models are parameterized on redshift. For completeness, I seek to examine redshift as a possible contributor to the spectral diversity of quasars, which is the goal of the chapter. If redshift is a contributor to this diversity, that is an important statement about the models of the Baldwin Effect. If redshift is not a contributor (or a minor contributor) to the Baldwin Effect, quasar composite spectra in later chapters can be mixed between all redshifts. Vanden Berk et al. (2004) found a correlation between redshift, variability, and emission line equivalent width, and Wu et al. (2010) showed that this effect is mostly due to normalization factors.

The cause of this difference is in the different median i-band absolute magnitudes, as

the Baldwin Effect shows. The difference can be seen in Figure 6.2, and i-band absolute magnitudes are listed in Figure 6.1. The median magnitude varies from -25.70 magnitudes in the lowest redshift bin to -26.61 magnitudes in the highest redshift bin.

The Baldwin Effect is apparent from these composites. The first panel of Figure 6.3 shows the equivalent width of the C IV line with respect to the redshift bin, using the line regions outlined in Table 6.1. Even though the trend is not monotonic, this does show a relationship between redshift bin and equivalent width. This figure mixes redshift and luminosity. The effect of redshift on quasar diversity has not yet been assessed. The equivalent width evolves by a factor of 25% from a redshift of 2.8 to 3.5, but the absolute magnitude changes over that range as well. It has been known for 40 years (Baldwin 1977) that luminosity is a large player in quasar diversity, but the luminosity clearly evolves with redshift. The effect of redshift evolution in quasar properties is clearly complicated by the degeneracy between selection effects and astrophysical evolution. In addition, the hints of a trend with redshift have been shown to be smaller than the trend with luminosity. In this analysis, we attempt to mitigate the effects of selection bias by trimming the sample to have the same median luminosity in each redshift bin. A more careful analysis of redshift evolution is reserved for a future work.

Now, I seek to remove the effect of having different median i-band absolute magnitudes in the redshift bins. I truncate or extend each end of the i-band absolute magnitude ranges in each redshift bin such that the median i-band absolute magnitude is the same. These new composites are found in Figure 6.4. The Lyman-α Forest region is generally unchanged, but the line strengths have changed from previous. This is due to the different i-band absolute magnitude distributions for each composite, shown in Figure 6.5.

This change does not completely remove the inverse relationship between luminosity and line equivalent width. The equivalent widths of lines do change with redshift, but in a different way now that the median i-band absolute magnitude is held constant. Because the shapes of the distributions are very different, the equivalent widths still evolve with redshift. The second panel of Figure 6.3 shows the equivalent width of the C IV line with respect to the redshift bin when the i-band absolute magnitude is held constant. The equivalent width changes by a factor of 12% once the median i-band absolute magnitude is held constant, and this change is not monotonic, and appears to be mostly due to scatter. Thus, more than half of the effect can be attributed to luminosity alone. Bear in mind that this procedure is incomplete, and did not match the shapes of the distributions. This is likely the cause of the remaining difference. This indicates that the effect of redshift on emission line equivalent

width is generally due to correlations with luminosity, not due to a fundamental dependence on redshift, a result also found by Wu et al. (2010).

6.1 Baldwin Effect with Respect to i-Band Absolute Magnitude and Redshift

To extend my examination of the Baldwin Effect, I first create quasar composite spectra binned by redshift and i-band absolute magnitude. Here I show that this trend is actually due to the target selection algorithm selecting brighter quasars at higher redshift. Binning in redshift and magnitude is interesting for multiple reasons. The quasar sample is more uniform when binned by redshift and absolute magnitude. I can find the quasar emission line equivalent widths as a function of both i-band absolute magnitude and redshift, allowing more data points. Furthermore, the slope of the Baldwin Effect can be compared at different redshifts to see if the Baldwin Effect itself changes with redshift. The bins in redshift and i-band absolute magnitude are set in advance, and any bin with fewer than 50 quasars is not made into a quasar composite spectrum as the signal-to-noise is too low to get meaningful data. Table 6.2 shows the properties of each quasar composite spectrum used for this examination.

Figure 6.6, Figure 6.7, Figure 6.8, Figure 6.9, Figure 6.10, Figure 6.11, and Figure 6.12 show the Baldwin effect in each line. Each figure shows the equivalent width versus the median absolute i-band magnitude in the given redshift-luminosity bin. Each figure also shows a simple linear fit to the data points in order to guide the eye. Points and lines are color coded by redshift bin.

Figure 6.6 shows the Baldwin Effect in the C III], Si III], and Al III line complex. Interestingly, the linear fit does seem to fit the data well, a contradiction to the above.

The C II figure (Figure 6.7) shows no Baldwin Effect. Indeed, the effect shown could be interpreted as a reverse-Baldwin Effect as the C II line becomes smaller at dimmer i-band absolute magnitude bins. This is also likely due to low signal-to-noise. This makes the C II line a poor candidate for further studies.

The C IV line was one of the original lines to be examined, which led to the discovery of the Baldwin Effect. Here in Figure 6.8, the Baldwin Effect relationship is very clear. Again, the linear fit does not fit the data very well, indicating a possible linear relationship with flux, not with i-band absolute magnitude.

Figure 6.9 clearly shows the Baldwin Effect, along with the effect that the linear fit does not fit the data very well, indicating a possible linear relationship with flux, not with i-band absolute magnitude.

Figure 6.10 shows the Baldwin Effect very clearly in Mg II. Mg II was one of the original lines to be examined, which led to the discovery of the Baldwin Effect.

Figure 6.11 shows a Baldwin Effect in some redshift bins, but not in others, for the O I and Si II lines. Specifically, the higher the redshift bin, the greater the effect from the Baldwin Effect. This is unexpected. The Baldwin Effect is expected to be constant with increasing redshift. The likely explanation is that the signal-to-noise is too low to get good measurements, and this result is coincidental. Interestingly, the linear fit does not fit the points in each redshift bin very well. An exponential fit would likely represent the data better, indicating that the Baldwin Effect is not linear with magnitude, but linear with flux.

Figure 6.12 shows a clear Baldwin Effect. As with the O I, Si II complex, the linear fit does not fit the data very well, indicating a possible linear relationship with flux, not with i-band absolute magnitude. In addition, the two highest redshift bins seem to have the steepest Baldwin Effect relationship. The Equivalent Width decreases faster in these bins than it does in other bins with respect to the i-band absolute magnitude.

To be included in the analysis of quasar spectral diversity in Chapter 7, a quasar must show a Baldwin Effect relationship without any dependence on redshift. The C IV line, the Mg II line, the Si IV and O IV line complex, and the C III, Si III, Al III line complex pass these criteria and will be analyzed in more depth in Chapter 7.

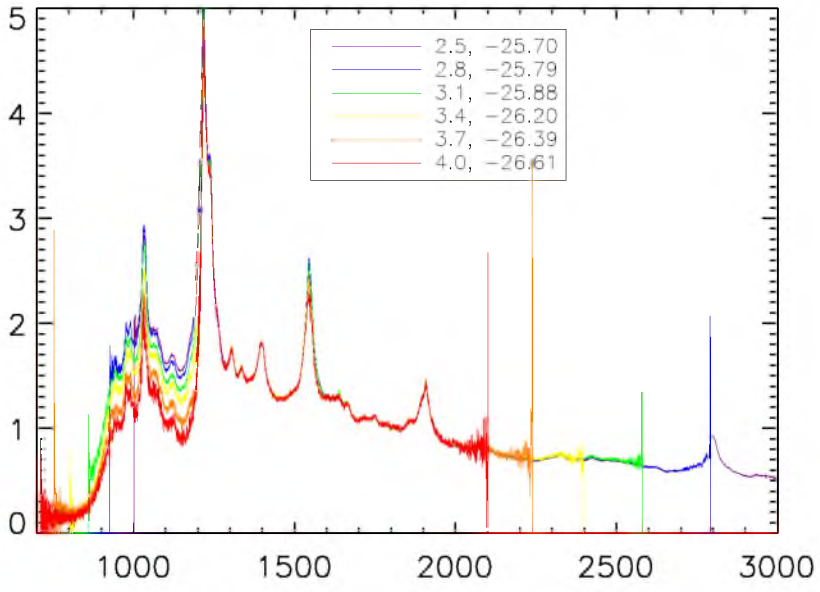

Figure 6.1: The evolution of quasars with redshift. The six quasar composite spectra created from bins in redshift. The legend indicates the center of the redshift bin (in each case, extending 0.15 units of redshift above and below) and the median i-band absolute magnitude.

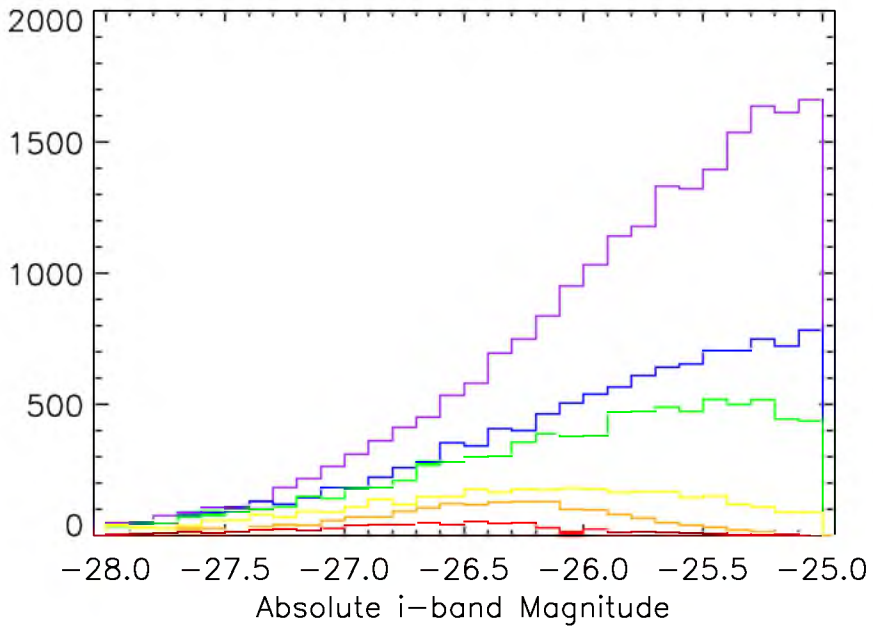

Figure 6.2: A histogram of the i-band absolute magnitude of the six quasar composite spectra created from bins in redshift. The color scheme is identical to Figure 6.1.

Table 6.1: This table shows the lines of interest examined for this study. The "blue continuum" region and "red continuum region" are used for fitting the continuum, while the "line region" indicates the wavelength range over which the equivalent width of the line will be found. The ranges for Mg II and C IV are taken directly from the Shen catalog.

Line	Blue Cont Region	Line Region	Red Cont Region
Mg II	$2200\mathring{A} \leq \lambda \leq 2700\mathring{A}$	$2700\mathring{A} \leq \lambda \leq 2900\mathring{A}$	$2900\mathring{A} \leq \lambda \leq 3090\mathring{A}$
C IV	$1445\mathring{A} \leq \lambda \leq 1465\mathring{A}$	$1500\mathring{A} \leq \lambda \leq 1600\mathring{A}$	$1700\mathring{A} \leq \lambda \leq 1705\mathring{A}$
O I and Si II	$1280\mathring{A} \leq \lambda \leq 1290\mathring{A}$	$1290\mathring{A} \leq \lambda \leq 1315\mathring{A}$	$1315\mathring{A} \leq \lambda \leq 1325\mathring{A}$
C II	$1315\mathring{A} \leq \lambda \leq 1325\mathring{A}$	$1325\mathring{A} \leq \lambda \leq 1350\mathring{A}$	$1350\mathring{A} \leq \lambda \leq 1360\mathring{A}$
Si IV and O IV]	$1360\mathring{A} \leq \lambda \leq 1370\mathring{A}$	$1370\mathring{A} \leq \lambda \leq 1420\mathring{A}$	$1420\mathring{A} \leq \lambda \leq 1440\mathring{A}$
He II	$1600\mathring{A} \leq \lambda \leq 1620\mathring{A}$	$1620\mathring{A} \leq \lambda \leq 1645\mathring{A}$	$1645\mathring{A} \leq \lambda \leq 1660\mathring{A}$
C III]/Si III]/Al III	$1820\mathring{A} \leq \lambda \leq 1840\mathring{A}$	$1840\mathring{A} \leq \lambda \leq 1940\mathring{A}$	$1940\mathring{A} \leq \lambda \leq 1960\mathring{A}$

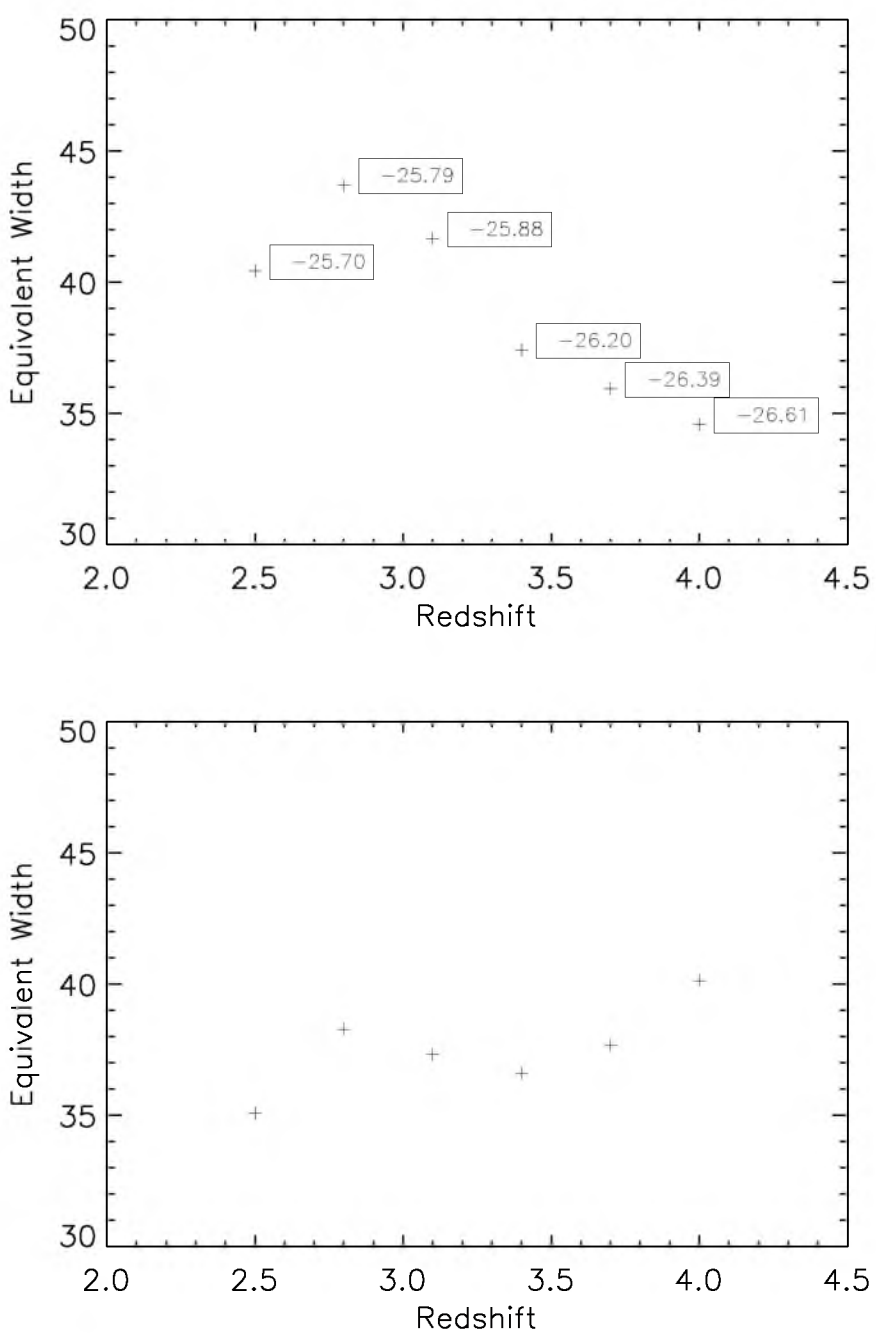

Figure 6.3: The Baldwin Effect observed in redshift binned composites for the C IV line. The first panel shows the equivalent widths of the C IV emission line for quasar composite spectra not matched on median magnitude. This panel also shows the median i-band absolute magnitude for each bin. The second panel shows the equivalent widths of the C IV emission line for quasar composite spectra which have been matched on median magnitude.

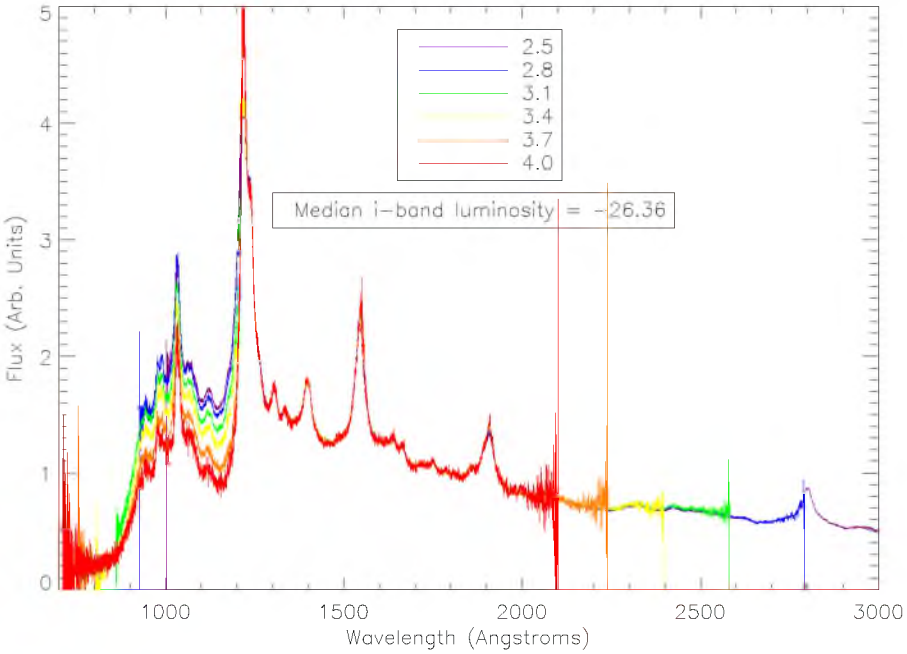

Figure 6.4: The six quasar composite spectra created from bins in redshift. The legend indicates the center of the redshift bin (in each case, extending 0.15 units of redshift above and below) and the median i-band absolute magnitude.

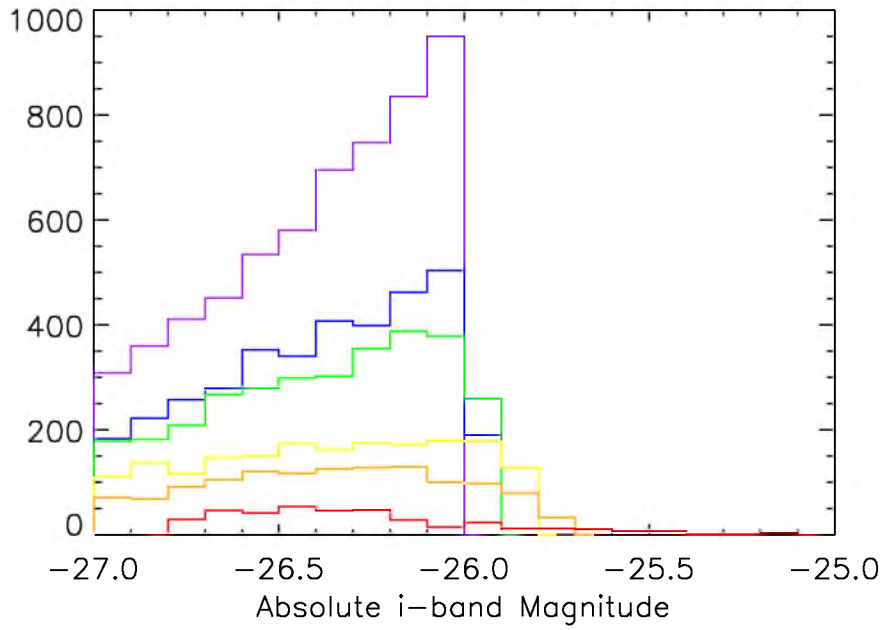

Figure 6.5: A histogram of the i-band absolute magnitude of the six quasar composite spectra created from bins in redshift. The color scheme is identical to Figure 6.4.

Table 6.2: The quasar composite spectra used in the initial tests to determine the redshift dependence on the Baldwin Effect.

Redshift Range	i-band Abs Mag	Median Redshift	Median i Abs Mag	N QSO
$0.00000 \leq z < 2.10000$	$-25 \leq z < -24$	1.62204	-24.3465	5286
$2.10000 \leq z < 2.45000$	$-25 \leq z < -24$	2.29456	-24.5215	21613
$2.45000 \leq z < 2.80000$	$-25 \leq z < -24$	2.57512	-24.5808	11427
$2.80000 \leq z < 3.15000$	$-25 \leq z < -24$	2.93424	-24.7012	3549
$3.15000 \leq z < 3.50000$	$-25 \leq z < -24$	3.21797	-24.8010	617
$0.00000 \leq z < 2.10000$	$-26 \leq z < -25$	1.88369	-25.3139	1135
$2.10000 \leq z < 2.45000$	$-26 \leq z < -25$	2.30208	-25.4219	16460
$2.45000 \leq z < 2.80000$	$-26 \leq z < -25$	2.58713	-25.4420	12229
$2.80000 \leq z < 3.15000$	$-26 \leq z < -25$	2.96336	-25.4674	6225
$3.15000 \leq z < 3.50000$	$-26 \leq z < -25$	3.24968	-25.5462	2664
$3.50000 \leq z < 10.0000$	$-26 \leq z < -25$	3.70568	-25.7616	536
$0.00000 \leq z < 2.10000$	$-27 \leq z < -26$	2.00719	-26.2129	129
$2.10000 \leq z < 2.45000$	$-27 \leq z < -26$	2.31131	-26.3379	6167
$2.45000 \leq z < 2.80000$	$-27 \leq z < -26$	2.59713	-26.3670	5645
$2.80000 \leq z < 3.15000$	$-27 \leq z < -26$	2.97726	-26.4037	3407
$3.15000 \leq z < 3.50000$	$-27 \leq z < -26$	3.28178	-26.4097	2239
$3.50000 \leq z < 10.0000$	$-27 \leq z < -26$	3.71306	-26.4758	1661
$2.10000 \leq z < 2.45000$	$-28 \leq z < -27$	2.31791	-27.2896	1191
$2.45000 \leq z < 2.80000$	$-28 \leq z < -27$	2.61515	-27.2992	1335
$2.80000 \leq z < 3.15000$	$-28 \leq z < -27$	2.97359	-27.3326	1016
$3.15000 \leq z < 3.50000$	$-28 \leq z < -27$	3.29493	-27.3463	782
$3.50000 \leq z < 10.0000$	$-28 \leq z < -27$	3.73554	-27.3217	539
$2.45000 \leq z < 2.80000$	$-29 \leq z < -28$	2.65703	-28.0886	85
$2.80000 \leq z < 3.15000$	$-29 \leq z < -28$	2.99836	-28.1763	114
$3.15000 \leq z < 3.50000$	$-29 \leq z < -28$	3.29326	-28.1686	104
$3.50000 \leq z < 10.0000$	$-29 \leq z < -28$	3.64543	-28.2031	56

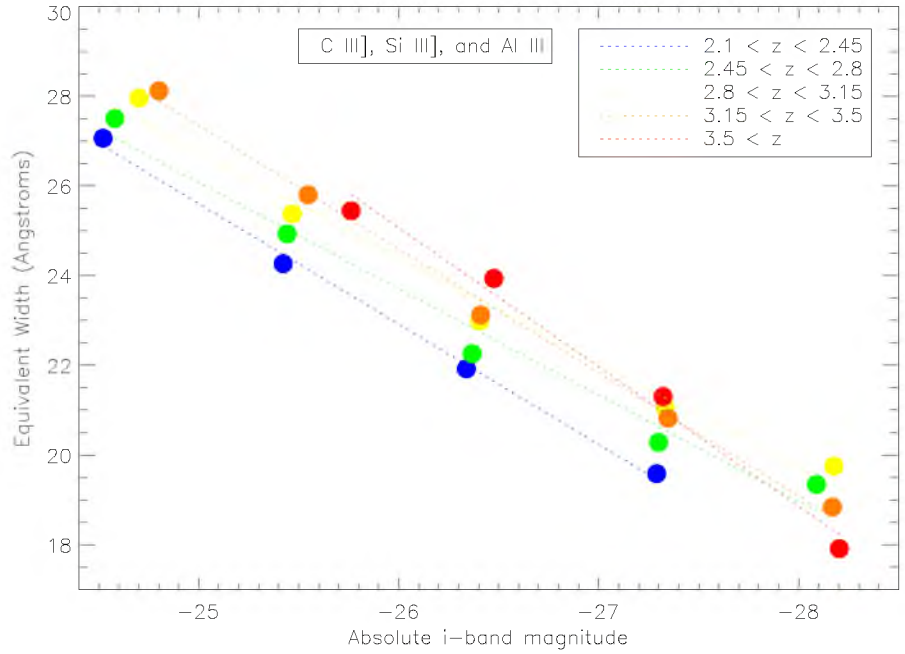

Figure 6.6: Testing for the Baldwin Effect on the C III, Si III, and Al III lines. Higher redshifts are represented by redder colors.

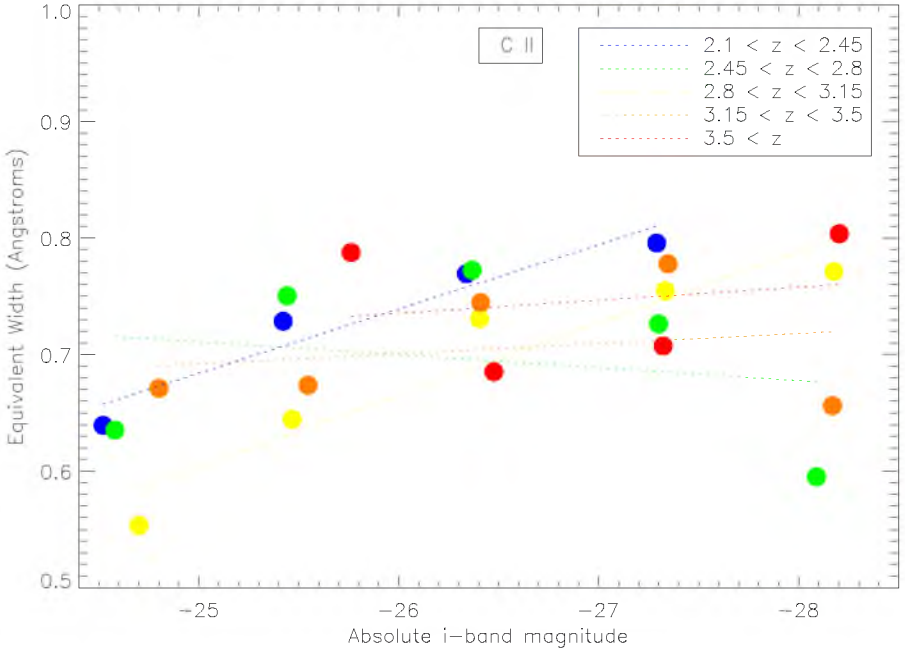

Figure 6.7: Testing for the Baldwin Effect on the C II line. Higher redshifts are represented by redder colors.

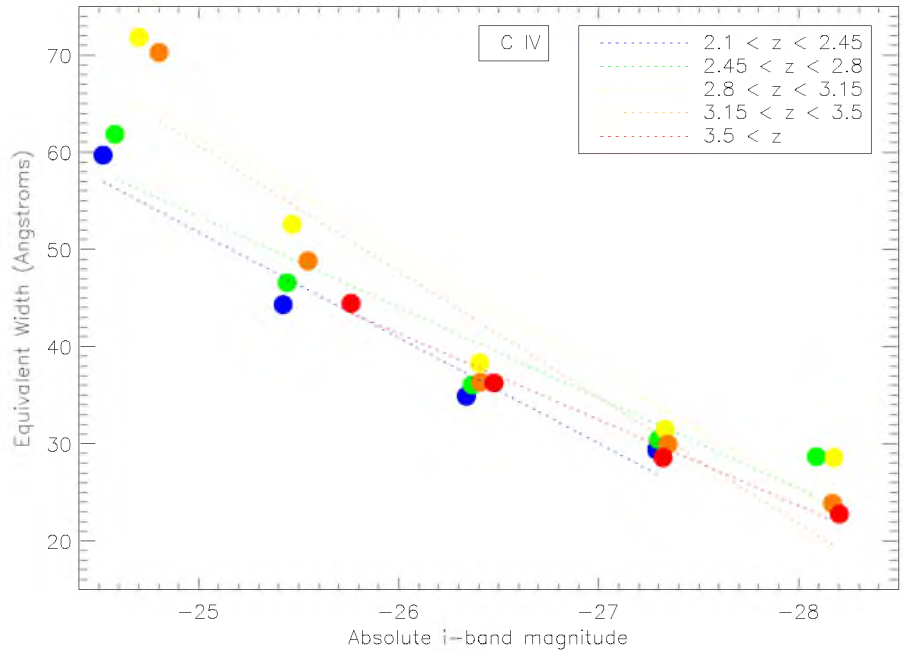

Figure 6.8: Testing for the Baldwin Effect on the C IV line. Higher redshifts are represented by redder colors.

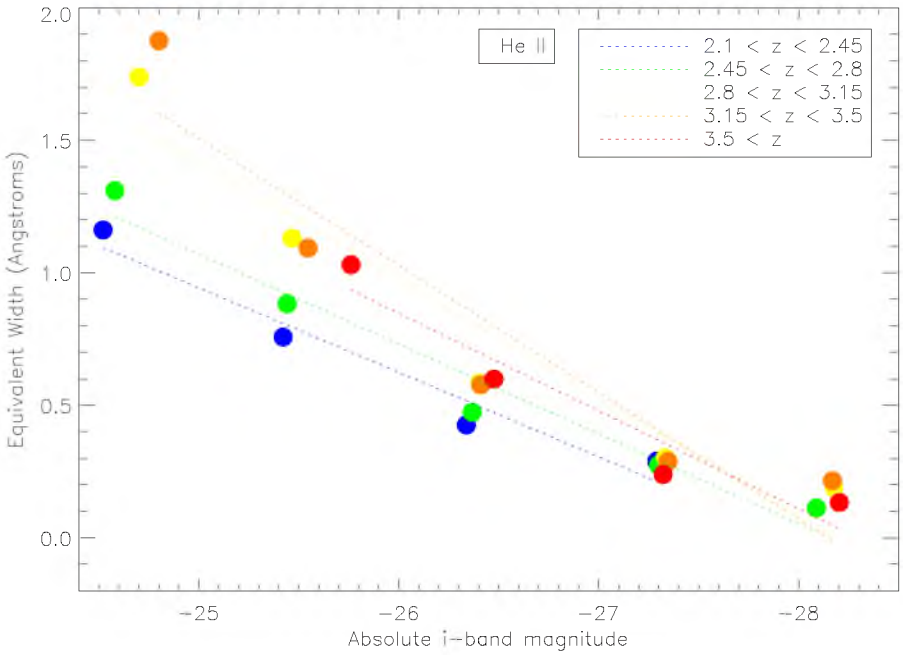

Figure 6.9: Testing for the Baldwin Effect on the He II line. Higher redshifts are represented by redder colors.

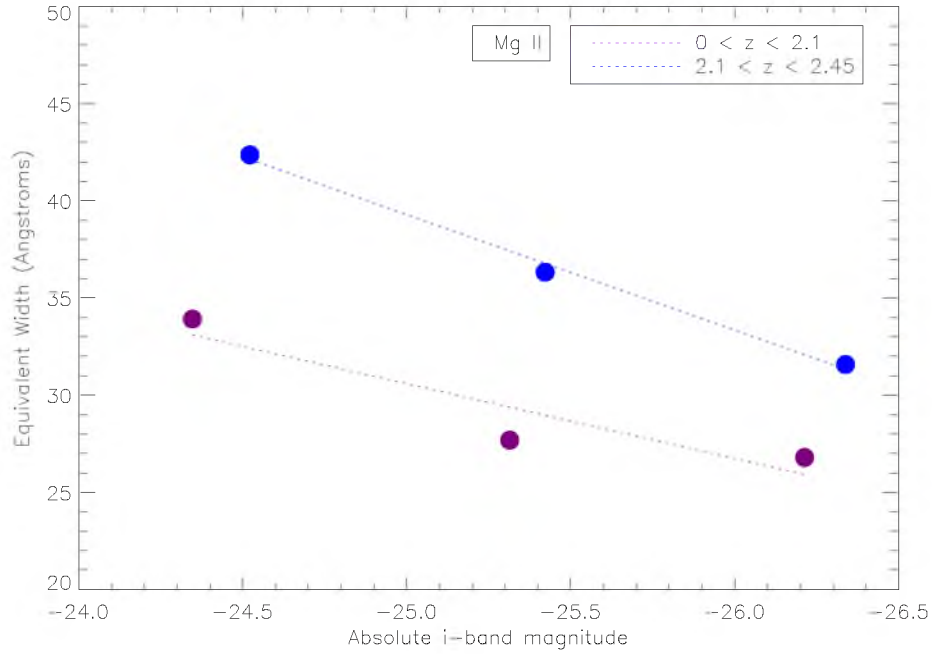

Figure 6.10: Testing for the Baldwin Effect on the Mg II line. Higher redshifts are represented by redder colors.

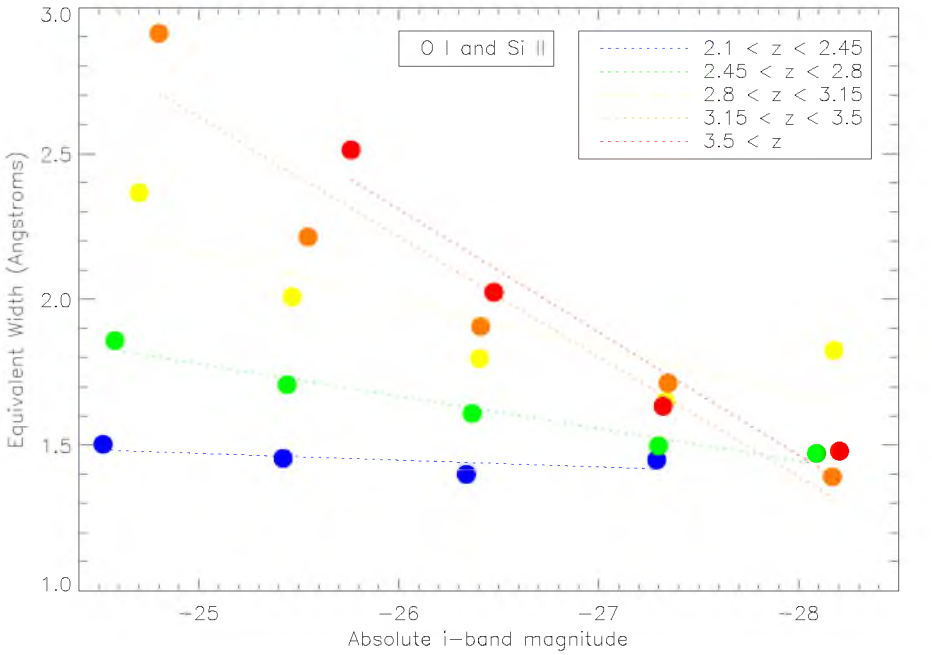

Figure 6.11: Testing for the Baldwin Effect on the O I and Si II lines. Higher redshifts are represented by redder colors.

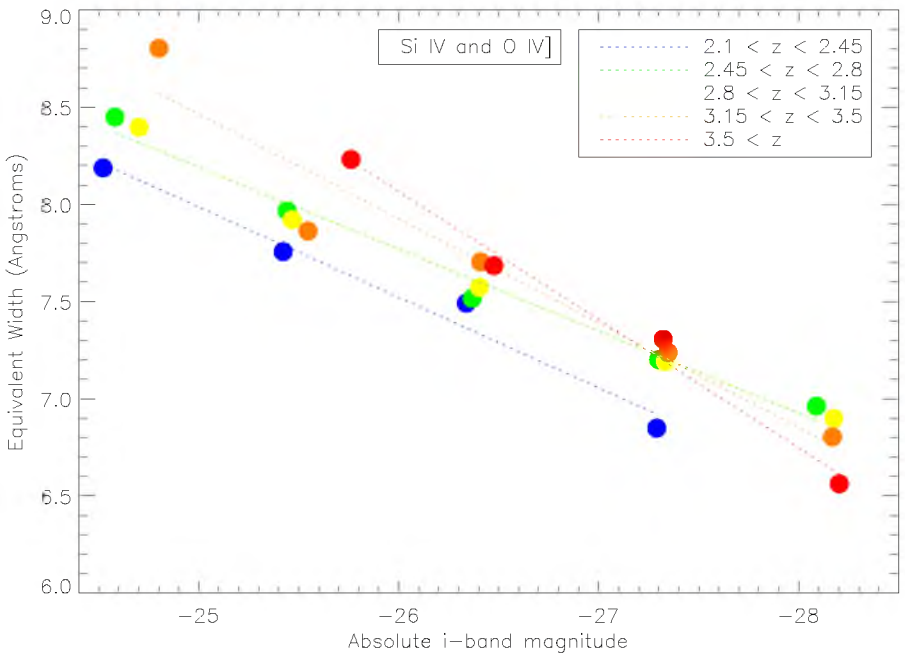

Figure 6.12: Testing for the Baldwin Effect on the Si IV and O IV lines. Higher redshifts are represented by redder colors.

CHAPTER 7

LINEWIDTH RELATIONSHIPS TO QUASAR OBSERVABLES

In this chapter, I create numerous quasar composite spectra and find the equivalent widths of lines in each spectrum. Some of the composites are restricted to have smaller ranges of certain parameters. This is designed to investigate whether or not said parameter contributes to the Baldwin Effect. This will be used to determine which parameters the inverse correlation is and is not dependent on.

Quasar emission line profiles are functions of many variables. The width (usually measured as the FWHM) is a function of black hole mass and the geometry of the accretion disk. The emission line is doppler broadened by the high-velocity gas close to the black hole. The emission line flux is a function of several variables. The emission lines are created by clouds of ionized gas near the black hole. Thus, emission lines require ionizing photons to ionize the gas, and they also require the gas itself. Furthermore, the emission line photons must escape the vicinity of the quasar, placing further constraints on the gas density.

Here, I test three particular models of the Baldwin Effect: Wandel99a, Wandel99b, and Korista. These models, especially the Korista model, are the standard models used to explain the inverse relationship between line equivalent width and quasar luminosity. See Chapter 2 for an explanation of these models. These models have various input parameters, including ionization energies and line energies. Here, I hold some of these parameters fixed at the model parameter while other parameters are free. The Wandel99a model uses a fixed continuum energy of 20 eV, which characterizes the mean energy of ionizing photons in the quasar. In all other cases, parameters are not held fixed.

Ideally, a model would correctly predict the shape and amplitude of the Baldwin Effect. As such, in Section 7.3 I fix additional parameters to their predicted values and rerun this analysis. Initially, the fits are made without restrictions on bolometric luminosity.

In this chapter, I examine the Baldwin Effect in traditional terms, parameterized against luminosity. Here, I will fit the previously discussed models to the data. I will then restrict

my luminosity sample, since previous works conclude the models hold better at higher luminosities. Next, I will examine correlations between parameters which may cause an observed inverse relationship between line equivalent width and quasar luminosity, even though it is just due to correlation. Then, I will examine the Baldwin Effect and Modified Baldwin Effect as parameterized against bolometric luminosity, black hole mass, Eddington ratio, and spectral index. Finally, I will restrict the samples in such a way as to determine whether the bolometric luminosity or the black hole mass has the greater contribution to quasar spectral diversity.

7.1 Analysis

7.1.1 Tests to Baldwin Effect Models at all Luminosities

I create composites of quasars in bins of increasing bolometric luminosity. These composites allow for a detailed investigation of the traditional Baldwin Effect.

Korista found that their models fit the data better at higher bolometric luminosities. Thus, here we rerun the above analysis to fit the data at bolometric luminosities greater than $10^{45.5} ergs^{-1}$. All other aspects of these tests are identical to the above. Shown in Figure 7.1 are the results for the Korista model tested on the C IV line. The fit parameters are listed in Table 7.1 and in the legends of the figures. These show that the fit improves slightly when the lower luminosity quasars are removed.

The Wandel99a model is taken to be

$$EW \approx exp(\frac{E_I - E_{ion}}{E_c L_{46}^{-1/4}}) \tag{7.1}$$

The W99b model is taken to be

$$EW \approx M^x \tag{7.2}$$

where M is the mass of the quasar. The Korista model is taken to be

$$log(EW) = \alpha + \beta log(\lambda L_\lambda) \tag{7.3}$$

with α and β being constants for each emission line, given in their paper. All data are fit to these equations and the results are as shown.

As can be seen from Table 7.2, the Wandel99a model produces very poor fits to the data, failing to reproduce the prediction and failing to predict the data well. As can be seen from Table 7.3, the Wandel99b model results in a better fit to the data, but with the exponent as a free parameter. The Korista model consistently produces good fits which are often close to the predicted value (excluding the He II line, which has an exponent more than a factor of two off from the prediction), as can be seen from Table 7.1.

7.2 Bolometric Luminosity, Linear Fit

In this section, I fit a simple linear fit to the luminosity data to be used in comparing the efficacy of a traditional Baldwin Effect against a Modified Baldwin Effect. Fits to the data are shown in Table 7.4.

7.3 Comparing Modified Baldwin Effect Parameterizations

Here, I compare the strength of the Modified Baldwin Effect when using various parameterizations. This will identify which parameters are the most important in causing the Baldwin Effect or Modified Baldwin Effect. To do this, I create quasar composite spectra in the same way as detailed in Section 5.3. I order the sample from lowest to highest of the quantity I wish to examine and create composites from that. In this case, I take spectra in sets of 750 instead of 2000. Thus, the first 750 quasar spectra are used to make a composite, the second 750 spectra make the next composite, etc. As the spectra have been ordered by some observable (bolometric luminosity black hole mass, Eddington ratio, or spectral index), each composite will have a different (and monotonically increasing from one to the next) mean observable quantity. The equivalent width of each line or set of lines is found in each composite.

Figures 7.2, 7.3, 7.4, 7.5, 7.6, 7.7, 7.8, 7.9, 7.10, 7.11, 7.12, 7.13, 7.14, 7.15, 7.16, and 7.17 show the equivalent width measurements when parameterized against the observables. Bolometric luminosity and black hole mass show steep slopes and can thus be considered to have a strong input to the Baldwin Effect. Eddington ratio and spectral index have highly nonlinear relationships with equivalent width, and can thus be considered to have weak contributions to the Baldwin Effect. In Figure 7.18 and Figure 7.19, I focus on the results from the C IV line. Clearly, parameterizing quasar spectral diversity on bolometric luminosity and black hole mass offer the best results, as in both cases the trend is nearly monotonic. By parameterizing the Baldwin Effect on the bolometric luminosity, the trend is approximately monotonic within error bars and shows slope evolution. With black hole mass, the trend is monotonic except at low black hole mass, and the trend is more linear at moderate black hole masses. The trend with Eddington Ratio and Spectral Index are not monotonic and show a very complex relationship. Trends with bolometric luminosity and black hole mass warrant further study.

To test the characteristic strength of each parameter in influencing the Baldwin Effect, I find the slope of the Baldwin Effect parameterized against each parameter and divide that by the 68% confidence interval of the parameter in question. Greater values denote a

stronger inverse correlation between line equivalent width and quasar luminosity.

As can be seen from Table 7.4, the bolometric luminosity and the black hole mass contribute the most to the Baldwin Effect. However, as demonstrated by Figure 5.12, these quantities are strongly correlated. The Eddington ratio and spectral index have a much smaller effect on quasar spectral diversity.

Here, I examine the relative contributions of bolometric luminosity and black hole mass to quasar spectral diversity. To find the contribution of black hole mass to the traditional Baldwin Effect, I find a small range in black hole masses and use only those quasars to assess the traditional (versus bolometric luminosity) Baldwin Effect. The range is chosen to maximize (or nearly maximize) the number of quasars usable. The range of black hole masses chosen is from $10^{8.7}$ to $10^{8.8}$ solar masses. I compare the slope of the Baldwin Effect with and without the cut. If the slope decreases when the cut is applied, then the black hole mass is more important than the bolometric luminosity in the Baldwin Effect. If the slope stays the same, both bolometric luminosity and black hole mass are necessary to model the Baldwin Effect. If the slope increases, then the bolometric luminosity must be less important than the black hole mass. The reverse is also considered, parameterizing against black hole mass and choosing a narrow range of bolometric luminosity ($10^{46.1-46.2} ergs^{-1}$). The slope of the fits are again multiplied by the 68% confidence interval of the original distribution of the parameter. The Eddington Ratio and Spectral Index parameterizations are disfavored, while the Bolometric Luminosity and Black Hole Mass are favored.

In the statistically significant cases of the C IV line and the C III, Si III, and AL III lines the fit worsens when the alternate parameter is fixed. Figure 7.20 shows the results from the analysis of the C IV line. In both cases, there is a significant amount of scatter, making the trends hard to interpret. Determining which parameter is more significant from these data is challenging.

Fundamentally, a quasar can be described by the black hole mass and the accretion efficiency (Eddington Ratio). The luminosity of a quasar is a function of those two quantities, and is not fundamental in and of itself. Thus, given that the trends with bolometric luminosity and black hole mass are on order the same, I claim that these results indicate the possibility that quasar spectral diversity in the Baldwin Effect is more of a function of black hole mass, and secondarily a function of bolometric luminosity.

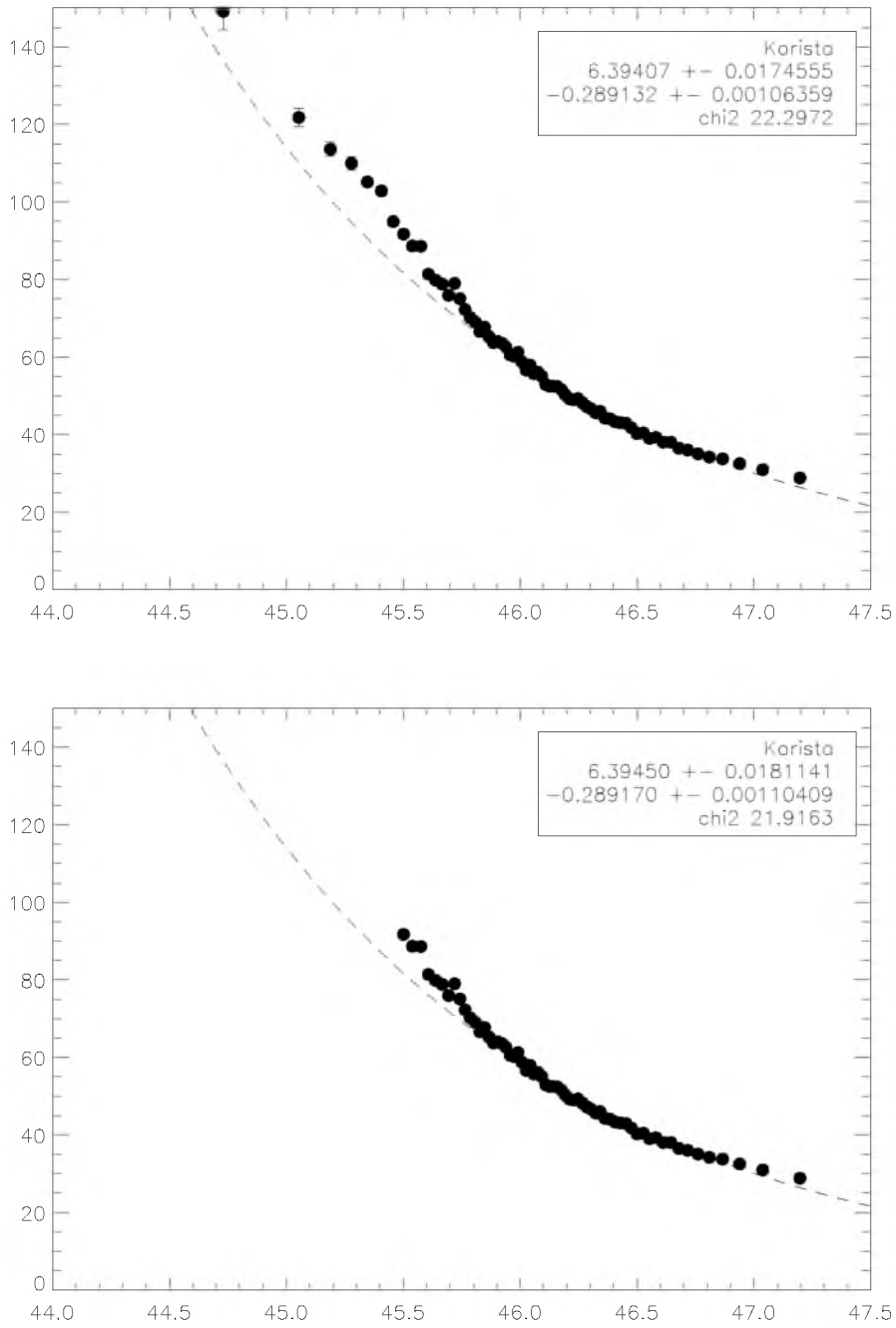

Figure 7.1: The Baldwin Effect detected in the C IV emission line. First Panel: The C IV line equivalent width, showing a Baldwin Effect, and the fit statistics for the Korista model. Second Panel: The C IV line equivalent width, showing a Baldwin Effect, and the fit statistics for the Korista model. Bins with an average bolometric luminosity less than $10^{45.5} ergs^{-1}$ are ignored in the fit.

Table 7.1: The quality of the fits using the Korista model are shown. Comparisons to the predictions when using high-luminosity quasars are also indicated, as is the quality of the fit.

Line	Korista Fit	Korista Prediction	Korista χ^2
C IV	-0.29 ± 0.001	-0.20	23
He II	-0.49 ± 0.01	-0.20	0.74
Si IV and O IV]	-0.089 ± 0.002	-0.10	1.8
C III]/Si III]/Al III	-0.134 ± 0.001	-0.11	2.64

Table 7.2: The quality of the fits using the Wandel99a (W99a) model are shown. Comparisons to the predictions when using high-luminosity quasars are also indicated, as is the quality of the fit.

Line	W99a Fit	W99a Prediction	W99a χ^2
C IV	-207 ± 19	-40.0	1.6e11
He II	-61.5 ± 9	-46.8	2043
Si IV and O IV]	-125 ± 65	-24.6	29000
C III]/Si III]/Al III	-140. ± 44	-17.8	55000

Table 7.3: The quality of the fits using the Wandel99b (W99b) model are shown. Comparisons to the predictions when using high-luminosity quasars are also indicated, as is the quality of the fit.

Line	W99b Fit	W99b Prediction	W99b χ^2
C IV	-0.29 ± 0.0001	-0.25	118
He II	-0.49 ± 0.004	-0.25	4.1
Si IV and O IV]	-0.088 ± 0.001	-0.25	8.9
C III]/Si III]/Al III	-0.13 ± 0.001	-0.25	13.5

Table 7.4: Slope of Baldwin Effect divided by 68% confidence interval for that parameter, in each line used.

Parameter	C IV	He II	Si IV, O IV	C III, Si III, Al III
Bolometric Luminosity	-22.8 ± 0.8	-0.50 ± 0.01	-1.48 ± 0.08	-5.8 ± 0.3
Black Hole Mass	-14.2 ± 0.4	-0.73 ± 0.03	-1.23 ± 0.09	-2.92 ± 0.10
Eddington Ratio	-5.0 ± 0.7	-0.13 ± 0.03	0.00 ± 0.04	-1.69 ± 0.05
Spectral Index	1.6 ± 0.3	0.03 ± 0.01	0.39 ± 0.02	0.58 ± 0.09

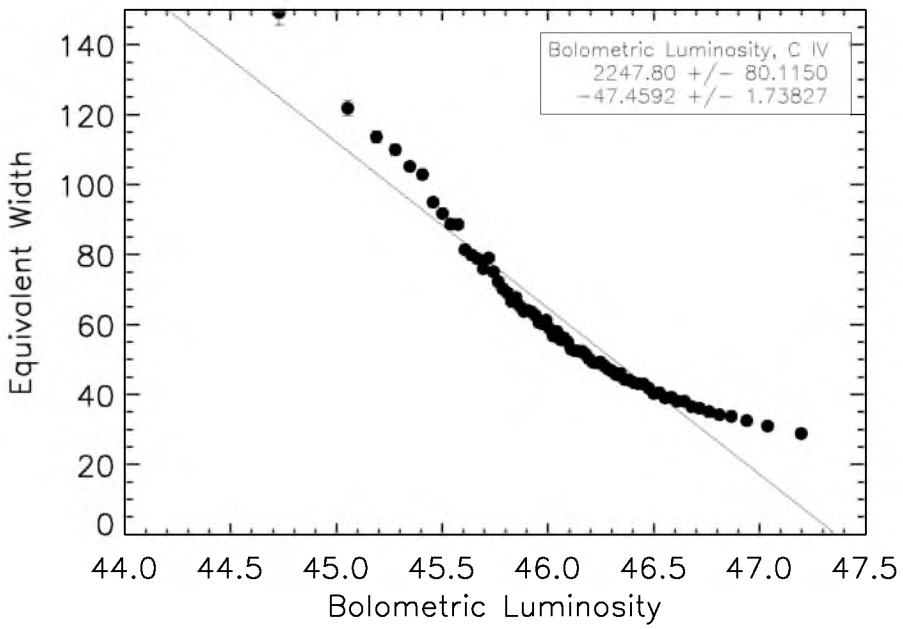

Figure 7.2: The Modified Baldwin Effect parameterized against the Eddington Ratio and considered using the C IV emission line. The C IV equivalent width is plotted against the log base ten of the eddington ratio.

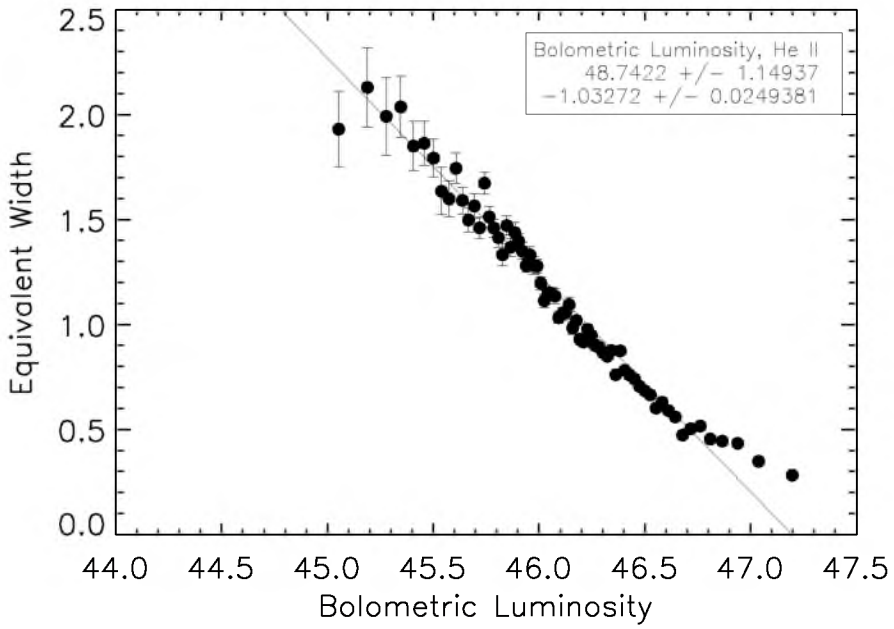

Figure 7.3: The Modified Baldwin Effect parameterized against the Eddington Ratio and considered using the He II emission line. The He II equivalent width is plotted against the log base ten of the eddington ratio.

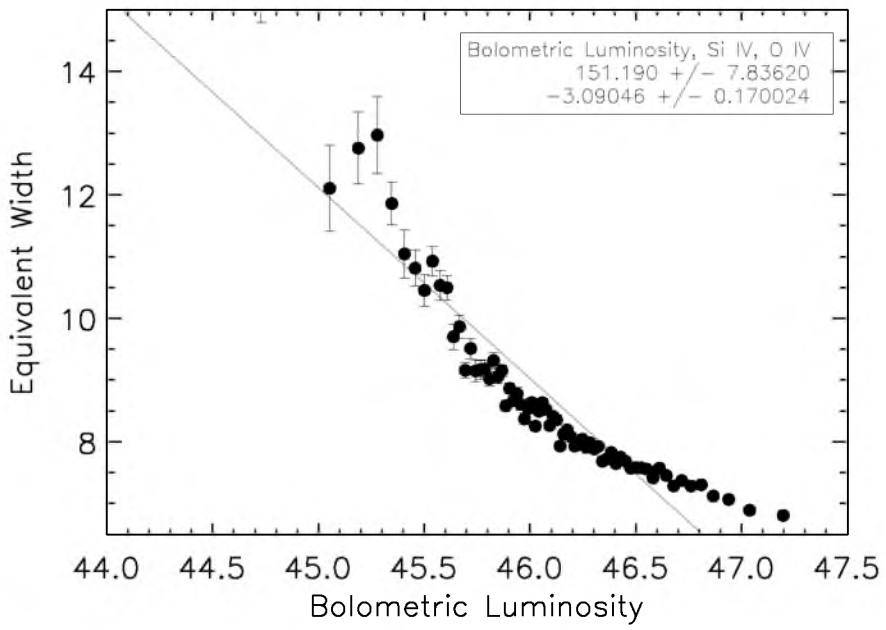

Figure 7.4: The Modified Baldwin Effect parameterized against the Eddington Ratio and considered using the Si IV and O IV] emission lines. The Si IV and O IV] equivalent width is plotted against the log base ten of the eddington ratio.

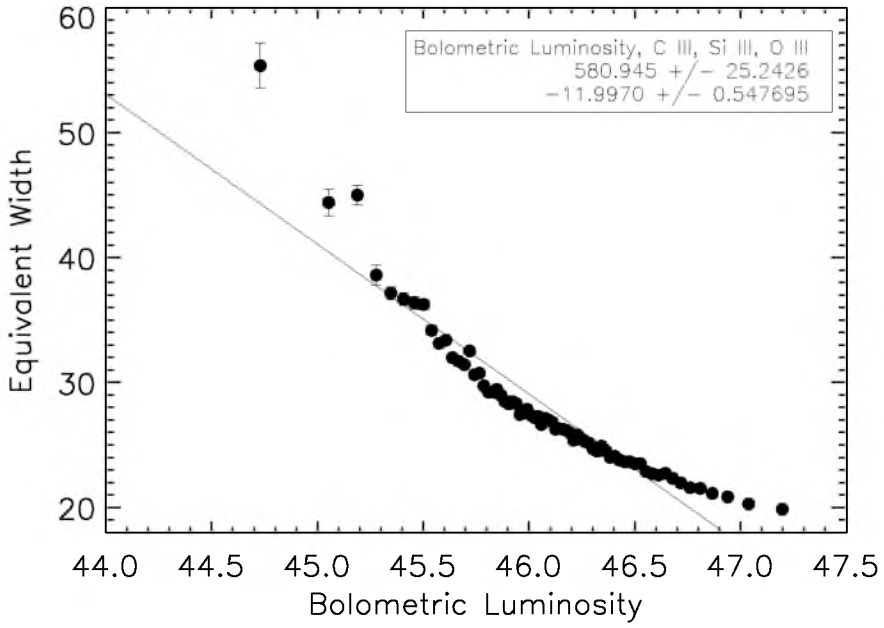

Figure 7.5: The Modified Baldwin Effect parameterized against the Eddington Ratio and considered using the C III], Si III], and Al III emission lines. The C III], Si III], and Al III equivalent width is plotted against the log base ten of the eddington ratio.

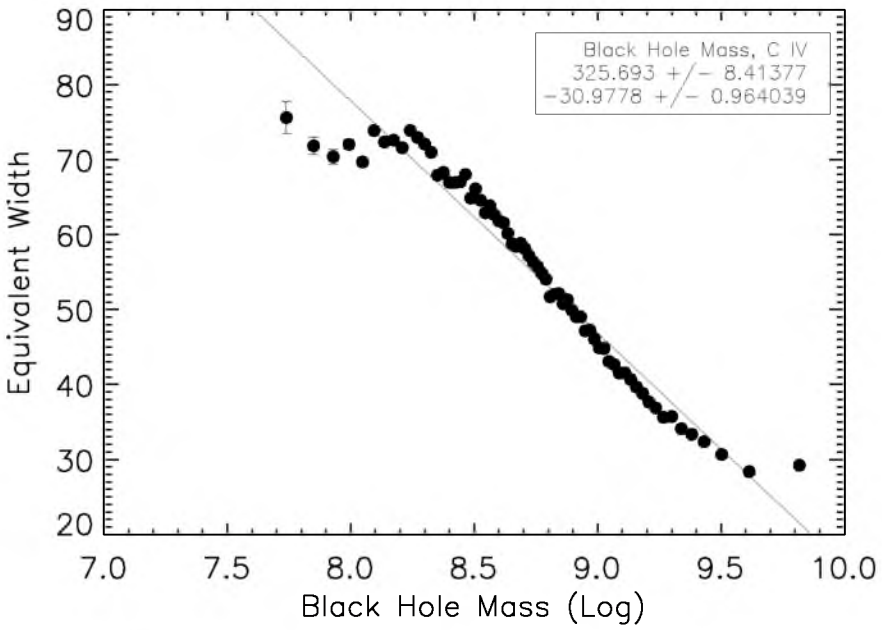

Figure 7.6: The Modified Baldwin Effect parameterized against the quasar black hole mass and considered using the C IV emission line. The C IV equivalent width is plotted against the log base ten of the black hole mass in solar units.

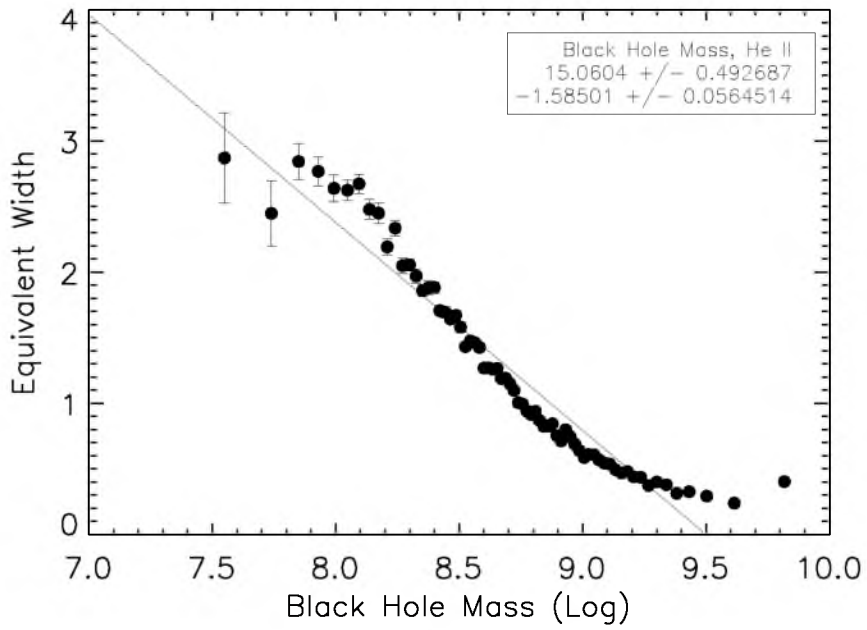

Figure 7.7: The Modified Baldwin Effect parameterized against the quasar black hole mass and considered using the He II emission line. The He II equivalent width is plotted against the log base ten of the black hole mass in solar units.

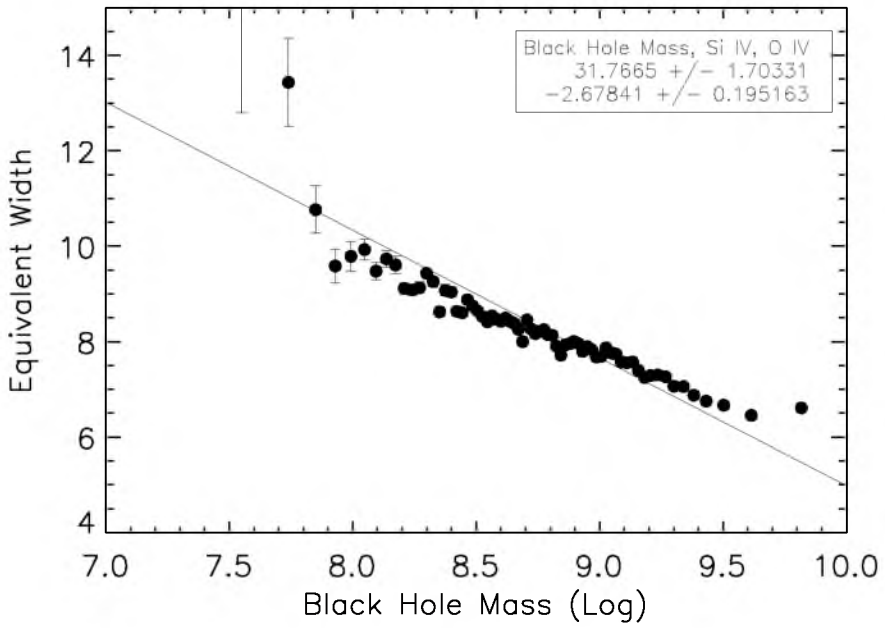

Figure 7.8: The Modified Baldwin Effect parameterized against the quasar black hole mass and considered using the Si IV and O IV] emission lines. The Si IV and O IV] equivalent width is plotted against the log base ten of the black hole mass in solar units.

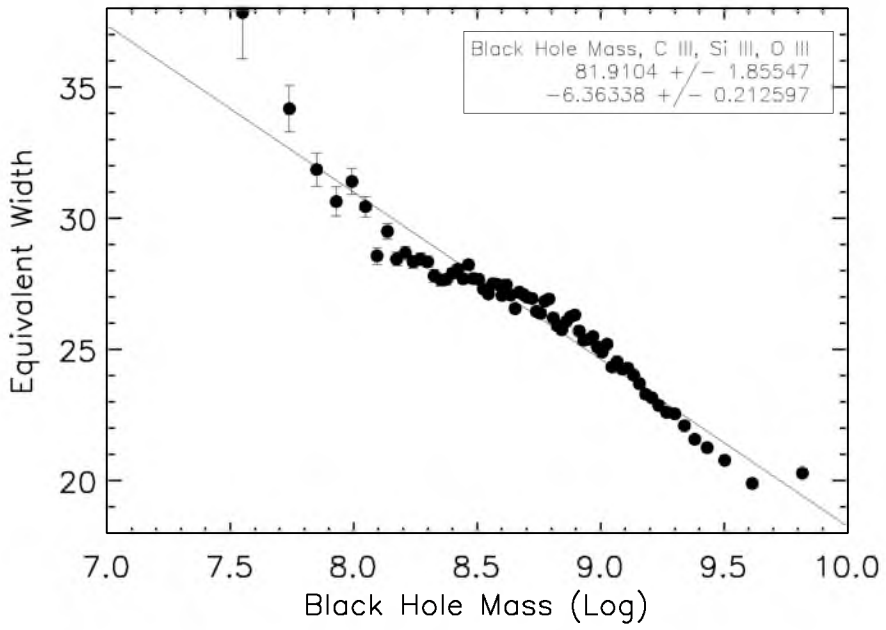

Figure 7.9: The Modified Baldwin Effect parameterized against the quasar black hole mass and considered using the C III], Si III], and Al III emission lines. The C III], Si III], and Al III equivalent width is plotted against the log base ten of the black hole mass in solar units.

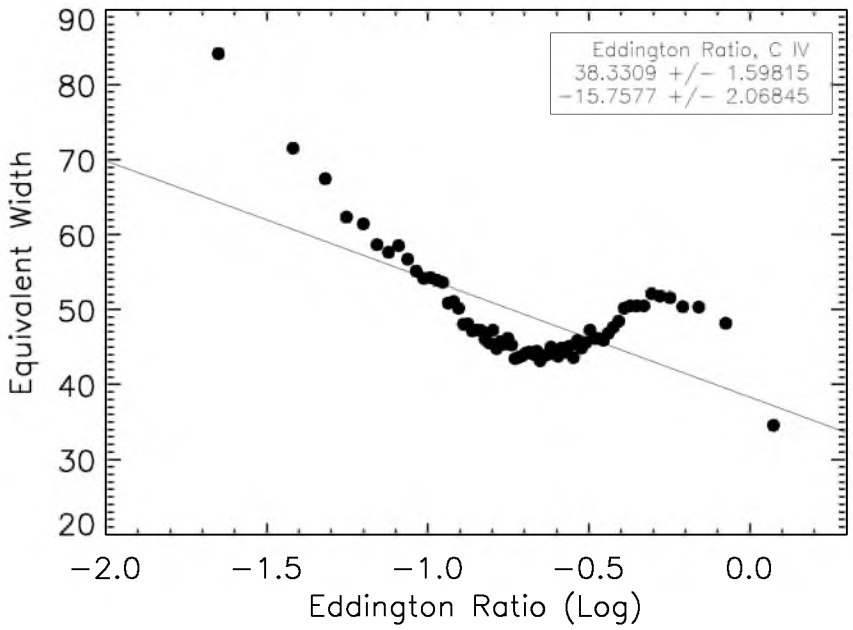

Figure 7.10: The Modified Baldwin Effect parameterized against the Eddington Ratio and considered using the C IV emission line. The C IV equivalent width is plotted against the log base ten of the eddington ratio.

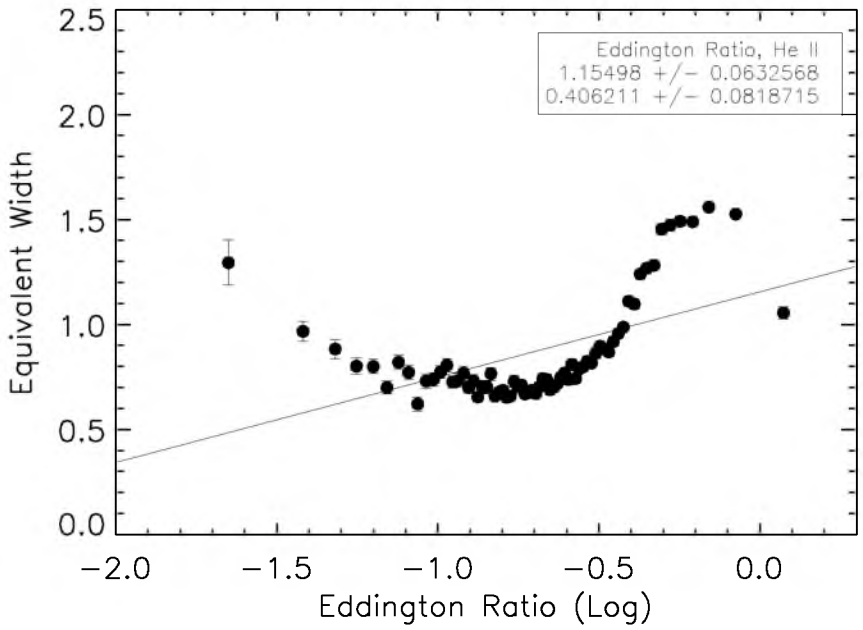

Figure 7.11: The Modified Baldwin Effect parameterized against the Eddington Ratio and considered using the He II emission line. The He II equivalent width is plotted against the log base ten of the eddington ratio.

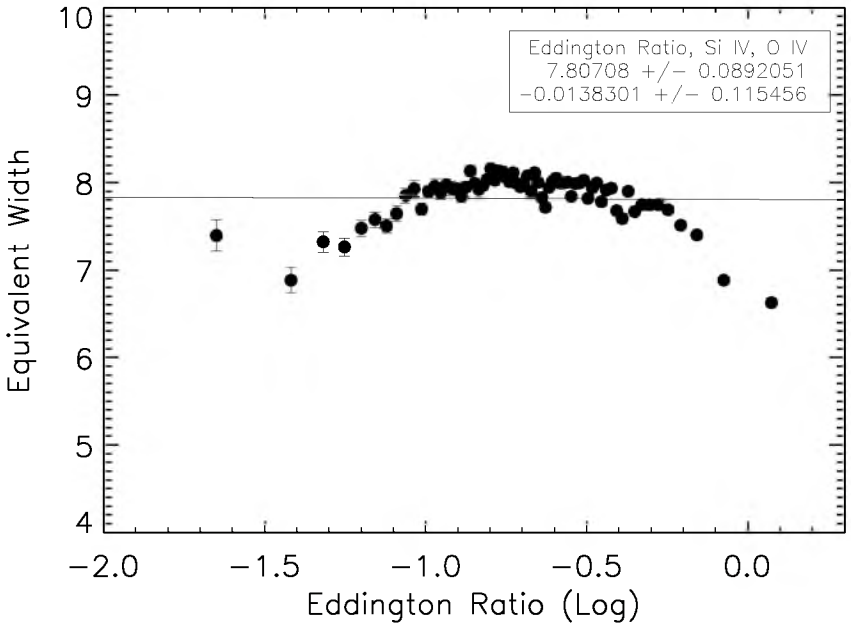

Figure 7.12: The Modified Baldwin Effect parameterized against the Eddington Ratio and considered using the Si IV and O IV] emission lines. The Si IV and O IV] equivalent width is plotted against the log base ten of the eddington ratio.

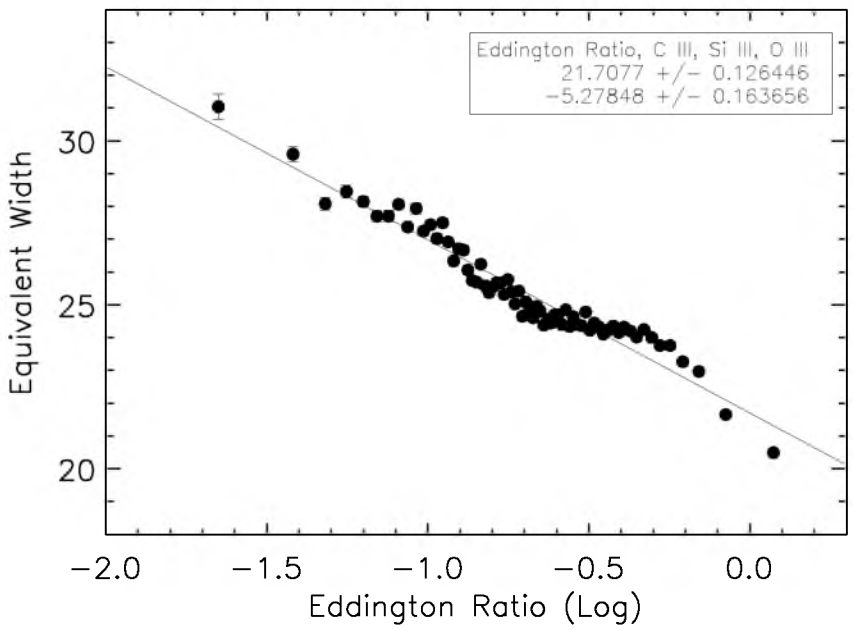

Figure 7.13: The Modified Baldwin Effect parameterized against the Eddington Ratio and considered using the C III], Si III], and Al III emission lines. The C III], Si III], and Al III equivalent width is plotted against the log base ten of the eddington ratio.

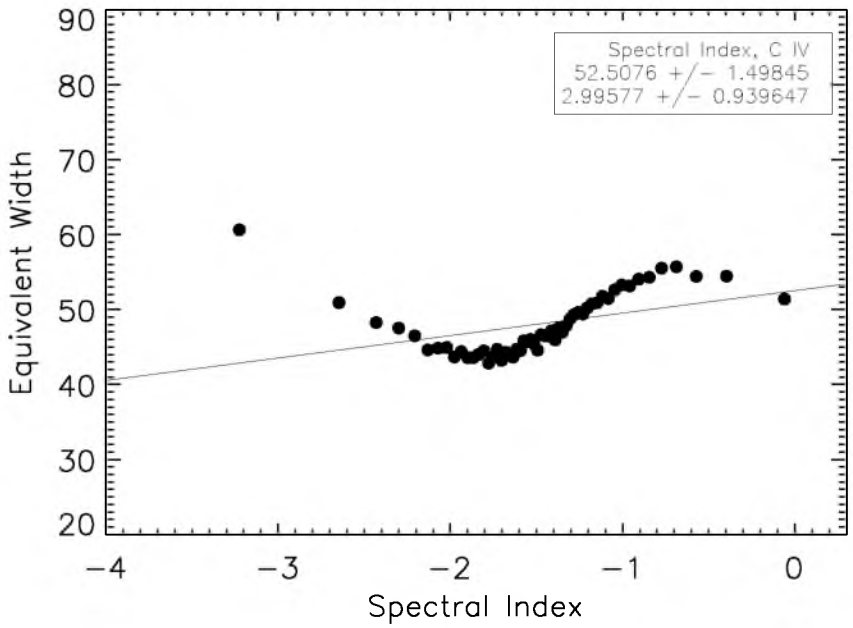

Figure 7.14: The Modified Baldwin Effect parameterized against the quasar continuum spectral index and considered using the C IV emission line. The C IV equivalent width is plotted against the quasar continuum spectral index.

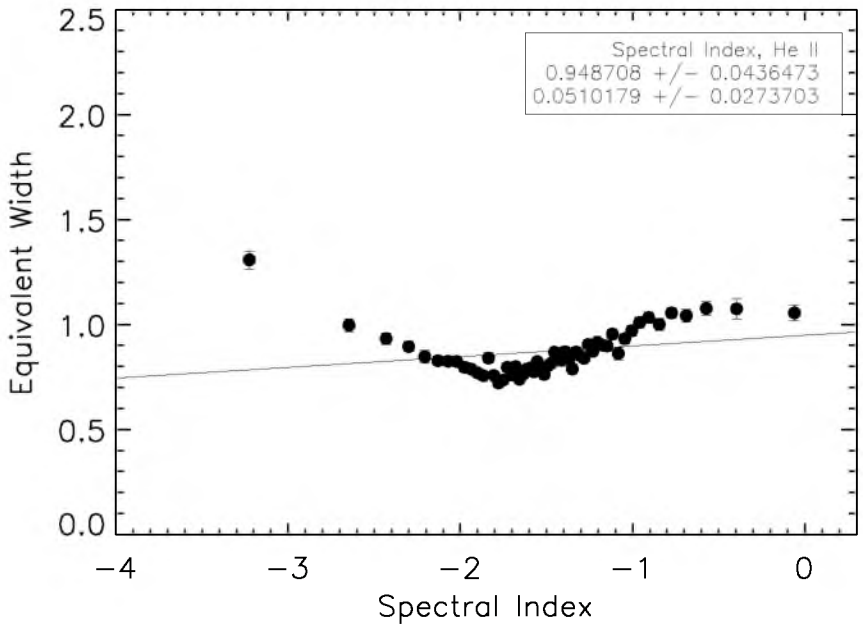

Figure 7.15: The Modified Baldwin Effect parameterized against the quasar continuum spectral index and considered using the He II emission line. The He II equivalent width is plotted against the quasar continuum spectral index.

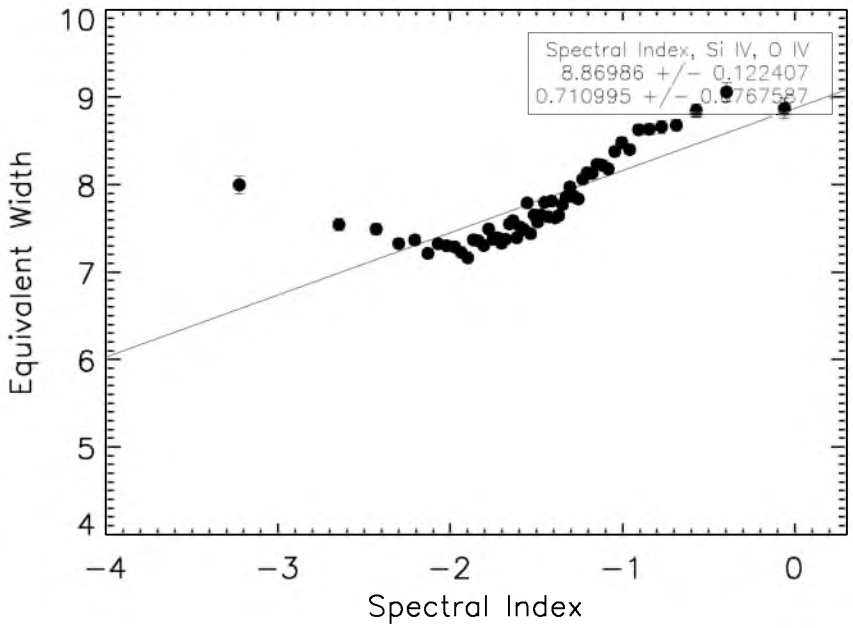

Figure 7.16: The Modified Baldwin Effect parameterized against the quasar continuum spectral index and considered using the Si IV and O IV] emission lines. The Si IV and O IV] equivalent width is plotted against the quasar continuum spectral index.

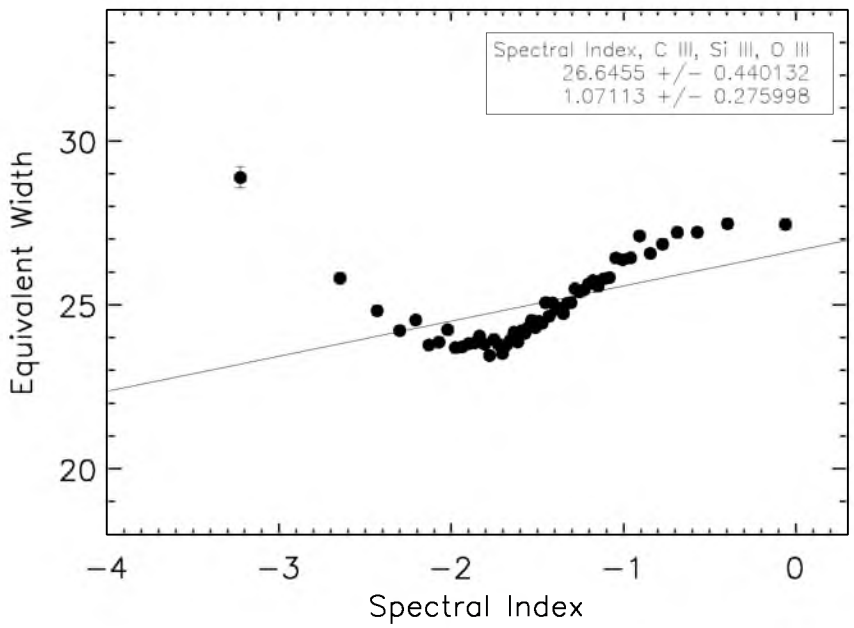

Figure 7.17: The Modified Baldwin Effect parameterized against the quasar continuum spectral index and considered using the C III], Si III], and Al III emission lines. The C III], Si III], and Al III equivalent width is plotted against the quasar continuum spectral index.

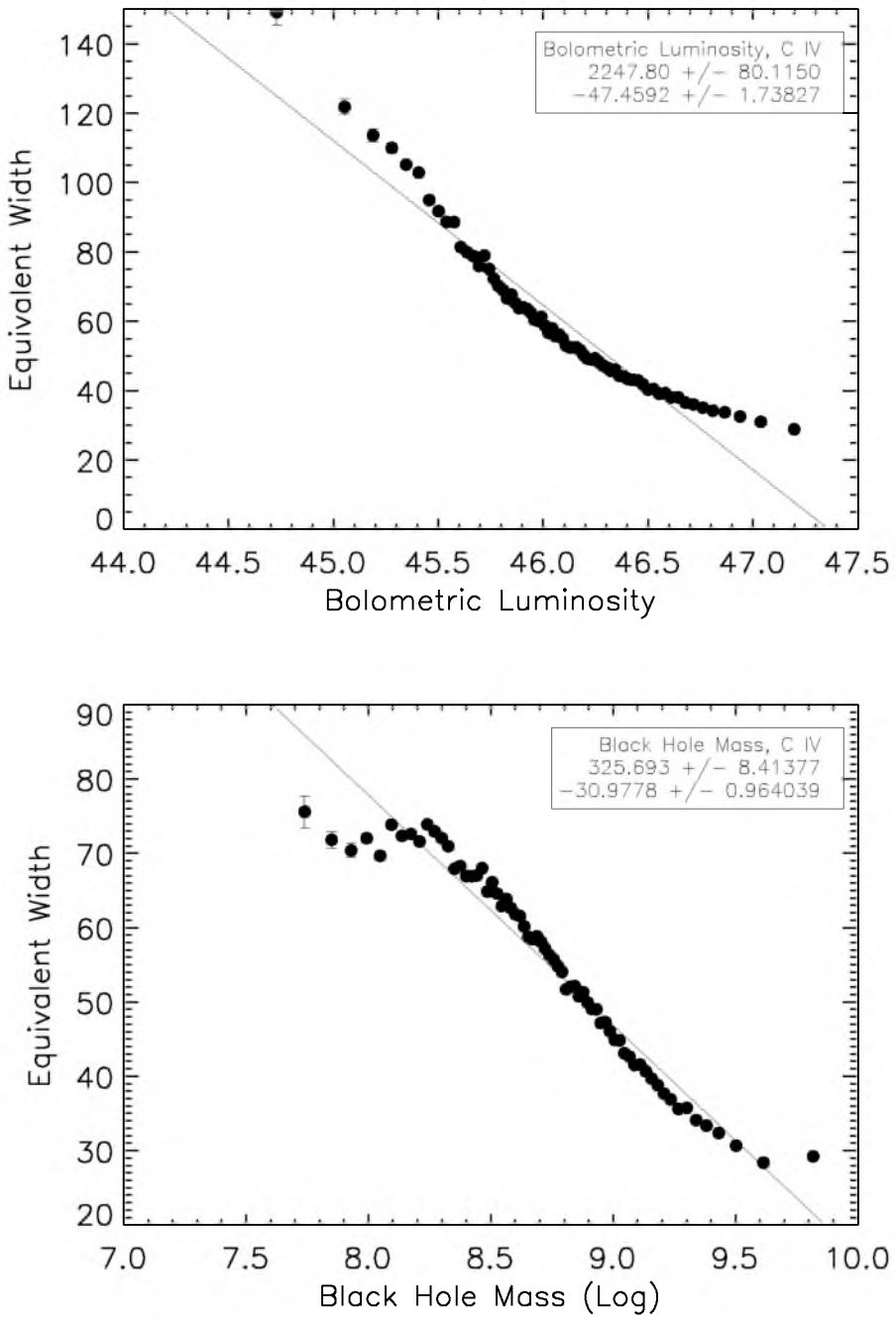

Figure 7.18: The Modified Baldwin Effect detected in the C IV emission line. First Panel: The Modified Baldwin Effect parameterized against the bolometric luminosity and considered using the C IV emission line. The C IV equivalent width is plotted against the log base ten of the eddington ratio. Second Panel: The Modified Baldwin Effect parameterized against the quasar black hole mass and considered using the C IV emission line. The C IV equivalent width is plotted against the log base ten of the black hole mass in solar units.

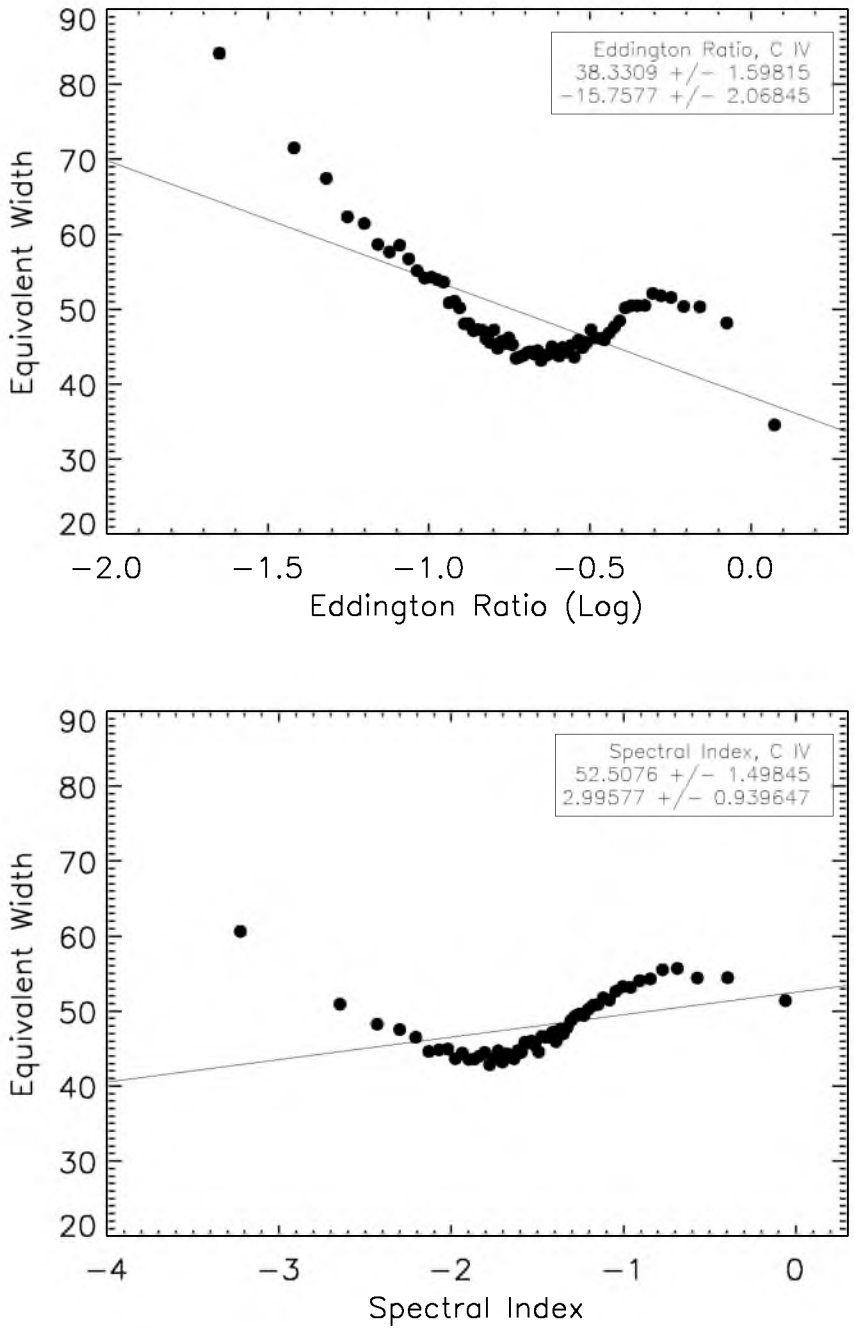

Figure 7.19: The Modified Baldwin Effect detected in the C IV emission line. First Panel: The Modified Baldwin Effect parameterized against the Eddington Ratio and considered using the C IV emission line. The C IV equivalent width is plotted against the log base ten of the Eddington ratio. Second Panel: The Modified Baldwin Effect parameterized against the quasar continuum spectral index and considered using the C IV emission line. The C IV equivalent width is plotted against the quasar continuum spectral index.

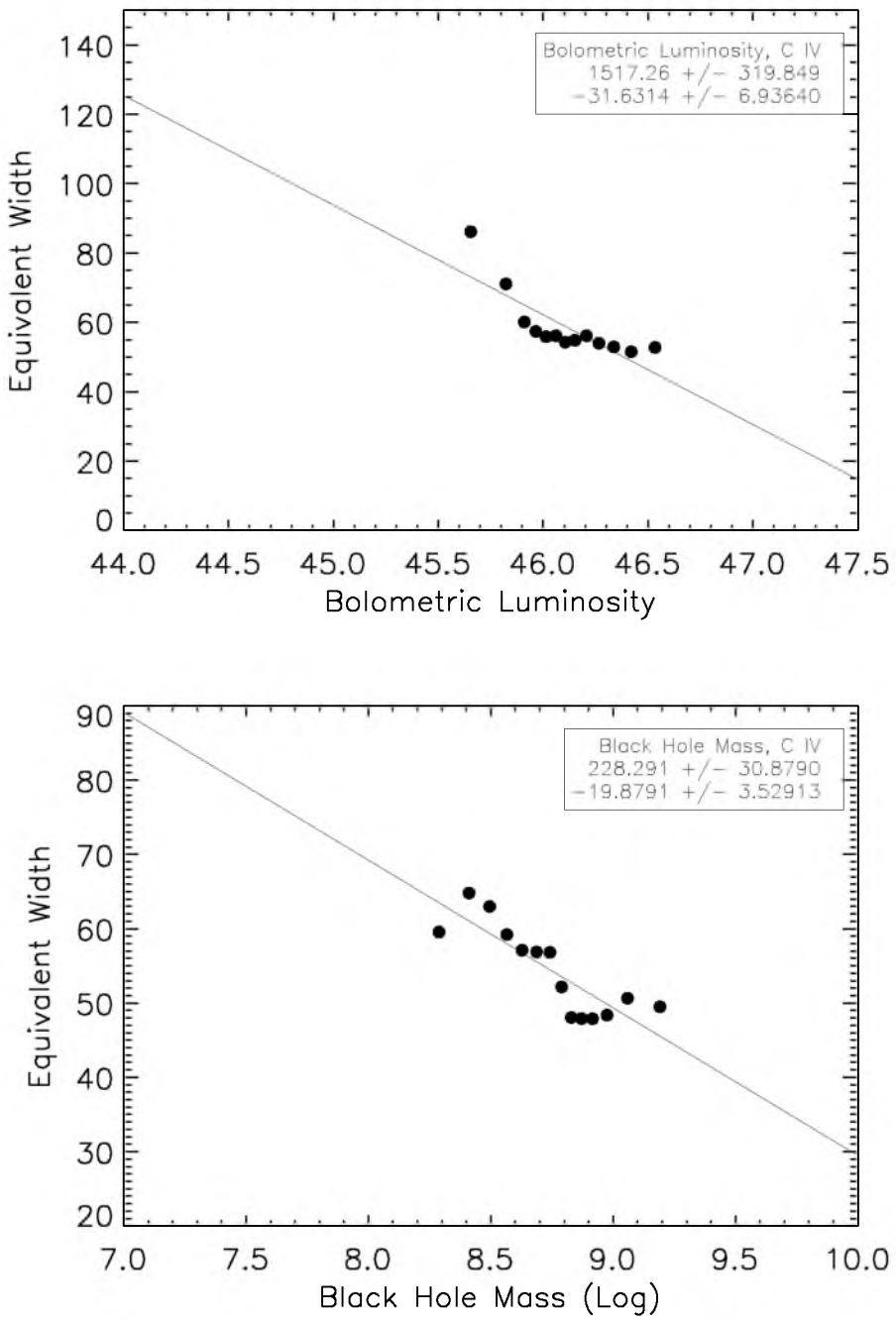

Figure 7.20: Comparison between the traditional Baldwin Effect and the Modified Baldwin Effect in C IV. First Panel: The Baldwin Effect parameterized against bolometric luminosity and considered using the C IV emission line, while removing all but a small range of black hole masses in an attempt to remove or decrease dependence on black hole mass. Second Panel: The Modified Baldwin Effect parameterized against black hole mass and considered using the C IV emission line, while removing all but a small range of quasar bolometric luminosities in an attempt to remove or decrease dependence on luminosity.

CHAPTER 8

DISCUSSION AND CONCLUSION

This dissertation has explained the history of quasar astrophysics and the relevant aspects of modern research, focusing on quasar spectral diversity, especially the inverse correlation between line equivalent width and quasar luminosity. Several models of quasar accretion have been introduced, including Wandel99a, Wandel99b, Korista 99, and the Modified Baldwin Effect.

Data used in this research come from BOSS. All data were properly vetted and corrections to the data were introduced when necessary. Corrections were necessary due to atmospheric differential refraction, and a spectrophotometric correction was included as a consequence. The corrected data were vetted once again and found to better match expectations from SDSS photometry.

A quasar composite spectrum is created through the coaddition of 102,150 corrected quasar spectra. This "master composite" is shown to have similar spectral properties to the median of the input sample. This validates the use of quasar composite spectra for further studies of quasar astrophysics. In addition, new faint lines are detected which had not been identified in previous works. These techniques are used to study models of quasar accretion and quasar spectral diversity. This analysis indicates several items of interest.

The Korista model fits the observed inverse relationship between emission line equivalent width and quasar luminosity well, though the constants differ from theory by some margin. The Baldwin Effect (parameterized on bolometric luminosity) and the Modified Baldwin Effect (parameterized on black hole mass) exist. This result has been known for some time, as the bolometric luminosity is correlated with the black hole mass. Several other interesting correlations between these data are also found.

The strength of the Baldwin Effect (parameterized on bolometric luminosity) and Modified Baldwin Effect (parameterized on black hole mass, Eddington ratio, and spectral index) for four lines commonly used in studying the Baldwin Effect and Modified Baldwin Effect (C IV, He II, Si IV/O IV, and C III/Al III/Si III) is also analyzed. There is a direct, negative correlation between the bolometric luminosity and the equivalent width, as well as

a direct, negative correlation between black hole mass and equivalent width, for each line. The relationship between Eddington ratio and equivalent width as well as the relationship between spectral index and equivalent width is more complex, nonmonotonic, and difficult to predict, making Eddington ratio and spectral index poor candidates for future studies of the Modified Baldwin Effect. In finding the linear fits to the bolometric luminosity versus equivalent width and black hole mass versus equivalent width relationships, I showed that both had a strong correlation. However, the correlation was stronger for bolometric luminosity in three of the lines (C IV, Si IV/O IV, and C III/Al III/Si III) and stronger for black hole mass in one line (He II). This indicates that, despite correlation between black hole mass and bolometric luminosity, I cannot rule out that both may hold importance for the Baldwin Effect. Given the uncertainties in this result, caution must be exercised by the reader in declaring one model to be definitively correct. This is just one point of evidence.

Future research should be directed at finding the relative strengths of the parameters entering into the Baldwin Effect.

REFERENCES

Aihara, H., Allende Prieto, C., An, D., et al. 2011, ApJS, 193, 29

Alam, S., Albareti, F. D., Allende Prieto, C., et al. 2015, ArXiv e-prints, arXiv:1501.00963

Allende Prieto, C., & Lambert, D. L. 2000, AJ, 119, 2445

Anderson, L., Aubourg, E., Bailey, S., et al. 2014, MNRAS, 441, 24

Antonucci, R. 1993, ARA&A, 31, 473

Bachev, R., Marziani, P., Sulentic, J. W., et al. 2004, ApJ, 617, 171

Baldwin, J. A. 1977, ApJ, 214, 679

Baskin, A., & Laor, A. 2004, MNRAS, 350, L31

Becker, G. D., Hewett, P. C., Worseck, G., & Prochaska, J. X. 2013, MNRAS, 430, 2067

Betoule, M., Kessler, R., Guy, J., et al. 2014, A&A, 568, A22

Bianchi, L., Rodriguez-Merino, L., Viton, M., et al. 2007, ApJS, 173, 659

Bolton, A. S., Schlegel, D. J., Aubourg, E., et al. 2012, ArXiv e-prints, arXiv:1207.7326

Boroson, T. A., & Green, R. F. 1992, ApJS, 80, 109

Bovy, J., Hennawi, J. F., Hogg, D. W., et al. 2011, ApJ, 729, 141

Bruhweiler, F., & Verner, E. 2008, ApJ, 675, 83

Burbidge, E. M. 1967, ARA&A, 5, 399

Carswell, R. F., & Smith, M. G. 1978, MNRAS, 185, 381

Croom, S. M., Rhook, K., Corbett, E. A., et al. 2002, MNRAS, 337, 275

Dawson, K. S., Schlegel, D. J., Ahn, C. P., et al. 2013, AJ, 145, 10

Delubac, T., Bautista, J. E., Busca, N. G., et al. 2015, A&A, 574, A59

Denney, K. D., Horne, K., Brandt, W. N., et al. 2016, ArXiv e-prints, arXiv:1601.05425

Dietrich, M., Hamann, F., Shields, J. C., et al. 2002, ApJ, 581, 912

Eisenstein, D. J., Weinberg, D. H., Agol, E., et al. 2011, AJ, 142, 72

Fan, X. 1999, AJ, 117, 2528

Faucher-Gigu`ere, C.-A., Prochaska, J. X., Lidz, A., Hernquist, L., & Zaldarriaga, M. 2008, ApJ, 681, 831

Ferrarese, L., & Merritt, D. 2000, ApJ, 539, L9

Fitzpatrick, E. L. 1999, PASP, 111, 63

Foltz, C. B., Chaffee, F. H., Hewett, P. C., et al. 1989, AJ, 98, 1959

Francis, P. J., Hewett, P. C., Foltz, C. B., et al. 1991, ApJ, 373, 465

Fukugita, M., Ichikawa, T., Gunn, J. E., et al. 1996, AJ, 111, 1748

Gebhardt, K., Bender, R., Bower, G., et al. 2000, ApJ, 539, L13

Ghez, A. M., Klein, B. L., Morris, M., & Becklin, E. E. 1998, ApJ, 509, 678

Green, J. C., Froning, C. S., Osterman, S., et al. 2012, ApJ, 744, 60

Green, P. J., Forster, K., & Kuraszkiewicz, J. 2001, ApJ, 556, 727

Greenstein, J. L. 1963, Nature, 197, 1041

Grier, C. J., Hall, P. B., Brandt, W. N., et al. 2015, ArXiv e-prints, arXiv:1503.03076

Gunn, J. E., Siegmund, W. A., Mannery, E. J., et al. 2006, AJ, 131, 2332

Harris, D. W., Jensen, T. W., Suzuki, N., et al. 2016, ArXiv e-prints, arXiv:1603.08626

Hazard, C., Mackey, M. B., & Shimmins, A. J. 1963, Nature, 197, 1037

Hogg, D. W. 2001, in IAU Symposium, Vol. 204, The Extragalactic Infrared Background and its Cosmological Implications, ed. M. Harwit & M. G. Hauser, 209

Ivezi´c, ˇZ., Lupton, R. H., Schlegel, D., et al. 2004, Astronomische Nachrichten, 325, 583

Iwasawa, K., & Taniguchi, Y. 1993, ApJ, 413, L15

Jiang, L., Fan, X., Cool, R. J., et al. 2006, AJ, 131, 2788

Kinney, A. L., Rivolo, A. R., & Koratkar, A. P. 1990, ApJ, 357, 338

Kirkpatrick, J. A., Schlegel, D. J., Ross, N. P., et al. 2011, ArXiv e-prints, arXiv:1104.4995

Korista, K., Baldwin, J., & Ferland, G. 1998, ApJ, 507, 24

Kormendy, J., & Richstone, D. 1995, ARA&A, 33, 581

Krolik, J. H., Madau, P., & Zycki, P. T. 1994, ApJ, 420, L57

Lupton, R., Gunn, J. E., Ivezi´c, Z., et al. 2001, in Astronomical Society of the Pacific Conference Series, Vol. 238, Astronomical Data Analysis Software and Systems X, ed.

F. R. Harnden Jr., F. A. Primini, & H. E. Payne, 269

Margala, D., Kirkby, D., Dawson, K., et al. 2015, ArXiv e-prints, arXiv:1506.04790

Marziani, P., & Sulentic, J. W. 2014, Advances in Space Research, 54, 1331

Nagao, T., Marconi, A., & Maiolino, R. 2006, A&A, 447, 157

Netzer, H. 1985, MNRAS, 216, 63

Netzer, H., Laor, A., & Gondhalekar, P. M. 1992, MNRAS, 254, 15

Noterdaeme, P., Petitjean, P., Carithers, W. C., et al. 2012, A&A, 547, L1

Oke, J. B. 1963, Nature, 197, 1040

Oke, J. B., & Gunn, J. E. 1983, ApJ, 266, 713

Osmer, P. S., & Shields, J. C. 1999, in Astronomical Society of the Pacific Conference Series, Vol. 162, Quasars and Cosmology, ed. G. Ferland & J. Baldwin, 235

Padmanabhan, N., Schlegel, D. J., Finkbeiner, D. P., et al. 2008, ApJ, 674, 1217

Page, K., & et al. 2004, in "Evidence for Tori and Winds in AGN," held 13-16 September, 2004 at University of Leicester, 25

Paris, I., Petitjean, P., Aubourg, E., et al. 2012, A&A, 548, A66. 2014

Pereyra, N. A., Vanden Berk, D. E., Turnshek, D. A., et al. 2006, ApJ, 642, 87

Pier, J. R., Munn, J. A., Hindsley, R. B., et al. 2003, AJ, 125, 1559

Ricci, C., Paltani, S., Awaki, H., et al. 2013, A&A, 553, A29

Ricci, C., Ueda, Y., Ichikawa, K., et al. 2014, A&A, 567, A142

Richards, G. T., Fan, X., Newberg, H. J., et al. 2002, AJ, 123, 2945

Richards, G. T., Strauss, M. A., Fan, X., et al. 2006, AJ, 131, 2766

Ross, N. P., Myers, A. D., Sheldon, E. S., et al. 2012, ApJS, 199, 3

Ruan, J. J., Anderson, S. F., Dexter, J., & Agol, E. 2014, ApJ, 783, 105

Sakata, Y., Morokuma, T., Minezaki, T., et al. 2011, ApJ, 731, 50

Sandage, A. 1961, The Hubble atlas of galaxies

Schawinski, K., Urry, C. M., Virani, S., et al. 2010a, ApJ, 711, 284

Schawinski, K., Evans, D. A., Virani, S., et al. 2010b, ApJ, 724, L30 107

Schlegel, D. J., Finkbeiner, D. P., & Davis, M. 1998, ApJ, 500, 525

Schmidt, M. 1963, Nature, 197, 1040

Shemmer, O., & Lieber, S. 2015, ApJ, 805, 124

Shen, Y., & Ho, L. C. 2014, Nature, 513, 210

Shen, Y., Richards, G. T., Strauss, M. A., et al. 2011, ApJS, 194, 45

Shields, J. C., Ferland, G. J., & Peterson, B. M. 1995, ApJ, 441, 507

Shull, J. M., Stevans, M., & Danforth, C. W. 2012, ApJ, 752, 162

Smee, S. A., Gunn, J. E., Uomoto, A., et al. 2013, AJ, 146, 32

Smith, J. A., Tucker, D. L., Kent, S., et al. 2002, AJ, 123, 2121

Stevans, M. L., Shull, J. M., Danforth, C. W., & Tilton, E. M. 2014, ApJ, 794, 75

Stoughton, C., Lupton, R. H., Bernardi, M., et al. 2002, AJ, 123, 485

Tanaka, Y., Inoue, H., & Holt, S. S. 1994, PASJ, 46, L37

Tremaine, S. 2014, ArXiv e-prints, arXiv:1407.6363

Tucker, D. L., Kent, S., Richmond, M. W., et al. 2006, Astronomische Nachrichten, 327, 821

Urry, C. M., & Padovani, P. 1995, PASP, 107, 803

Vanden Berk, D., Wilhite, B., Kron, R., et al. 2004, in Bulletin of the American Astronomical Society, Vol. 36, American Astronomical Society Meeting Abstracts, 120.02

Vanden Berk, D. E., Richards, G. T., & SDSS Collaboration. 2000, in Bulletin of the American Astronomical Society, Vol. 32, American Astronomical Society Meeting Abstracts #196, 751

Vanden Berk, D. E., Richards, G. T., Bauer, A., et al. 2001, AJ, 122, 549

Vestergaard, M., & Peterson, B. M. 2006, ApJ, 641, 689

Wandel, A. 1999a, ApJ, 527, 649

Wandel. 1999b, ApJ, 527, 657

Weaver, K. A., Mushotzky, R. F., Arnaud, K. A., et al. 1992, ApJ, 401, L11

Wilhite, B. C., Vanden Berk, D. E., Kron, R. G., et al. 2005, ApJ, 633, 638

Wilkes, B. J., Hooper, E. J., McLeod, K. K., et al. 1999, in ESA Special Publication, Vol. 427, The Universe as Seen by ISO, ed. P. Cox & M. Kessler, 845

Wills, B. J., Netzer, H., & Wills, D. 1985, ApJ, 288, 94

Wright, E. L. 2006, PASP, 118, 1711

Wu, C.-C., Boggess, A., & Gull, T. R. 1983, ApJ, 266, 28

Wu, J., Schneider, D. P., & Vanden Berk, D. E. 2010, in Bulletin of the American Astronomical Society, Vol. 42, American Astronomical Society Meeting Abstracts #215, 373.06

Wu, J., Vanden Berk, D. E., Brandt, W. N., et al. 2009, ApJ, 702, 767

Xu, Y., Bian, W.-H., Yuan, Q.-R., & Huang, K.-L. 2008, MNRAS, 389, 1703

York, D. G., Adelman, J., Anderson, J. E., et al. 2000, AJ, 120, 1579

Zamorani, G., Marano, B., Mignoli, M., Zitelli, V., & Boyle, B. J. 1992, MNRAS, 256, 238

Zhang, K., Wang, T.-G., Gaskell, C. M., & Dong, X.-B. 2013, ApJ, 762, 51

Zhou, X.-L., & Wang, J.-M. 2005, ApJ, 618, L83